Winter 1-15-2021

Nanoscale Enhancement of Photosensitized Radionuclide Stimulated Therapy

Daniel Douglas Lane
Washington University in St. Louis

Follow this and additional works at: https://openscholarship.wustl.edu/eng_etds

Part of the Biomedical Engineering and Bioengineering Commons, Materials Science and Engineering Commons, and the Mechanics of Materials Commons

WASHINGTON UNIVERSITY IN ST. LOUIS

Department of Biomedical Engineering

School of Engineering and Applied Science

Washington University in St Louis

Dissertation Examination Committee:
Samuel Achilefu, Chair
Abdel Kareem Azab
Hong Chen
Gregory M. Lanza
Srikanth Singamaneni

Nanoscale Enhancement of Photosensitized Radionuclide Stimulated Therapy
by
Daniel Douglas Lane

A dissertation presented to
The Graduate School
of Washington University in
partial fulfillment of the
requirements for the degree
of Doctor of Philosophy

January 2021
St. Louis, Missouri

Table of Contents

List of Figures

<u>Acknowledgments</u>

My time spent at WUSTL has greatly increased my understanding of the scientific method and I thank the whole institution for the support and growth it has given me. Specifically, I would like to thank my PI and mentor Samuel Achilefu for his vision and drive that allowed me to pursue meaningful contributions to our field. I would also like to thank Rui Tang and Kvar Black for assisting me throughout this dissertation in more ways than can be named. I want to thank Gail Sudlow for helping with mouse studies and being the lab mother to us all. I want to thank Julie Prior and Katie Duncan for *in vivo* imaging and mouse handling. Finally, for assistance in cell culture I would like to thank Matthew Mixdorf, Dorota Grabowska and Brad Manion.

Members of the Biswas group offered irreplaceable contribution to this dissertation both materially and intellectually. I want to thank you all for your contribution and technical trainings through the NanoResearch Facility, including: ICP-MS, ICP-OES, DLS and TEM. Specifically, I would like to thank Nathan Reed, Ramesh Raliya, and Sanmathi Chavalmane Subbenaik. For TEM imaging assistance and equipment, Gregory Strout provided invaluable expertise and keen insight through the Washington University Center for Cellular Imaging.

For my peers within the lab, both current and past, I thank you all for keeping me sane. Thank you, Rebecca Gilson, for instructing me in ROS investigation as well and being a friend, I am glad your back in the country. Jessica Miller for her friendship and as my fellow cofounder of Astaria Medical, her work ethic and drive are unparalleled, inspiring me to new heights. Thank you Deep Hathi, Nick Cho, Suman Mondal and Christine O'Brien as the best drinking buddies

and conversationalists I have met in St. Louis. To Hengbo Huang, Lei Fang, Hanru Zhang, Hongyu Meng and Megan Michie who have been there to talk to and discuss research.

I thank you all for assisting my development as a scientist and engineer.

Daniel D. Lane

Washington University in St. Louis

January 2021

Dedicated to my family and my love:

Douglas, Wendy, and Marcus Lane for all the growth and good times to get me here

Brenna Brown for keeping me loved and cared for over these 6 year

Abstract of The Dissertation

Nanoscale Enhancement of Photosensitized Radionuclide Stimulated Therapy

By

Daniel D. Lane

Doctor of Philosophy in Biomedical Engineering

Washington University in St. Louis, 2021

Professor Samuel Achilefu, Chair

Photodynamic therapy (PDT) provides efficient tumor killing through the generation of reactive oxygen species (ROS) from the optical excitation of a photosensitizer (PS). Furthermore, this mechanism is highly immune stimulating, providing systemic tumor immunity with a reduction in metastasis. However, these materials had previously been limited by their dependence upon external light sources, allowing treatment of only laser-accessible malignancy. With the recent development of photosensitized radiation stimulated therapy (PRaST) this depth dependence is broken through co-localization of radionuclides and semiconducting photosensitizers.

This dissertation focuses on the enhancement of titanium dioxide (TiO_2) based PRaST agents through understanding of TiO_2 material parameters as well as adsorbed surface coatings to enhance therapeutic outcomes. TiO_2 has several known crystal phases and can be generated

from an atomic cluster to micrometer size. To improve its therapeutic potential, we first investigated the effect these parameters had on its primary constraints, namely ROS generation and biodistribution, finding an interplay between 5 nm and 25 nm TiO_2 crystal domains. Furthermore, we sought to overcome the central tumor resistance mechanism to PDT, that of oxygen dependence. ROS generation from molecular PS traditionally use near infra-red (NIR) optical excitation of electrons, this energy then being transferred to an associated molecular oxygen. Nanoscale TiO_2 can use both electron and hole intersystem crossing, generating ROS from adsorbed oxygen and hydrolysis. To enhance these pathways, we investigated the ability of chromium VI ions to increase TiO_2 hole flux as well as the ability of adsorbed dichromate to act as an oxygen independent metallo-therapeutic. Finally, we develop a polymer stabilized perfluorocarbon nanoemulsion able to be tracked with near-infrared fluorescent imaging and increase the oxygen tension of hypoxic tumor tissue. This normalization can boost ROS generation and normalize tumor microenvironments. Combined, these developments point to new nano-design strategies to improve upon novel PRaST, optimizing the particles to both improve ROS generation and decrease tumor resistance.

__Chapter 1: Introduction__

1.1 Cancer Therapy

Cancer remains the 2nd leading cause of death globally, bringing undue suffering.[1] The treatment of the pain, both personal and societal, remains an essential goal of medicine. In pursuit of this cause there has been year over year funding increases from both governmental and charity sources, with large advances in survivability being achieved.[2] However, complete remission remains elusive due to metastasis, drug resistance and/or quiescence.[3,4] Complete remission of cancer requires systemic therapies which can exploit the bodies inherent defensive mechanisms as well as provide direct targeting of subtle differences between malignant cells and surrounding tissue.[5,6] One such disparity, metabolic dysregulation, results in an unbalanced cellular redox state. This imbalance makes cancerous cells particularly sensitive to additional strain on redox control mechanisms and effective therapy can be induced through the delivery of reactive oxygen species (ROS).

1.2 Reactive Oxygen Species and Cancer Biology

Undesired reactive molecules are byproducts of cellular metabolism and must be carefully controlled to maintain stable growth and replication/function for normal tissue. One primary class of metabolic byproducts are ROS whose highly energetic nature can damage lipids, proteins, and nucleic acids.[7] Normal cells control ROS through anti-oxidants and enzymes which

de-energize them to ground state.[8,9] Cancers, however, have dysregulated metabolic processes and increased survival signaling, leading to elevated intracellular ROS concentration.[10]

Mitochondria produce ROS during aerobic metabolism, producing superoxide, which can interconvert into hydrogen peroxide, and hydroxyl radicals.[11,12] The pathways which limit off-target damage are legion but the major systems revolve around glutathione and ascorbate redox cycling.[13] As the primary chemical anti-oxidants within the cell, the sulfur and hydroxyl groups can both reduce ROS before catalytic recovery either through enzymes or the NADH cycle.[14] Specific enzymes also exist for ROS such as singlet oxygen dismutase, which stabilizes singlet oxygen to hydrogen peroxide.[15,16] Peroxides are further degraded by ascorbate and glutathione peroxidase, both recovering the chemical anti-oxidants and degrading peroxides to water and oxygen.[17]

Cancers tend to have elevated levels of ROS within their cytosol due to dysregulation of these redox control pathways. In active tumors, this is due to elevated metabolism but this effect persists in quiescent cells due to dysregulation of cell death pathways and other signaling processes.[3] As over production of ROS can lead to a variety of cell death signals, cancer tissue must bypass them, particularly the HIF1-α and P53 mechanisms.[18] This increases susceptibility to further ROS damage while also generating highly immune stimulating damage-associated molecular patterns (DAMP).[19,20] Cells that perish from ROS stress undergo immune surveillance, further stimulated by DAMPs within the cellular detritus, increasing recruitment of dendritic cells, activated T-Cells, and possible anti-cancer beta cell generation. This increased immune reactivity makes ROS induced DAMPs effective in generating systemic immune targeting of cancer, limiting the relapse of tumors and attacking metastasis.[21,22]

1.3 History of Photodynamic Therapy

Photodynamic therapy (PDT) is one of the primary methods for generating ROS. Driven by the absorbance of optical energy by a photosensitizer (PS), it can transfer energy into ROS (Figure 1-1).[23,24] Light has long been recognized for its healing properties, predating even Herodotus, with modern recognition of its benefits amplified by a Nobel prize awarded in 1903 for lupus treatment.[23] However, the combination of a PS and light was first described in 1900 by the doctoral student Oscar Raab who accidentally exposed suspended protozoa stained with acridine orange to a bright light.[25] The description of the eukaryote's death was quickly published.[26] Raab and his mentors then brought the method to clinic before the end of the 1900's which proved effective on skin tumors. However, the therapy received little notice, dropping from common medical use.[27] This technique would later become photodynamic therapy (PDT) which emerged briefly in the 1950s with interest in porphyrins then slowly being investigated until the late 1970's when the clinical relevance of PDT was brought to the world by Dougherty et. al.[28–30] Their work resulted in the first clinically approved photosensitizer (PS), Photofrin (1993) for use on bladder cancer.[31] Since that time PDT has passed through three generations and is entering its fourth.[5,24,32–35]

While Photofrin heralded the first generation of porphyrin based PS, it had several side effects and shortcomings.[36,37] The most apparent of these issues were depth of penetration and systemic light sensitization, limiting treatment to laser accessible sites and requiring indoor quarantine for a week or more.[38,39] To overcome this impediment the second generation attempted to modify the porphyrin structure itself or expand into new dyes, increasing the wavelength of activation and site selectively. One example is ALA-5, is enzymatically activated

to PP-IX when reaching the target tissue, a conversion that favors metabolically active cancers and is activatable by NIR light.[40–43] While the 2nd generation increased the depth of penetration, the limit remained ~ 1 cm, primarily due to tissue heating effects of NIR lasers.[44] Additionally, choice of the NIR wavelengths came at the cost of lower optical energy, also lowering the energy of the generated ROS. The third generation remains ongoing and is categorized by nanoparticle (NP) and/or antibody targeting of existing PS but has little to improve the penetration depth of therapy.

A new generation of PS is currently being developed that can return to higher energy ROS generation and/or overcome depth of penetration issues. Using either two-photon absorbance for molecular photosensitizers, like aggregation-induced emission lumigens (AIEgens), or up-conversion NP like NaYF3:Eu:Yb, the energy level of delivered light can be increased.[45–47] However, these still rely on external laser sources limited depth of penetration. To overcome both depth and energy concerns, sonodynamic therapy has used sonosensitizers for ROS generation but this carries the downside of direct beam targeting and limited reduction of satellite malignancy.[48,49] Photodynamic radiation-stimulated therapy (PRaST), recently developed within our lab, can overcome both penetration depth and energy restrictions while providing systemic targeting.
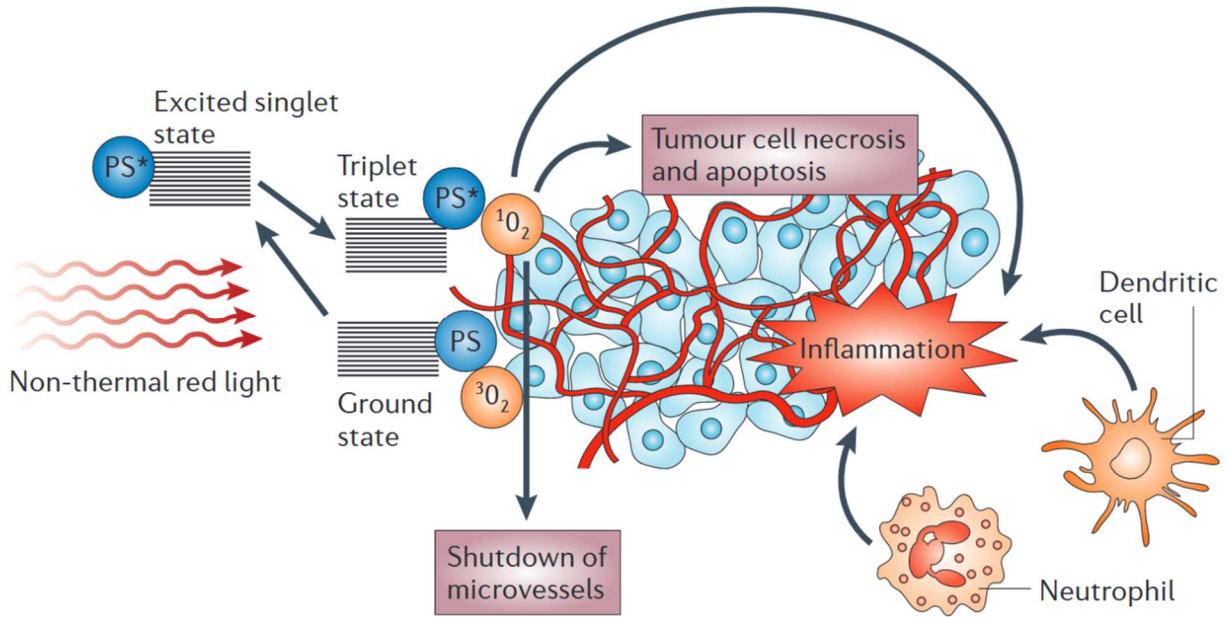
Figure 0-1: The mechanism of photodynamic therapy.
The photosensitizer (PS) absorbs light and an electron moves to the first short-lived excited singlet state. This is followed by intersystem crossing, in which the excited electron changes its spin and produces a longer-lived triplet state. The PS triplet transfers energy to ROS, in this case ground-state triplet oxygen, which produces reactive singlet oxygen ($^1O_2$). ROS can directly kill tumor cells by the induction of necrosis and/or apoptosis, can cause destruction of tumor vasculature and produces DAMP activating leukocytes such as dendritic cells and neutrophils.[50]

1.4 PRaST

Instead of directly relying upon photon energy, PRaST exploits multiple energy delivery mechanisms resulting from radio decay to drive the PDT (Figure 1-2), showing great effect in mouse models of cancer.[51,52] PRaST utilizes non-toxic doses of radiation, below that normally required for direct radio-therapy and allowing energy release anywhere within the body.[53,54] This systemic delivery is supplemented by the cancer seeking nature of existing PET radio tracers whose beta emission provides easily exploitable energy and offers imaging capabilities. The energy types emitted by beta decay are Cherenkov radiation, beta capture and daughter redox reactions (Figure 1-2). To utilize these requires the use of specifically designed PS and knowledge of each's properties.
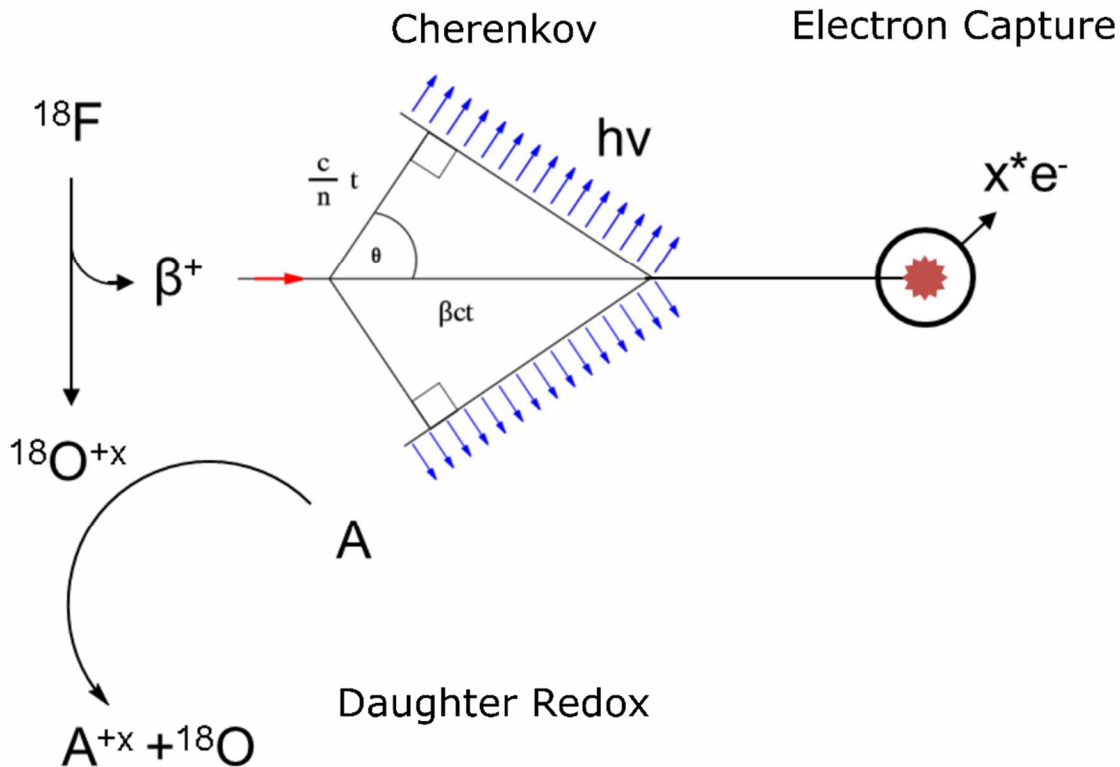
Figure 0-2: PRaST energy delivery mechanisms.
After a sufficiently energetic beta decay (either positron or electron) Cherenkov light is generated in dielectric media for PS excitation. The particle can then annihilate or be captured by a material, generating multiple excited Auger electrons. Finally, the daughter product undergoes separate redox reactions to return to ground state.

Cherenkov radiation (CR) is a byproduct of the faster-than-light travel of a charged particle in dielectric media. The travel of the particle causes polarization of the media along its path, relaxing and generating an electromagnetic wave. CR pulls energy from the particle and transfers it into optical emission, reducing the velocity of the particle to below the speed of light for the medium.[55–58] The spectrum produced depends upon the medium and the energy of the particle but follows the proportion of $1/\lambda^3$ (λ being wavelength) vs photon flux.[56,59] The combination of water absorbance and the exponential decay proportionality places the tissue intensity maximum near 200 nm (UV-C light, Figure 1-3), with a mean free path of <1 mm in tissue.[60] Visible to the naked eye at high radiation doses as a blue glow, Figure 1-3B shows the luminescence of ^{64}Cu, a beta emitter, under an open filter in an IVIS (in vivo imaging system)

imager. Figure 1-3C shows the lack of photon flux above a 500 nm cutoff (specifically the built-in GFP filter, pass range 515-575 nm) leaving most of the flux in the UV, unable to activate existing PS.

The second energy transfer mechanism for PRaST is scintillation, a process particularly relevant to nanoscale inorganic materials which can regenerate from the process.[61] The direct capture of a beta particle can occur up to 10 mm from the decay source in tissue, depending upon the emission energy.[62] In the case of both positron and electron capture, the resulting energy can cause a multiple electron energy transfer cascade known as the Auger process, able to generate several trapped, excited electrons, and therefore ROS. The final PRaST energy mechanism is daughter product redox equilibration. As the original atom's nucleus ejects a beta particle the resulting nucleus is often left with residual energy due to electron imbalance. This excited atom then undergoes energy decay processes, including redox reactions, till reaching ground state. Directing this energy to specific regions, however, is challenging and more often leads to non-specific reactions. This process is inherent in radioactive decay and does generate ROS but does not directly involve a PS, simply adding to redox imbalances. These combined energy delivery mechanisms, with their limited travel distance in tissue, keeps PRaST energy within a malignancy and benefits from co-targeting of both the radionuclide and PS.

When considering the PS to use with PRaST, however, these three energy mechanisms must be considered and require a rethink of current PS canon. Instead of needing high quantum efficiencies in the NIR window developed in the 2nd generation, PRaST requires high UV and beta capture density. Considering these factors titanium dixoide NPs have proven effective as PRaST PS.

7
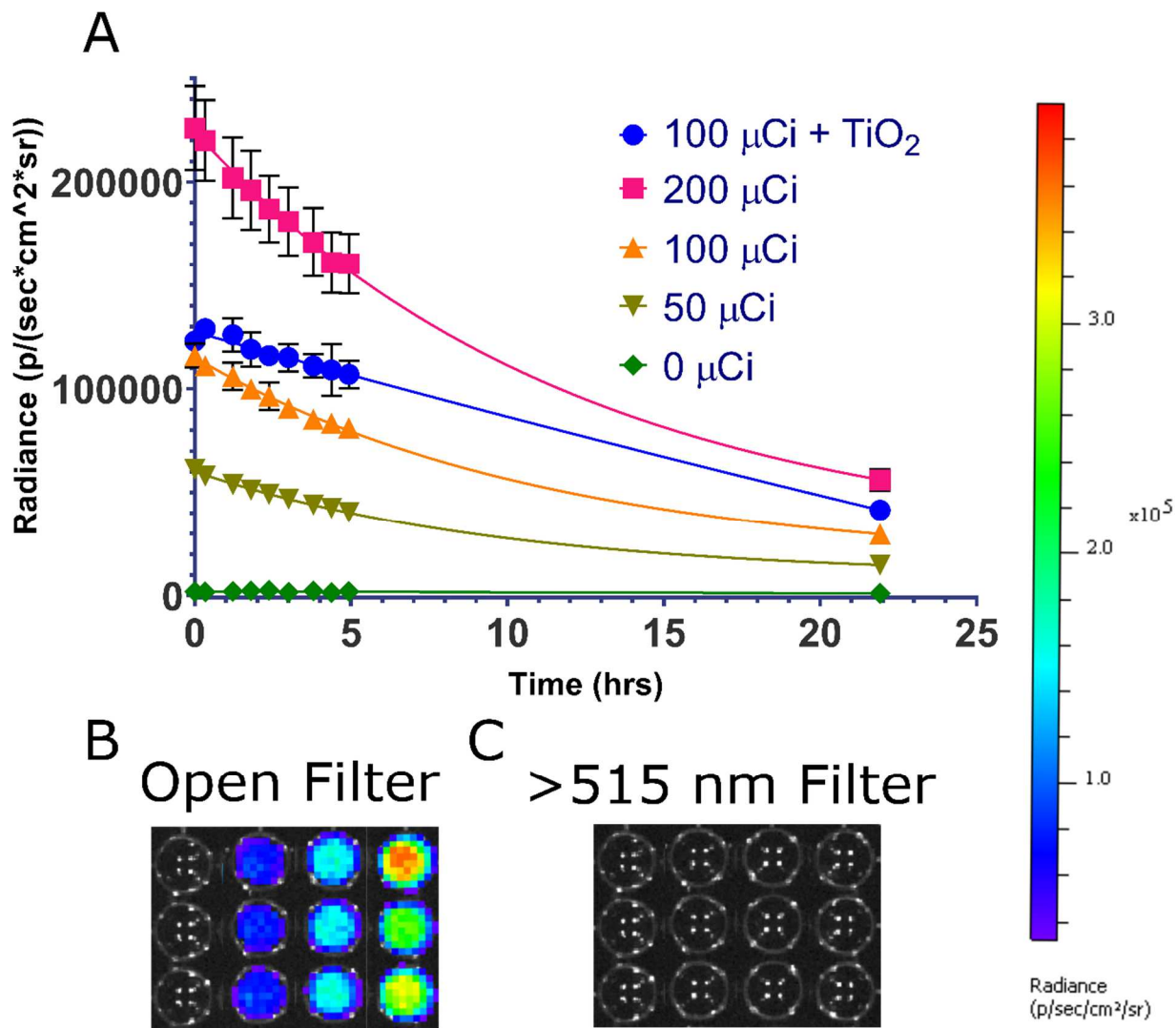
Figure 0-3: Decay based Cherenkov radiation generation.
A) Luminescence decay of ^{64}Cu in water alone or in the presence of 25 nm TiO$_2$. Decay half-life follows that of [64]Cu's 12 hr. Luminescence image of ^{64}Cu at 200 µCi with a B) open or C) 515 nm high pass filter, scale bar for both is located right.

1.5 Titanium Dioxide PRaST

In 2014 our lab developed titanium dioxide (TiO$_2$) as a PRaST agent, using FDG and

[64]Cu as beta emitters for stimulation (Figure 1-4).[51] TiO$_2$ is a heavily investigated semiconductor

known for its catalytic properties and absorbance characteristics which make it an ideal catalyst

for both industry and academic purposes.[63] TiO$_2$ is highly bio-tolerated, has a catalytic surface

with tunable hydrophilicity, electron/hole trapping energies sufficient for hydrolysis, can be easily synthesized into NP and has a high optical and radio-absorbance density.[64] When combined with beta emitters this system showed remission of murine breast tumors in a subcutaneous mouse model and showed great promise for a new generation of PS. The work contained herein focuses on the refinement and enhancement of TiO_2 based pRaST to further increase its conversion efficiency and limit tumor resistance mechanisms.
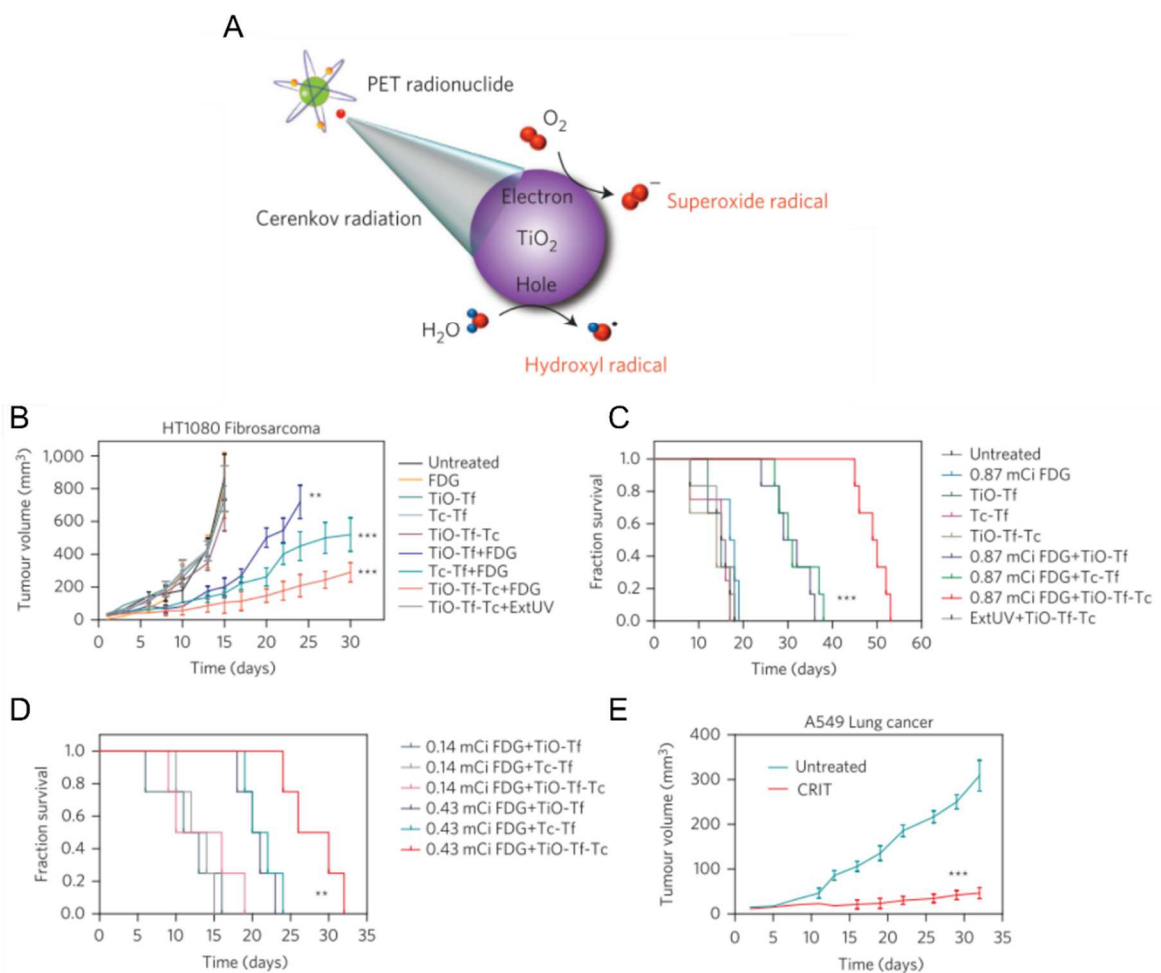
Figure 0-4: *In vivo* PRaST Efficacy.
A) Schematic of the Cherenkov-mediated excitation of TiO_2 NPs to generate cytotoxic hydroxyl and superoxide radicals from water and dissolved oxygen, respectively, through electron–hole pair generation. B) In vivo PRaST through a one-time systemic administration in tumor-bearing Athymic nu/nu mice. **P < 0.01, ***P < 0.001. ExtUV, external ultraviolet. C)The Kaplan–Meier survival curves represent treatment with 0.87 mCi/0.1 ml FDG. ***P<0.001. D) The survival curves represent treatment with 0.14 and 0.43 mCi/0.1 ml FDG (n = 4 mice per group). **P < 0.01. E) In vivo CRIT in A549-tumor-bearing Athymic nu/nu mice using TiO_2-Tf-Tc and FDG. ***P < 0.001. [51]

1.8 Aims of this Dissertation

The objective of this dissertation is to enhance TiO_2 based PRaST through nanoscale modification. We accomplished this by undertaking the following research:

Chapter 2: The Effect of Size and Crystal Structure on ROS Generation and Biodistribution of TiO_2 Nanoaggregates

Chapter 3: Chromate Based Hole Injection for Oxygen Independence in TiO_2 Photosensitization

Chapter 4: Cr(VI) Ion State Change Therapy for Cancer Suppression

Chapter 5: Oxygen Delivery by Perfluoronated Nanoemulsions

Chapter 2: The Effect of Size and Crystal Structure on ROS Generation and Biodistribution of TiO₂ Nanoaggregates

Lane, Daniel D. et al. 2020. "Effects of Core Titanium Crystal Dimension and Crystal Phase on ROS Generation and Tumor Accumulation of Transferrin Coated Titanium Dioxide Nanoaggregates." *RSC Advances* 10(40): 23759–66.

2.1 Chapter Summary

Transferrin-TiO$_2$ (Tf-TiO$_2$) has been proven to be an effective PRaST agent. However, the material properties of TiO$_2$ had not been investigated to maximize its bio-efficacy, specifically considering biodistribution and ROS generation. Here we sought to improve both aspects through reduction of TiO$_2$'s core dimension (cTd) and alteration of the crystal structure. Investigation of sub-50 nm cTd showed stable particles averaging a diameter of 108 nm by dialysis. This consistent structure was investigated by TEM, revealing that Tf-TiO$_2$ particles consisted of nanoaggregates (NAG) that packed varying numbers of TiO$_2$ cores into a Tf coated, fixed volume. While the NAG size remained consistent with cTd, the ROS generation was altered with peak generation occurring at 25 nm cTd. Alteration of crystal type from anatase to amorphous improved ROS generation but NAG stability suffered. Finally, the biodistribution of 5 and 25 nm NAGs showed higher uptake by 5 nm Tf-TiO$_2$, with a tumor-to-muscle ratio of 13.3 by ICP and 6.02 by fluorescence. Combined, this information suggests cTd's of <25 nm is ideal

for full *in vivo* investigation of PRaST to balance the tumor uptake against the ROS generation capabilities.

2.2 Introduction

Titanium Dioxide

Titanium dioxide (TiO_2) is a semiconductor capable of regenerative photocatalysis and has been heavily investigated since its optical catalysis was described by Fujishima et al. in the 1970s.[65] Fujishima discovered that UV exposed TiO_2 could lower the energy of water hydrolysis well below that normally required. Further investigation showed the surface of titanium dioxide has efficient trap sites for high energy holes and electrons generated from the optical excitation.[66] TiO_2 trap sites exist at the materials interface allowing environmental electrical conjugation to adsorbed molecular species, namely water and oxygen. These traps also limit exciton recombination, the major mechanism of energy loss, leading to high catalytic efficiency.[67] Solution studies against ROS reporter dyes revealed TiO_2 catalysis also comes, in part, from ROS generated upon UV excitation, including highly reactive hydroxyl radicals generated directly from water. As ROS therapy had been conceptualized in the 1980s, several attempts were made to convert TiO_2 into an anti-cancer theraputic.[68,69] However, its dependence on UV light, and challenging particle stabilization limited its efficacy.

With the advent of PRaST, the UV absorbance from TiO_2's large bandgap became a boon as it improved electron/hole redox potential relative to current generation photosensitizers.[70,71] Particularly, the ability to generate high energy hydroxyl radicals through hole based reactions facilitates low oxygen ROS generation. The surface bound hydroxyls are rapidly replaced by

adsorbed water through deprotonation allowing unlimited catalytic recovery. Tumors generate hypoxic regions due to malformed vasculature and high metabolic rate.[4,72,73] The generation of hydroxyl radical from water also requires a redox energy of +2.27 V vs. standard hydrogen electrode (SHE), an energy too high for near-infrared photosensitizers.[70,74] Additionally, TiO_2's bandgap and electron density increase beta capture efficacy over most standard carbon based PS.[75] These ROS generation properties, along with a stable crystal structure, strong UV band optical density and electron-dense structure make TiO_2 ideal for PRaST energy absorption through Cherenkov radiation and beta capture.[56,76–78]

Exciton Trapping and Crystal Effects

The efficiency of PDT is directly affected by electron and hole separation in a material. An exciton (electron/hole pair) can easily recombine in materials that lack extended electrical conjugation, which allows exciton travel, and trapping groups. If an exciton does recombine, the energy is lost to bond resonance or fluorescence/phosphorescence.[79] In an aqueous environment, TiO_2 shows rapid trapping of electrons/holes in oxygen/titanium defects, respectively, limiting recombination.[80–82] The trapping rate relies on the defect density in TiO_2, specifically acidic titanium or hydroxyl sites, with a higher density increasing the overall photoactivity.[83] Furthermore, TiO_2's hole traps correlate with adsorbed water/hydroxyl sites, facilitating rapid oxidation and release of hydroxyl radicals.[84] The electron traps are surface oxygen defects and reduce molecular oxygen to singlet oxygen and other ROS.[74]

The surface defect rate has been associated with several factors, including TiO_2's bulk crystal phase, core TiO_2 crystal dimension (cTd), and surface coating.[85] Early investigations of the natural crystal phases, anatase and rutile, revealed anatase to have a higher ROS production

potential.[64,86] This is attributed to the higher bandgap and surface potential of anatase, as well as increased trap density on the (0,0,1) plane.[87,88] Some evidence suggests amorphous/mixed crystal phase TiO_2 have higher ROS quantum yields due to undefined surface regions, higher total surface defect rate, and exciton splitting between different crystal sub-domains.[89] These conclusions, however, often conflict due to the heterogeneity of synthesized amorphous materials. One example of increased ROS generation is P25 Degussa TiO_2, the gold standard for catalysis, a mixed phase crystal material with increased photocatalytic yield relative to pure anatase.[90,91]

The cTd also alters ROS generation rates, often breaking the catalytic surface area dependence when approaching the nanoscale. At the nanoscale TiO_2 particles have increased crystallinity which limits the number of surface defects, lowering ROS conversion.[89] Additionally, recent work by Shen et al. shows multiple defect sites must be co-localized on a oxide surface to generate ROS, this being scarce as surface area decreases.[84] Overall, the cTd investigated across several TiO_2 photocatalytic systems shows peak ROS generation in the 7-40 nm range.[89,92,93]

Transferrin Coating

The 80 kDa β-globulin Tf has the combined advantages of high affinity to Ti^{+3} ions, non-toxicity, and tumor targeting effects.[94–96] Tf itself is the third most common protein in serum, being a vital iron transporter. Additionally, Tf has a well-known record as a tumor targeting agent, increasing the therapeutic outcome of molecular species and nanoformulations.[97,98] This is a result of EPR enhancement and tumor upregulation of the Tf-receptor to feed a metabolically enhanced iron demand, increasing Tf retention in cancer tissue.[99–101]

Tf also regulates iron trafficking to the brain where iron demand is high, specifically shuttling iron to astrocytes.[102,103] After being bound and trafficked through the clathrin coated endosomal pathway, the bound iron is released. This iron is then transported in the cytoplasm where it is bound to ferroportin and is separately transported into the spinal fluid. The Tf and covalently bound materials are then recycled back into the blood-stream, limiting blood brain barrier transport.[104]

Biodistribution of Nanoparticles

For maximum therapeutic effect, NP design requires high, tumor specific bio-distribution, requiring consideration of surface properties, material size and targeting groups. The most vital biological properties these parameters effect are the enhanced permeability and retention (EPR) effect, caused by leaky tumor vasculature, the as well as liver, kidney and spleen filtration.[6,105,106] In general, particles must limit all non-tumor uptake, being larger than the hydrodynamic diameter limit of 7 nm for nephron filtration, and smaller than 150 nm to avoid macrophage uptake in liver and spleen.[6,107] For solid NPs like TiO_2, the effective size is modified by protein adsorption.[108,109] Previous studies have tracked renal excretion and, using quantum dots, showed about 5.5 nm is the limit for hard nanostructures.[110]

2.3 Experimental Method

Materials

Apo-Transferrin was purchased from Athens Research and Technology (Athens, GA), TiO_2 cTd's were provided by the Biswas lab, all chemicals were purchased from Sigma-Aldrich (St. Louis, MO).

TiO₂ Core Synthesis and Crystal Structure

TiO$_2$ cTds of various sizes (5 - 1000 nm diameter) were prepared by hydrothermal reaction of titanium alkoxide (titanium isopropoxide: TTIP) stabilized in an acidic ethanol-water (1:2 to 1:8 v/v) solution by modifying the method previously proposed.[111] The 25 nm anatase TiO$_2$ synthesis is used as an example for the rest of the experimental section. The pH of an ethanol and water solution was adjusted to 0.7 with 1 M nitric acid. 100 μL of 0.02 M TTIP (97%) was added dropwise to this solution. The reaction was magnetically stirred at 400 rpm (25 °C) followed by 4 hrs thermal treatment at 220 °C. Synthesized crystals were washed several times with ethanol to remove un-reacted alkoxide. The materials were then either dried under vacuum or dispersed in a solvent for further use. For different crystal structures, the calcination conditions were altered to 250 °C for 4 hrs for anatase-rutile and 2 hrs at 120 °C for amorphous.[112]

The size and morphology of the TiO$_2$ cTds was investigated using transmission electron microscopy (TEM) with an 80 keV FEI Tecnai Spirit Transmission Electron Microscope. A 2 μL sample was placed on an ultrathin lacey carbon grid, 400 mesh (Ted Pella Inc.) and allowed to sit for 5 min before removal of the droplet via wicking with a Chemwipe and vacuum drying. To visualize the Tf coating, a dried grid sample was stained for 1 min with uranyl acetate (UA), 3 μL drop of 4% (w/v), before blotting and vacuum drying to limit UA crystal contamination. X-ray diffraction (XRD) was performed to confirm the crystal phase of TiO$_2$ NPs.[113] 25 mg of dry TiO$_2$ powder was added to a low background silicon sample holder and scanned (coupled two-theta/theta) from 5-60 degrees with a 15 rpm sample rotation and anti-scatter fins in place. The data was analyzed with Bruker DIFFRAC.EVA program.

Stabilization of Tf-TiO₂ NAGs

TiO₂ cTd solutions (1 mg/mL) were prepared in 1x Dulbecco's phosphate-buffered saline (DPBS) and vortexed to homogeneity. Immediately, Tf was added at a mass ratio of 1:3 (TiO₂ to Tf) and mixed until dissolved. This solution was then separated into 2 mL aliquots before sonication by a small-bore probe at 3 W output for 40 seconds (kept below 50 °C from sonic heating) to form Tf-TiO₂ NAGs. Post sonication, the aliquots were filtered through a Millex-HV PVDF 0.22 μm filter, unless otherwise stated. Note that due to size, >200 nm cores were not filtered, but instead centrifuged at 1k for 1 min before resuspension under sonication.

Characterization of Tf-TiO₂ Particles

Hydrodynamic diameter and zeta potential of the suspensions were both determined with the Malvern Zetasizer Nano ZS. Particle measurements were performed in a 2 cm path-length quartz cuvette and a folded capillary zeta cell (Malvern Instruments Ltd), respectively. A triplicate of each sample was diluted to 0.01 mg/mL TiO₂ to produce an optically clear solution of the particles in DPBS for dynamic light scattering (DLS) and deionized water (diH₂O) for zeta potential measurements. Z-average size and polydispersity index (PDI) of the TiO₂ NAGs were obtained with an average of 12 runs. TEM was performed to validate morphology and size of the coated particles. Quantification of protein coating was carried out using a Pierce BCA Protein Assay kit to determine Tf concentration (1) before coating, (2) remaining in the supernatant after coating and centrifugation, and (3) the amount remaining in the particle sample. Long-term stability was quantified using three separate 2 mL samples at 1 mg/mL of Sigma-Aldrich Tf-TiO₂, prepared in water. These were stored at 4 °C and 100 μL samples were diluted to 0.01 mg/mL in water and analyzed on DLS as described above.

ROS Quantification

Dichlorofluorescein diacetate (DCF-DA) was used to quantify general ROS production from Tf-TiO$_2$, and hydroxyphenyl fluorescein (HPF) was used to detect hydroxyl radicals.[114] DCF-DA was activated to DCF by adding DCF-DA (45 µL, 5.55 mM) in Dimethyl sulfoxide (DMSO) to NaOH (5 µL, 1 N) and incubating for 10 min, producing a 5 mM stock that was refreshed for each sample run. DCF and HPF were added to TiO$_2$ samples from DMSO with 5 mM starting concentrations. The Tf-TiO$_2$ samples were prepared as above but not filtered to preserve the concentration more closely, relying on orbital shaking between reads to maintain homogeneity. The initial Tf-TiO$_2$ formulation (1 and 3 mg/mL TiO$_2$ and Tf, respectively) was then diluted to 0.01 mg/mL TiO$_2$ in 1 mL and 5 µM HPF or DCF was added.

An uncoated, black walled, flat and clear bottom 96 well plate (Greiner Bio-One) containing 150 µL sample per well was used for ROS quantification. Each plating was performed in triplicate with a well geometry that allowed an average power of 1.9 mW across each triplicate set. For comparison between runs, a bare 25 nm TiO$_2$ DCF control was always plated to quantify variability. After loading, the plate was shaken for 20 seconds in a double orbital pattern and analyzed on a plate reader (BioTek Synergy Neo2) using 487 nm excitation and 528 nm emission. Subsequently, the plate was automatically exposed to UV light for 80 seconds before being shaken again, repeating the process. This was carried out for a total of 30 min for each plate and the data was compiled into pseudo-first-order kinetic curves for reporting.

***In Vivo* Tumor Model and Biodistribution**

All studies were conducted in compliance with Washington University Animal Welfare Committee's requirements for the care and use of laboratory animals in research. Fluorescent

imaging of biodistribution was carried out in HT1080 fibrosarcoma model nu/nu mice. Cells were injected at 1 x 10^6 and grown till reaching 10 mm by caliper. Freshly prepared 5 and 25 nm Tf-TiO$_2$ NAGs in PBS were injected via tail vein (100 µL, 1 mg/mL). Imaging was done on a Li-Core PEARL imager with the 700 nm channel (ex 685/em 720 nm) pre-injection and 2, 4 and 24 hrs post-injection. At 24 hrs animals were euthanized and organs excised for biodistribution.

ICP-MS biodistribution was quantified on breast cancer (4T1)-bearing BALB/c mice (n=4/group). 4T1 (1 X 10^6 cells) were injected subcutaneously and grown to 10 mm by caliper. The animals were euthanized 24 hrs post-injection. To quantify the TiO$_2$ biodistribution, major organs and tumor tissue were harvested, homogenized, and degraded using nitric acid and H$_2$O$_2$ (hydrogen peroxide) and Ti content in each organ was quantified by an Elan DRC II.

2.4 Results

Synthesis and Characterization of TiO$_2$ Core NPs

Different sizes (5, 15, 25, 30, 50, 100, 200, and 1000 nm) of TiO$_2$ cTd as described above (Figure 2.1) were prepared through sol-gel synthesis. The electrophoretic zeta potential of the cores was between -19 and -35 mV. Using 25 nm cTds as a base cTd, three different crystal phases were synthesized and characterized - anatase, anatase-rutile, and amorphous. DLS measurements showed an average PDI of 0.15 +/- 0.035 at pH 5.8 in ethanol across all cores.
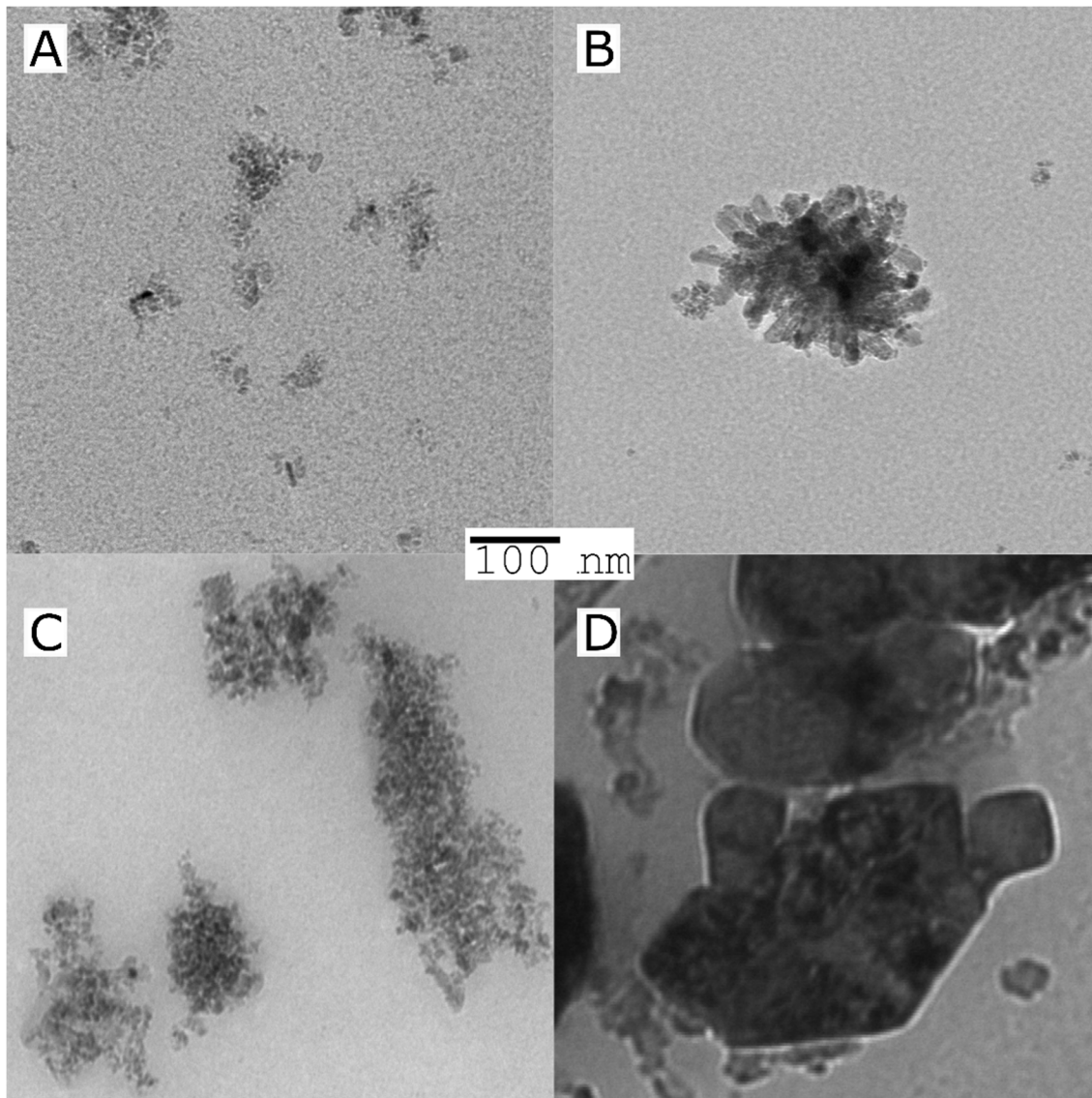
Figure 0-1: Sol-gel synthesized TiO₂ crystals.
TEM images of TiO₂ A) 5, B) 15, C) 50, D) 200 nm.

XRD analysis shows three core crystal phases matching 26º, 37º, and 55º peaks for

anatase and 36º, 42º, and 54º peaks for rutile (Figure 2-2B). Amorphous particles have weaker

facets of both phases due to the lack of annealing during synthesis. TEM of the synthesized cores

shows clustering in aqueous media that can range from a single cTd to multi micron aggregates.

The crystallites match the expected pseudo-octahedral crystal shape, appearing as slight

elongated, rhomboid shapes. Preferential elongation along a single axis was observed as the

particle size increased, creating NPs with a standard aspect ratio of near 2:1 for 200 nm tetragonal crystals (Figure 2-1D). The anatase crystal structure was further shown in the diffraction bands (Figure 2-2A) whose graph analyses exhibited two patterns with a spacing of 0.3312 ± 0.0811 nm and 0.3568 ± 0.0993 nm for each (~3.5 Å literature).[115] The different sizes and crystal phases provided diverse parameters to assess their ROS-generating properties and biodistribution.
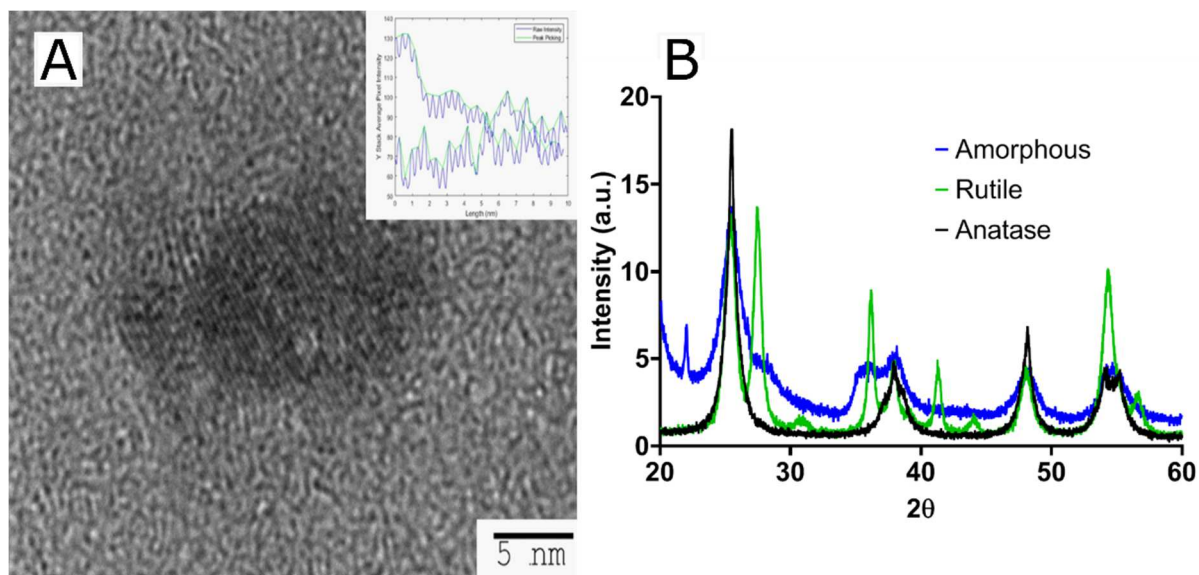
Figure 0-2: TiO₂ crystal structure confirmation.
A) TEM of an anatase particle, insert figure is ImageJ peak picking of crystal facets for lattice spacing determination. B) Xray diffraction of anatase, mixed anatase rutile and amorphous particles used in our examination.

Coating of Core TiO₂ NPs with Tf Produces Distinct NAGs

To stabilize the random aggregates seen above the TiO₂ cTds were coated with Tf, which served as both a dispersing and tumor-targeting agent. Previous results from within our group had shown the coating of 25 nm cTd TiO₂ with apo-transferrin (Tf) produced Tf-TiO₂ particles with individual cores near 30 nm by TEM. However, this conflicted with DLS measures averaging 108 nm which suggested either a unique structured water layer, a thick Tf coating, or multiple cTd per particle. Observation of the clusters by TEM showed consistent NAG structure

across all Tf-TiO_2 particles. For 25 nm core NPs, they appeared as agglomerated TiO_2 cores coated with Tf, with an average size of 105.1 ± 59.15 nm (Figure 2-3D) generated from edge finding algorithms in Image-J. Visual analysis suggests the number of cores in each particle decreases with increasing core size. Due to this decrease, it is possible the final NAG size is governed by entropic effects in water, causing a volume-restricted stable point that is then filled by a number of cores stabilized by Tf, forming a stable (low PDI) NAG. BCA analysis of 25 nm anatase Tf-TiO_2 NAGs showed 95 ± 2.9 Tf per particle. Adjusting for the expected volume of a Tf layer this size indicates a monolayer to bilayer coating the NAG surface. Interestingly the size distribution narrowed as the core size approached the filter cutoff, dropping from PDI 0.17 to 0.03 suggesting higher selectivity. This is likely driven by selection of a narrowing gaussian edge of cTd by the filter.

Attempts to coat TiO_2 with holo-Tf resulted in uncontrolled aggregation of TiO_2 to >1 μm (PDI of 1) compared to the stable apo-Tf. This suggests that iron binding limits TiO_2 coating, possibly due to direct interaction of Tf's binding site with surface titanium defects. For apo-Tf DLS analysis provided an average NAG size of 108 ± 1.13 nm for 5 to 35 nm core NPs (Figure 2-3C). This consistent NAG size was disrupted at 50 nm cTd where it gradually increased as the core size increased. It was difficult to obtain an accurate measurement post 200 nm cTd due to rapid settling.
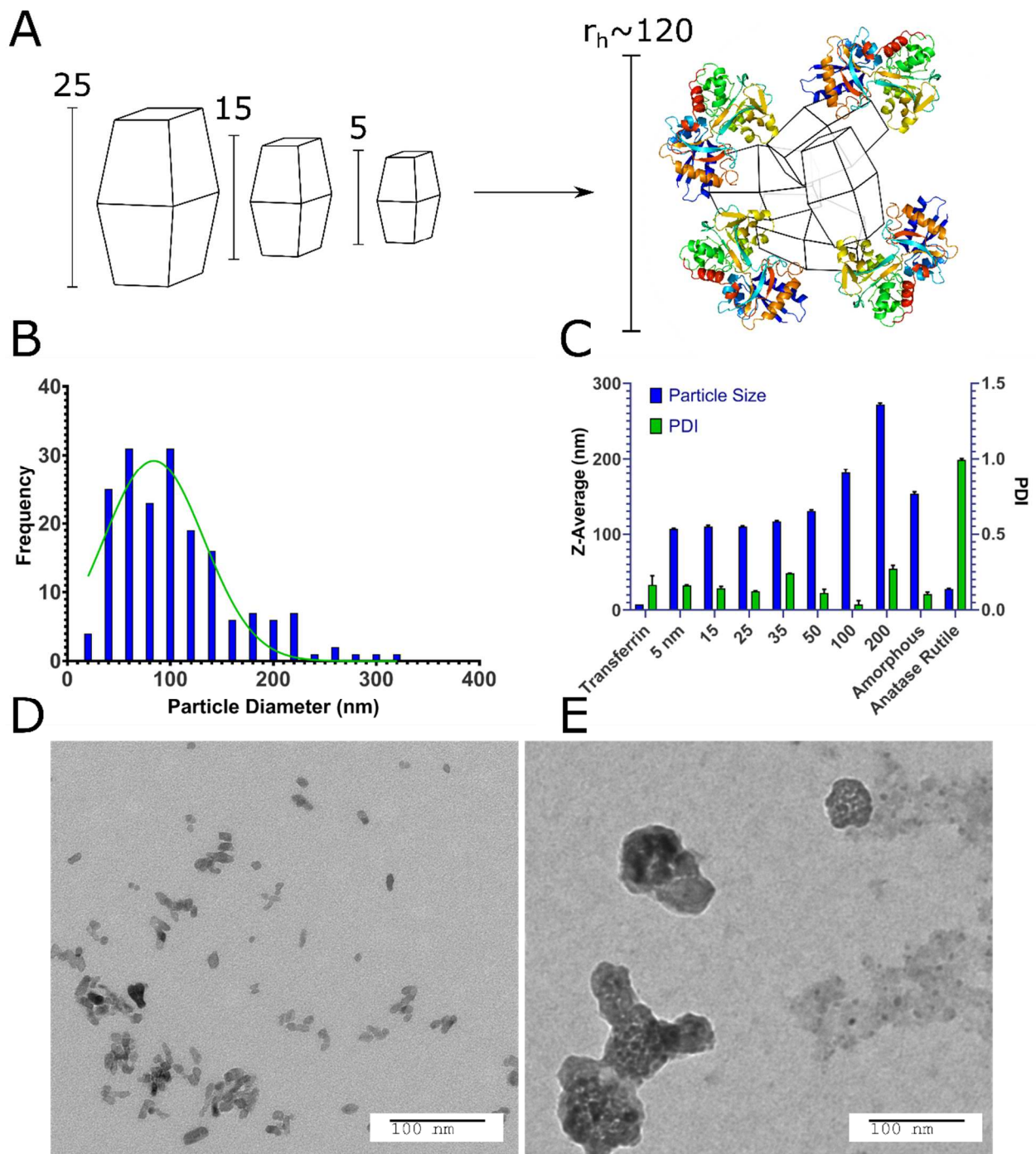
Figure 0-3: Effect of TiO$_2$ cTd on Tf-TiO$_2$ particle size.
A) Schematic depicting the Tf coating of multiple cTd forming similarly sized NAGs. B) Intensity % histogram of a Tf-TiO$_2$, 25 nm cTd particle by DLS. C) Z-average size and PDI of various cTd and crystal structures after Tf coating. TEM of Tf-TiO$_2$ 25 nm cTd particles D) unstained and E) stained with uranyl acetate showing Tf layer on NAGs.

The crystal phase also influenced the overall NAG size. This effect was not driven by differences in buffer conditions as each crystal type was synthesized through the same process, differing only in the finishing temperatures. The PBS buffer was used to maintain the formulation at pH 7 for all NPs. Amorphous particles show a larger average particle size, likely due to increased surface energy and hydroxylation in aqueous solution. This increased water affinity and lack of exposed $Ti^{+3/+4}$ on the surface, characteristic of amorphous TiO_2, likely lowers the affinity for Tf. This lack of affinity removes the stabilizing coating and drives aggregation, limiting the overall stability of amorphous NAGs.[94,116] NAG size of the mixed anatase-rutile TiO_2 collapsed from the anatase cTd along with a drastic increase in size heterogeneity indicated by PDI (Figure 2-3C). This was driven in part by high filter retention, suggesting the Tf coating was unstable on these particles.

A fundamental problem with many NP formulations is the poor shelf life. Thus, 25 nm core NAGs stored at 2 □C were monitored for over two months in diH$_2$O and PBS (Figure 2-4). Longitudinal tracking of size and PDI via DLS show the dispersion of NPs in diH$_2$O exhibiting high stability over 60 days, with consistent PDI below 0.2. PBS had a larger particle size during storage and seemed to become destabilized before the 60-day mark. The result suggests that diH$_2$O is useful in maintaining NAG's integrity for long term storage.
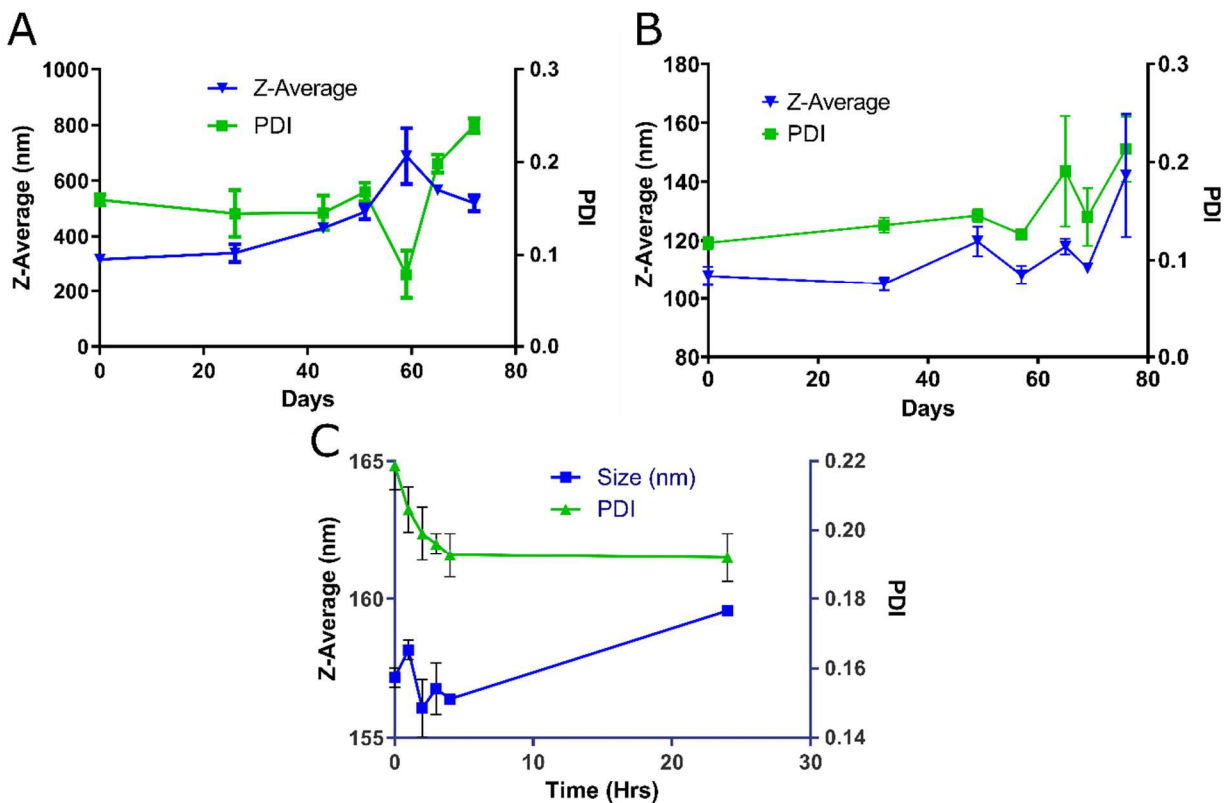
Figure 0-4: Tf-TiO$_2$ particle stability in various media.
25 nm Tf-TiO$_2$ NAG storage stability in A)PBS or B) di-water measured by DLS. C) Tf-TiO$_2$ serum stability over 24 hr.

ROS Production Exhibits Non-linear Relationship with NP Size

ROS producing capacity of the NPs varied with size and crystal phase. Comparison of all

the NPs prepared showed that the 25 nm core NAGs produced the most ROS in both HPF and

DCF measurements (Figure 2-5A). This finding contrasts with standard catalytic particle theory,

which suggests increased surface area per gram should show the highest ROS.[117] The results here

show 25 nm NPs have 180% enhanced DCF conversion rate vs. 15 nm and a 190% enhanced

HPF rate over 5 nm particles, its nearest competitors for the respective reporters. Our results

agree with data originally generated against non-UV exposed, bare TiO$_2$ which suggested low

cTd have decreased surface defect rate below 25 nm.[89] As Ti^{3+} defects act as binding sites for

surface hydroxyls and oxygen, they are essential for exciton separation and catalysis. Therefore,

the loss of defects for 5 nm cTd TiO_2 limits the ROS production.[82] The drop off above 25 nm

approximates the canonical loss of surface area, a $1/r^3$ decrease.[118] Furthermore, the HPF signal

increased relative to DCF at 5nm cTd. This phenomenon is likely driven by increased exciton

confinement near the Bohr radius of the exciton (~3.2 nm in TiO_2). That confinement further

increases the absorbed energy, which favors hydroxyl radical generation by holes but has little

effect on oxygen catalysis.[70] This shift toward hydroxyl generation may be vital in hypoxic

tumor cores as water splitting is the main transfer path for hydroxyl radicals, possibly removing

oxygen dependence, a vulnerability of many small molecule photosensitizers.[119]

Crystal Type Affects ROS Generation in Tf-TiO₂ NAGs

Previous studies demonstrated that amorphous particles can improve ROS quantum

yield.[89] Here we explored whether this pattern can translate to NAGs using 25 nm core NPs. Our

results show a 260% increase in ROS production of amorphous over anatase (Figure 2-5B). This

increase is likely caused by an increased surface defect rate. Since amorphous particles lack

regular crystal structure (Figure 2-2B), they leave grain boundaries that propagate to the surface

and increase trapping. Additionally, the amorphous cTd's lack of calcination leaves a higher oxy

anion concentration on the surface of particles, which has been shown to increase the catalytic

rate.[83] It is also apparent that the rutile content reduces overall ROS yield, as reported

previously.[120] This is caused by a decrease in surface energy compared to the high defect rate

anatase active crystal plane (101), which, when combined with anatase-rutile's lower band gap

decreases it's ROS yield compared to anatase.[80] These data point to the importance of the

presence of TiO_2 surface defects in maximizing ROS generation.
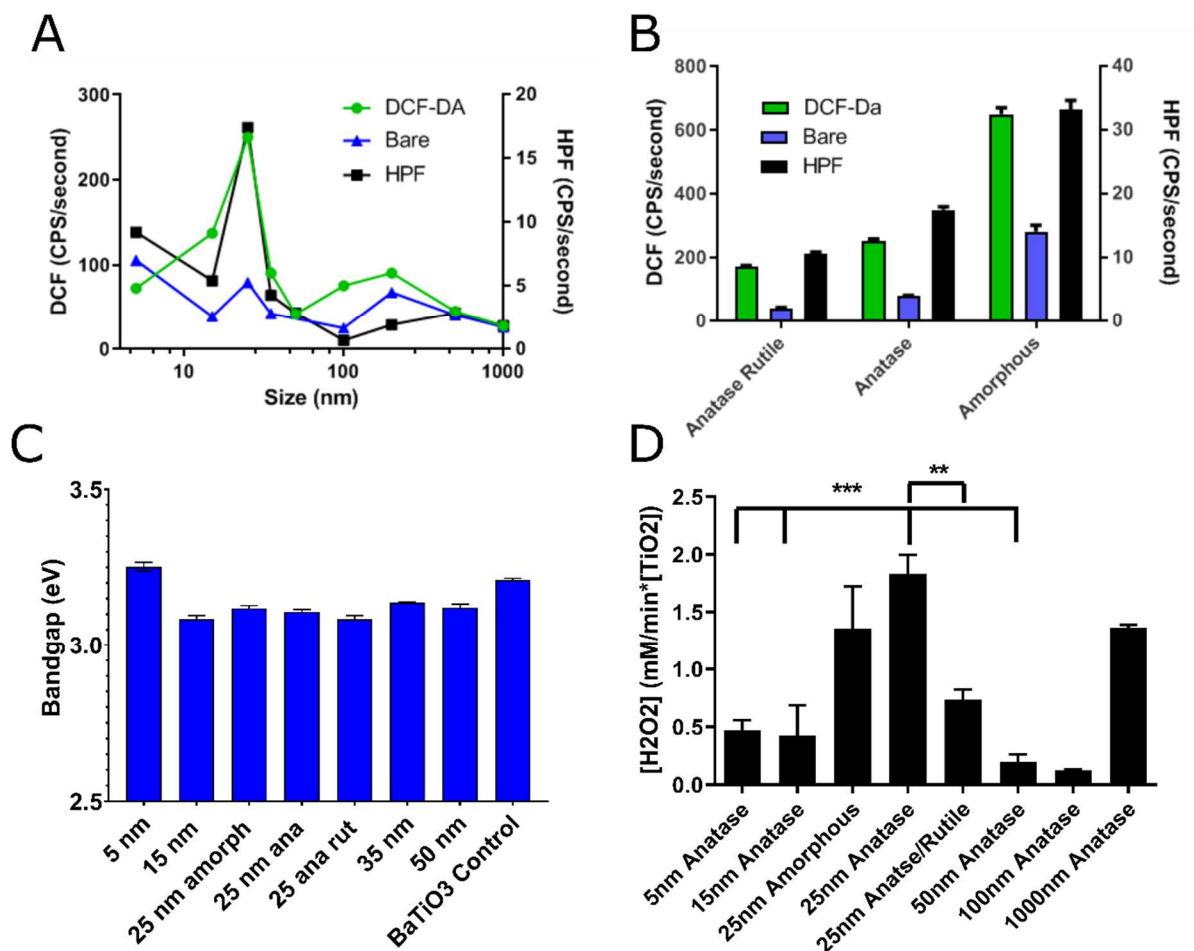
Figure 0-5: ROS generation for each cTd and crystal type.
A) ROS generation rate by cTd, denoted by rate of fluorescence increase fit by pseudo-first order constant. B) ROS generation by different crystal types for Tf-TiO₂ particles. C) Bandgaps for each cTd determined by Tauc plot from diffuse reflectance spectra assuming indirect bandgap. D) Hydroxyl radical generation relative to a set amount of hydrogen peroxide split by the Fenton reaction, normalized for mass.

Small TiO₂ Core NAGs Exhibit High Tumor Retention

For *in vivo* biodistribution studies 5 and 25 nm cTd NPs were selected for their high ROS and similar NAG size. Using Alexafluor-680 bound apo-Tf the cTds were coated and tracked via fluorescence. Figure 2-6C shows that after 4 hr, particle accumulation is likely near its peak and persists within the tumor. When the tissue was excised, the biodistribution of 5 nm NAGs showed higher tumor uptake with a tumor to muscle ratio of 6.2 v 25 nm TiO₂/Cr's 4.53. This

result was not statistically significant however, and some bladder signal was present which suggested kidney clearance, which should be impossible without nephron damage, for TiO_2 particles.
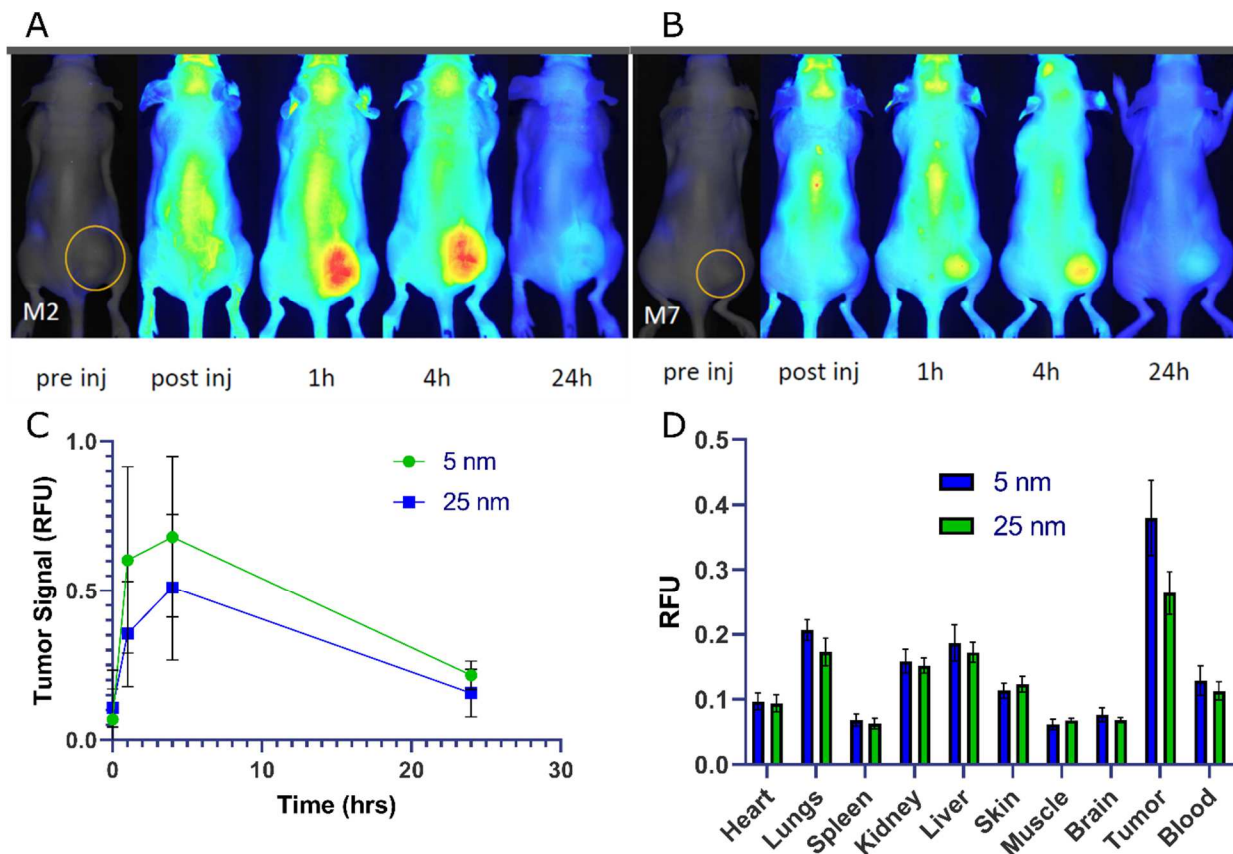
Figure 0-6: Fluorescent biodistribution of Alexa680-Tf coated on 5 and 25 nm TiO_2.
Fluorescent images of the A) 5nm and B) 25 nm Ti/Alexa-680 Tf particles. C) The mean tumor signal over time for both particles. D) Fluorescent biodistribution of excised organs from all mice. (n=5, n.s.)

To more accurately track the biodistribution of titanium, ICP-MS on degraded tissue was run for 5 and 25 nm NAG. ICP-MS measurement of ^{48}Ti accumulation showed an increase in tumor localization per unit mass for 5 nm core NAGs with a total of 2.7 µg/g (Figure 2-7). Further, a six-fold higher tumor to muscle ratio was observed between 5 nm core NAGs (13.3) compared to the 25 nm core (2.83). Although the NAG sizes for the two NP cores are similar, our result suggests the *in vivo* biological distribution may differ. Possibly due to stripping of

28

transferrin from the NAGs in circulation, high intravenous shear force, or other biological

interactions which may dissociate the NAGs, thereby reducing the size to more closely match the

cTd. To discount the possible serum displacement the stability of the NAGs over 24 hours was

tracked and showed no relevant change in the particle size, staying within sampling error out to

24 hours.

ICP tracking showed apparent uptake in the brain. This is likely caused by a combination

of ^{48}Ti interference by ^{48}Ca and the uptake of NAGs by astrocytes via transferrin mediated

internalization.[103,121]
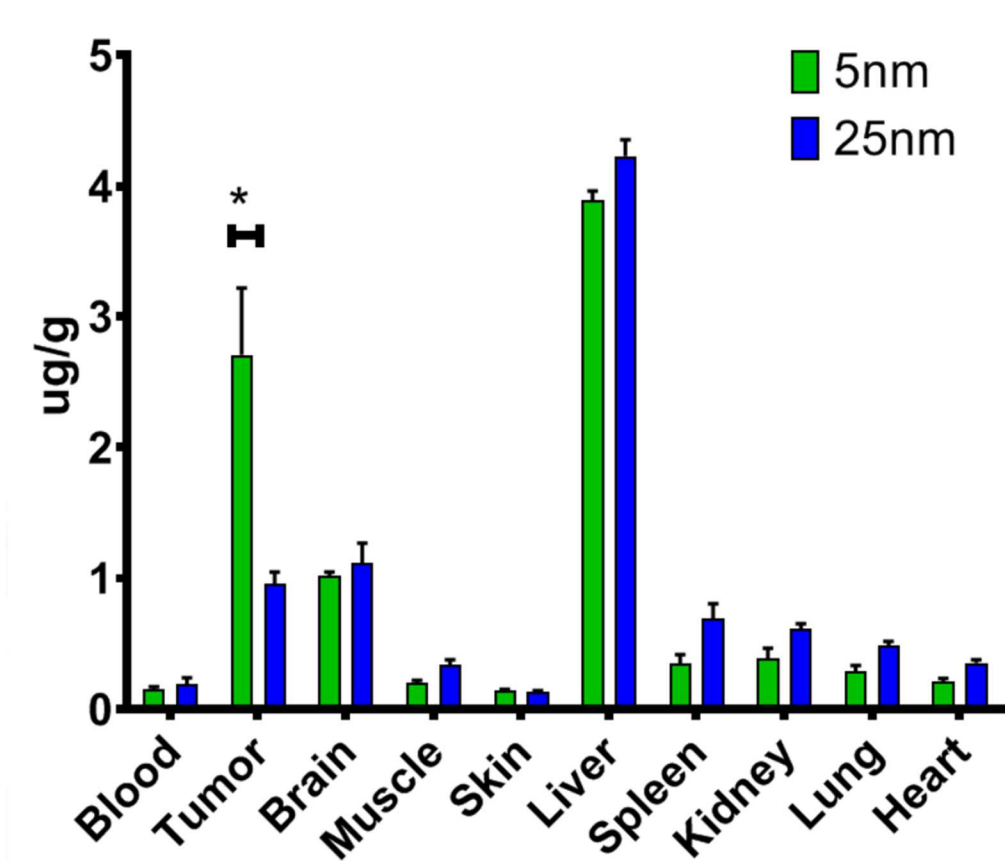
Figure 0-7: Biodistribution of titanium *in vivo* by ICP-MS.
Run against 5 and 25 nm cTd Tf-TiO$_2$, n=8. (*P < 0.01). Measure is μg of Ti ion per gram tissue.

2.5 Discussion

Analysis of the TiO$_2$ core size and crystal reveal their direct impact on ROS generation and *in vivo* biodistribution. First, cTd appears to have little impact on the size of the NAGs formed in aqueous suspensions, likely due to the formulation size being driven by the particle surface energy and not physical core dimensions. This is most apparent when comparing differing crystal phases against the final formulated size, with higher surface energy cores resulting in larger Tf-TiO$_2$ NAGs. While the core size had little effect on the final NAG, it did significantly impact the ROS production. The 25 nm core NAGs clearly generated the most ROS, which held true for both bare TiO$_2$ and Tf-TiO$_2$ NAGs. The 5 nm NAGs produced the next largest amount of ROS at half the rate of the 25 nm NAGs. This is likely due to the 5 nm NP's large increase in the surface area over 25 nm which partially compensated for the reduction in defect sites. Furthermore, the defect hypothesis was corroborated by the highest ROS production rate from the amorphous crystal structure, having a 200% enhancement in rate. Unfortunately, amorphous NAGs sit near 200 nm which limits its utility. Additionally, the increase in HPF production at 5 nm implies small cTd may be used to fine-tune oxygen sensitivity of TiO$_2$ but at the cost of absorbance range.

Finally, 5 nm cTd NAGs also show improved tumor localization over 25 nm, showing the importance of cTd in tumor accumulation properties. With this in mind, there must be a balance between the nearly 2-fold enhancement of ROS generation by the 25 nm over the 5 nm particles versus the nearly 3-fold increase in the tumor uptake of the 5 nm over the 25 nm NPs when designing PRaST strategies. For PRaST TiO$_2$ photosensitizers must both generate high amounts

of ROS as well as significantly accumulate with radionuclides in tumors. Assuming linearity, this 3x to 2x ratio suggests the ideal cTd size would lean towards the 5 nm NAGs.

2.6 Conclusion

Overall, depth-independent photodynamic therapy offers broad potential in the treatment of cancer, with TiO_2 based nanophotosensitizers having already shown *in vivo* promise. However, the material properties play a direct role in the efficacy of the treatment. Herein, we have elucidated key parameters in the design of TiO_2-based nanophotosensitizers that refine both the ROS-generating and biodistribution necessary to enhance therapeutic effect *in vitro*. Future therapy studies in mouse models of cancer are ongoing to identify which of the two factors dominate therapeutic response. These design features include the use of cTds that contain significant numbers of surface defect sites that generate ROS, whether in anatase or amorphous form, and the use of smaller crystals (< 25 nm) with higher tumor accumulation, which should be incorporated into the future design of TiO_2 photodynamic agents.

Chapter 3: Titanium Dioxide/Chromate Hole Injection

3.1 Chapter Summary

Electron injection via a sensitizer dye was recently investigated by our group to reduce TiO_2's dependence on oxygen for PDT.[122] However, electron injection can only improve electron flux, a pathway shown to increase the energy level of molecular oxygen radicals. Here we show that TiO_2/Cr(VI) particles can be generated for hole injection for hydrolysis. This absorption is concentration-dependent indicating surface equilibrium, binding 1.03 ug Cr(VI) per mg TiO_2 at pH 5. However, at pH 5 the speciation of Cr(VI) shifts to dichromate which cannot provide ROS enhancement. This was confirmed by pH-based ROS investigation which shows enhancement only when above pH 7, when Cr(VI) exists as chromate. To preserve this ROS enhancement at biological pH, Tf was added to trap the chromate. While this did increase the retention rate of chromate, the ROS enhancement was only temporarily preserved and was unable to last through the longer oxygen testing. Finally, we describe a possible nano-scale chromate-based trap that can utilize chromate at biological pH.

3.2 Introduction

Electron Injection

Photo-activation of TiO_2 generates excited electrons and holes which can react with molecular oxygen and water to from ROS (Figure 3-1). However, the specific ROS have differing energies and lifetimes, altering their damage patterns.
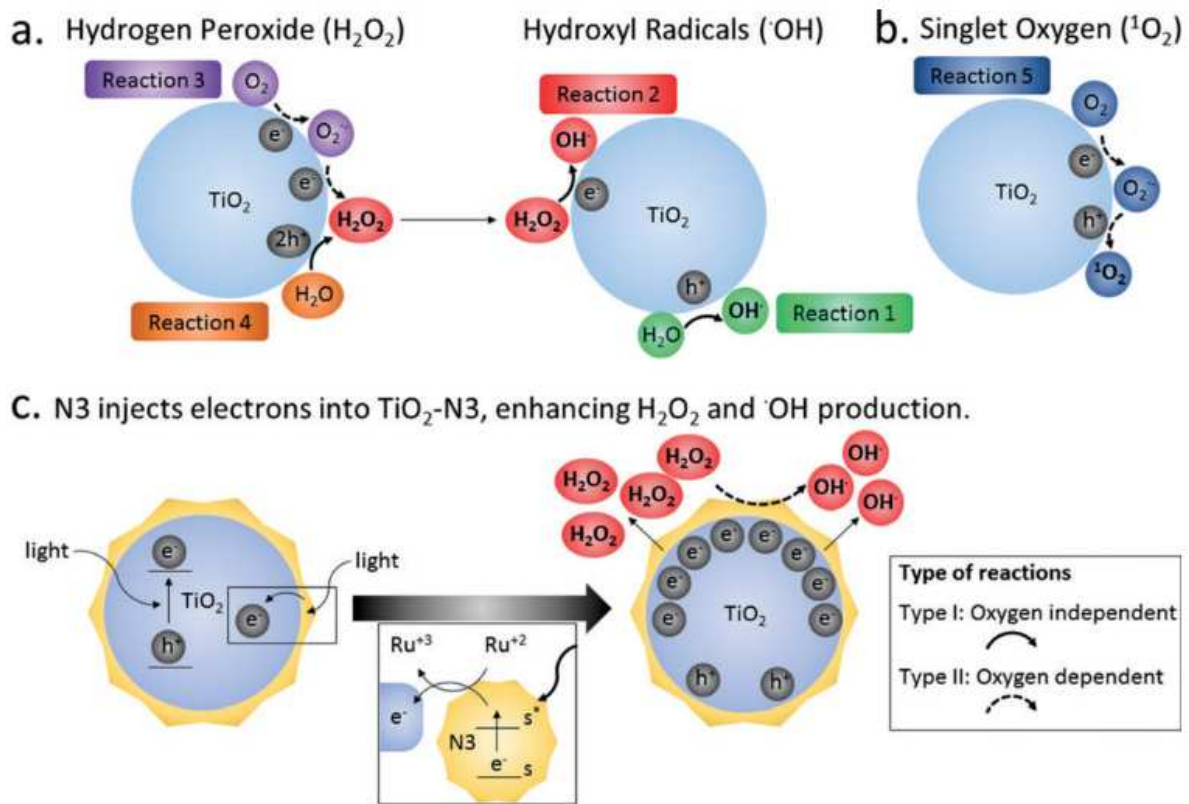
Figure 0-1: TiO_2 ROS generation pathways and their electron and/or hole requirements.
A) Generation pathways for hydroxyl radicals and peroxides. B) Generation path for singlet oxygen. C) Sensitization of TiO_2 using N3 for increased conversion of peroxide to hydroxyl radicals via oxygen independent pathways. Image reprinted from collaboration work with R. Gilson et. al.[122]

The ROS energy can be increased through multiple electron or hole reactions, with one such chain beginning with oxygen's reduction to superoxide, a further reduction to peroxyl radicals before a final electron/hole catalyzed split to hydroxyl radicals. Normally, these additional

electrons/holes come from UV photogenerated excitons, but sensitizers can provide extra electron/hole flux.

Sensitizers can inject photo-excited electrons into a material, a process that requires higher photo-energy than the conduction band edge of an acceptor material. PRaST compatible sensitizers must be able to: 1) bind the surface with geometry conducive to hole injection; 2) be photo-excited at Cherenkov radiation wavelengths (UV-C band); and 3) have sufficient excited hole potential to inject into TiO_2's valance band. Anatase TiO_2 has a bandgap of 3.18 eV with maximum electron and hole potential of -0.52 and 2.53 V vs. SHE, respectively.[70] The best known sensitizers for TiO_2 electron injection are ruthenium-based polypyridyl dyes, such as Ruthenium Black or N3 Dye.[123] Their combination of carbonyl conjugation to TiO_2's surface, multident binding, high photo-excited electron potential make them ideal for sensitization.
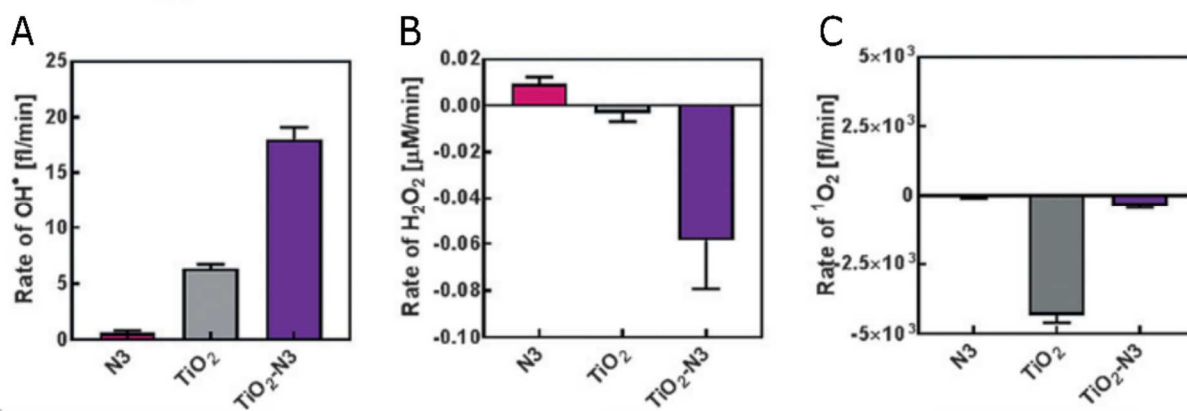
Figure 0-2: Relative ROS generation rates in hypoxic conditions.
A) hydroxyl radical B) hydrogen peroxide and C) singlet oxygen from TiO_2 and TiO_2-N3. This shows a shift away from hydrogen peroxide and towards higher energy hydroxyl radicals by the addition of N3.[122]

These dyes also expand TiO_2's optical absorbance beyond 365 nm and into the visible spectrum, increasing solar efficiency.[90] Recent work within our lab showed the ability of N3 to generate

higher energy hydroxyl radicals in oxygen depleted conditions (Figure 3-2). This was a shift away from lower energy peroxides and more efficient use of the low oxygen levels.

Hole Injection

While N3 increases ROS energy at low oxygen levels, it was still dependent on electron based, oxygen-dependent initiation.[122] An alternative is to use TiO_2 hole oxidation, which uses hydrolysis to generate ROS. Hole injection functions much like the intersystem crossing of electrons, though the sensitizer in question must now have a hole reduction potential higher than the valance band of TiO_2. However, TiO_2's relatively large semiconductor bandgap and highly stable crystal structure results in a large valence band potential (2.27 V vs. SHE). Combined with the other requirements, only two molecules are able to perform hole injection, a ruthenium tri-nuclear cluster, and chromate.[124]

Chromate Reduction Potential and TiO_2 Interaction

Cr(VI) alone has a reduction potential of 0.55-0.6 vs. SHE for its conversion to Cr(V).[125] However, when suspended in water, CrO_4^{-2}, Cr(VI) major species above pH 7, has increased reduction potential of 3.4 V vs. SHE.[126] This ion, known as chromate, has peak absorption at 440 nm with a second UV peak at 350 nm, allowing short wave sensitization typical of Cherenkov light. Finally, chromate is a tetrahedrally coordinated, multi-oxygen structure allowing both hydrogen bonding and Ti defect-ligand interactions. Combined, these factors make Cr(VI) the ideal candidate for hole sensitization of TiO_2.

Cr(VI) also exists in several other states in water depending upon pH and concentration (Figure 3-3A). These have been shown to affect the association to TiO_2, both due to charge

repulsion differences when TiO$_2$ passes through its isoelectric point (pH 6) as well as multiple

oxygen interactions when binding dichromate.[127,128]
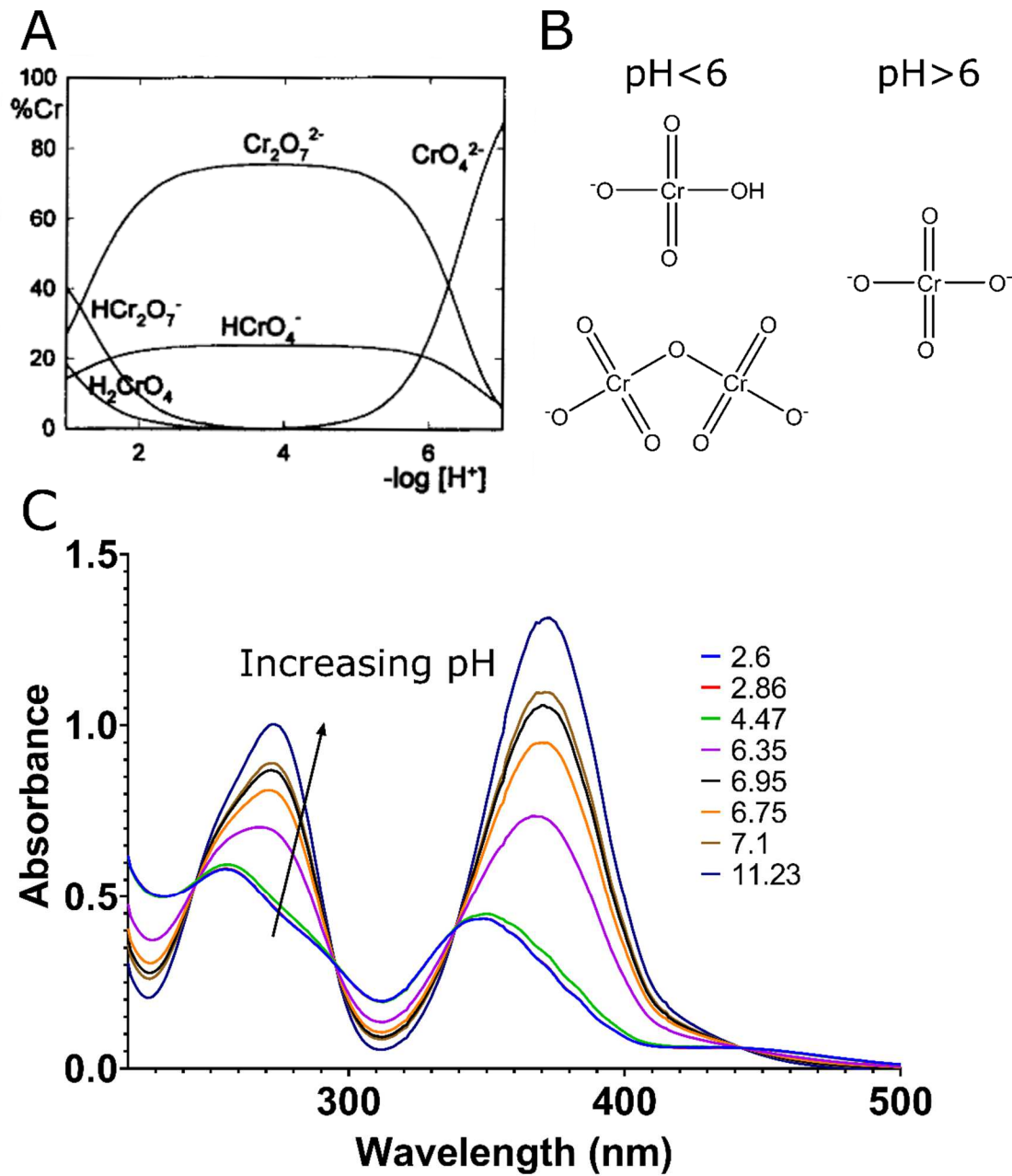
Figure 0-3: Effect of pH on Cr(VI) structure in water.
A) Cr(VI) state by pH in a 30 mM aqueous solution. Chromate being present above pH 6. B) The molecular structure of the various chromate states. C) Spectral data showing the shift in peak absorbance with speciation shifting from dichromate to chromate. A) Reprinted from Brito, F et al.(1997)*[129]*

3.3 Experimental Methods

Materials

Apo-Transferrin was purchased from Athens Research and Technology. All water was deionized to 18.2 MΩ resistance with a MilliQ Direct-Q3 water purification system. P25 TiO_2, potassium dichromate ($K_2Cr_2O_7$), sulfuric acid, Cr(VI) traceCERT ICP standard, diphenylcarbazide Cr(VI) assay kit, dichlorofluorescein diacetate (DCF-DA), NaOH, HCl, Tetraethyl orthosilicate (TEOS), titanium butoxide, hydroxypropyl cellulose (HPC), and 2-(N-morpholino)ethanesulfonic acid (MES) were all purchased from Sigma-Aldrich (St. Louis, MO, USA) without further purification. pH alterations were all carried out with 1N sodium hydroxide (NaOH) or hydrochloric acid (HCl).

TiO_2/Cr Adsorption

TiO_2 was prepared at 10 mg/mL in 2 mM potassium dichromate solution at pH 4.5-5 unless otherwise specified. The solution was then placed in a bath sonicator for 10 min before transferring to a rocking table overnight at room temperature (r.t.). Excess dichromate was removed through centrifugation-washing at 10k relative centrifugal force (rcf) for 10 min before resuspending in water. After decanting, the vials were cooled to -80 °C before lyophilization on a Savant SpeedVac overnight. Samples were stored in the dark at r.t. and new stocks were made after 2 weeks to limit Cr(VI) to Cr(III) surface conversion.

Transferrin was coated to TiO_2/Cr particles according to the protocol by Kotagiri et al.[51] Briefly, Tf-TiO_2/Cr was generated in water by dissolving a 3:1 mass ratio of Tf and TiO_2/Cr. The

sample was then probe sonicated at 4 W until the temperature reached 50 □C, followed by

filtering through a 0.22 μm PES syringe filter.

Cr Adsorption Quantification

Adsorption efficiency was determined in several ways. First, the absorption spectra were

investigated at 250 and 350 nm on a Beckman-Coulter 640 UV-Vis spectrophotometer (Brea,

CA, USA). The change in supernatant absorbance after the 1st wash was used to quantify the

absorbance against $K_2Cr_2O_7$ standards. To eliminate possible chromium state change by TiO_2, all

chromium on purified particles was quantified via a PerkinElmer Elan DRCII ICP-MS

(Waltham, MA, USA). TiO_2/Cr samples were digested in sulfuric acid at 280 °C for 1 hr. If any

residue remained within the vials, they were further heated to 320 °C for an additional 30 min.

All vials were precleaned for 10 min at 320 □C with sulfuric acid. The samples were then

diluted to 1% sulfuric acid with water and run against Cr(VI) standards.

Quantification of Cr(VI) ion concentration was performed with a Diphenylcarbazide

based assay kit. All samples (250 µL) contained at least 1 mg/mL TiO_2/Cr, which were then

diluted with 50 µL of the combined assay and incubated for 20 min at r.t. TiO_2 was then

precipitated by centrifugation at 10k rcf for 10 min and the supernatant was tested at 480 nm in a

96 well plate on a Biotage Neo2 plate reader (Uppsala, Sweden).

Tf-TiO₂/Cr Properties

Particle size and surface potential were determined on a Malvern Zetasizer Nano-ZS

(Malvern, UK) in PBS. Size measurements were confirmed with a JOEL JEM-1400Plus TEM

(Peabody, MA , USA) at 120 kV on a formvar carbon grid (Ted Pella, Redding, CA, USA). To

visualize protein coating on the Tf-TiO₂/Cr NPs, the grids were further stained with uranyl

acetate at 2% in water, incubating for 3 min before washing to limit uranyl acetate recrystallization. Bandgap was determined using diffuse powder reflectance UV-vis spectroscopy (Horiba Fluorimeter and attached Quanta-ϕ integrating sphere, Kyoto, Japan). A Spectralon scattering blank was used to calibrate the sphere before dry powdered TiO_2/Cr was run in a sample cup with a quartz coverslip, integration time 0.5 sec.

ROS Quantification

ROS production was measured by DCF-DA conversion and driven by a medium pressure 365 nm center wavelength UV lamp. DCF-DA was activated to DCF by incubating 5.55 mM DCF-DA in DMSO with 1 N NaOH for 15 min (final concentration of 5mM). DCF was then added to all samples at 5 μM final concentration. Samples were run at 0.01 mg/mL of $Tf-TiO_2/Cr$ NPs in 96 well plates with 150 μL per well and arranged such that the average UV power was 1 mW/cm^2 for the activation duration. Sample readings were excited at 495 nm and emission was detected at 525 nm (20 nm slit window) every 80 seconds of UV exposure for 30 min. Results were reported as pseudo first-order rate constants.

Anaerobic ROS Production

ROS production was quantified using DCF as above in an oxygen-depleted glove chamber. Argon was used to decrease atmospheric O_2 below 1% and the plate was rocked for 20 min to reach equilibrium. Using a slit for the UV lamp, a row of wells was exposed to 0.7 mW/cm^2 for an allotted time. After exposure, the plate was removed and imaged on the plate reader. Experiments under normoxic conditions were also performed within the glove box, equilibrated to atmospheric oxygen. Oxygen levels were quantified via an Ocean Optics NeoFox sensor fitted with a FOSPOR probe (Orlando, FL, USA).

Silica Generation

Silica NPs were generated following the Stöber method. Briefly, 2 g TEOS was added quickly to a solution of 30% ammonia (10mL), distilled water (11mL) and ethanol (75mL) under heavy stirring. This solution was left overnight at r.t. and the resulting silica particles were purified via centrifugation and washing with one round ethanol and two rounds di-water. The final powder was then lyophilized and stored at r.t.

TiO$_2$ Shell Formation

TiO$_2$ was coated onto the silica NPs via sol-gel coating. 10 mg/mL silica in anhydrous ethanol was dispersed well via sonication. To this was added dissolved HPC in water to a final concentration of 3 mg/L HPC and 0.5 M di-water. Titanium butoxide dissolved in ethanol at 0.6 g/mL was added dropwise to the solution under heavy stirring over 1 hr, final concentration of 57 mg/mL. The solution was then sealed and heated to 85 °C for 1.5 hr. The resulting TiO$_2$-silica was then purified through centrifugation and washing with ethanol.

Silica etching was done with 3 mg/mL resuspended particles in 50 mL di-water. The solution pH was raised to 12 and sonicated to homogeneity. The solution was then transferred into a pressure vessel which was then heated to 140 °C for 6 hr. After cooling the solution was purified via centrifugation against di-water. The final cores were imaged on TEM and size analyzed with Image-J.

TiO$_2$ Shell/Cr Coating

TiO$_2$ shells at 1 mg/mL were coated with pyridium chlorochromate at 50 mM. The pH was raised to >10 and mixed via stir bar overnight. The solution was then purified via multiple centrifugation-washes.

3.4 Results and Discussion

Adsorption of Cr(VI) to TiO$_2$

Adsorption was investigated across a range of pH, sampling the major Cr(VI) states, namely dichromate, chromate, and chromic acid. Figure 3-4A shows the remaining percentage of a 2 mM chromate solution exposed to TiO$_2$ at 10 mg/mL from pH 2.5-11.5. Low pH produced visibly yellowed TiO$_2$ with direct measurement of the supernatant (controlled for changes in spectra) showing a Cr(VI) concentration loss of -6.3 ± 0.42 μmol K$_2$Cr$_2$O$_7$/(g TiO$_2$*pH Cr(VI). Biding was also linearly dependent on TiO$_2$ concentration (Figure 3-4B). The standardized coating condition was then set to pH 5, corresponding to 1.00 ± 0.08 μg/mg TiO$_2$ by ICP-MS.

Diffuse reflectance spectroscopy (Figure 3-4C) shows a red shift in TiO$_2$/Cr's spectra in the range of 350-500 nm when freshly coated. The peak increase in absorbance occurred at 430 nm suggesting dichromate adhesion, the major state of Cr(VI) at pH 5. Prolonged dark storage of TiO$_2$/Cr showed a loss of this shoulder and shifting absorbance to 600 nm. This absorbance corresponds to Cr(III), a well-known conversion sought after in industrial waste catalysis.[130] This conversion to Cr(III) is drastically increased by UV exposure (Figure 4-1A). Analysis of this coatings stability over time was carried out via diphenylcarbohydrazide assay which is selective for Cr(VI). TiO$_2$ is known to have background catalytic activity without light activation and this generation seems to reduce Cr(VI) to Cr(III) over time. Cr(VI) levels decreased with increased storage time at a rate of 0.65 ± 0.03 % initial bound chromate per day. Using this information variations in the amount of chromate remaining on the particles was maintained within 10% by regenerating the particles every two weeks.
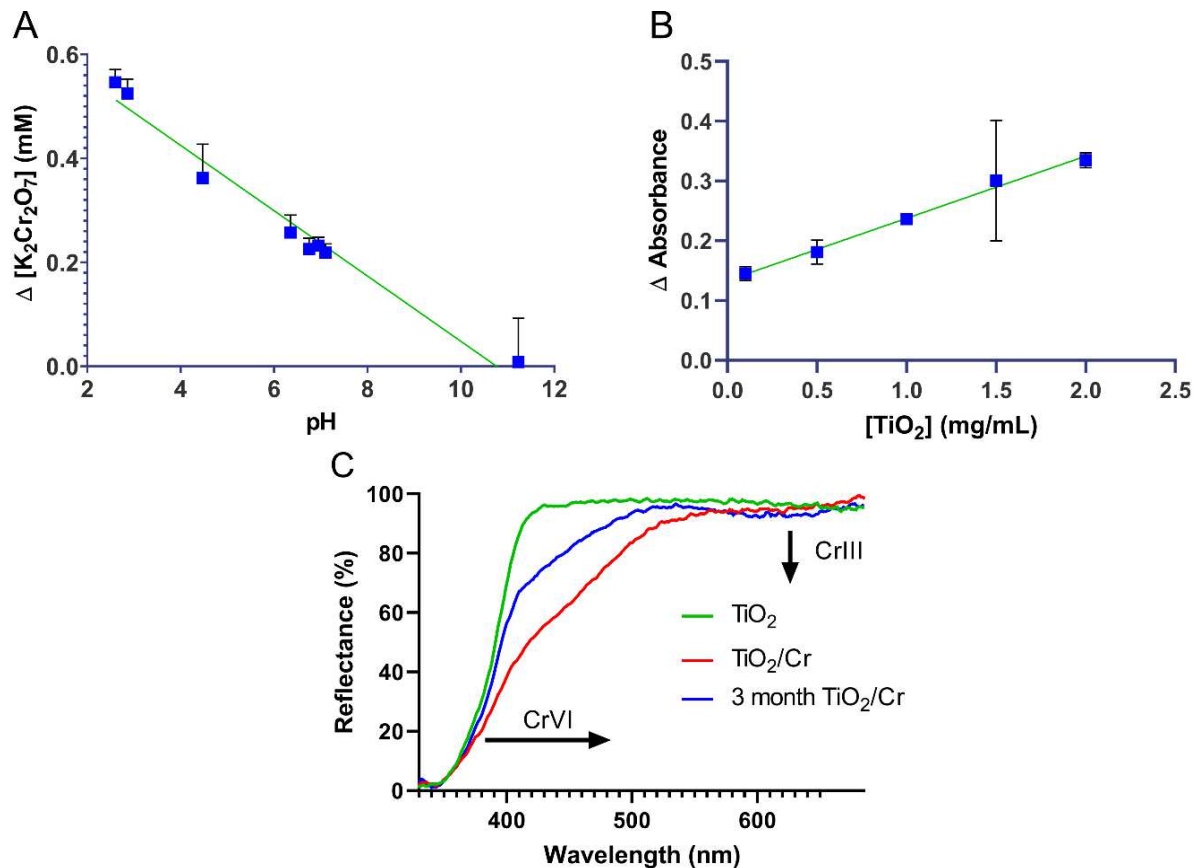
Figure 0-4: Coating of TiO$_2$ with Cr(VI).
A) The concentration removed from 2 mM K$_2$Cr$_2$O$_7$ solution upon incubation at various pH against 10 mg/mL TiO$_2$, indicating surface adsorbance. B) Change in 2 mM K$_2$Cr$_2$O$_7$ absorbance upon addition of various amounts of TiO$_2$, showing concentration dependence. C) Diffuse reflectance spectra of TiO$_2$/Cr construct coated at pH 5 in powder mode.

Tf-TiO$_2$/Cr Solution Properties

Coating with Tf increased particle stability with a hydrodynamic diameter of 209.2 ± 6.71 nm and a PDI of 0.182 ± 0.016. This size parallels existing Tf-TiO$_2$ formulation though has a radical shift in zeta potential from 20 ± 0.83 mV to -4.34 ± 0.732. This shift also shows an association of the chromate ions beyond electrostatic effects, pushing the zeta potential over neutral. Once filtered the final particle size is 169.3 ± 4.19 nm with a PDI of 0.092 ± 0.018 (Figure 3-5A). TEM showed the particles mirror the NAG structure of Tf-TiO$_2$, being monodisperse (178.4 ± 76.9 nm, Figure 3-5B) which improves when filtered (94.3 ± 8.73 nm,

Figure 3-5C). When stained with uranyl acetate (Figure 3-5E) Tf appeared as a coating, filling in

the gaps within the NAG structure as well as on the surface ~5-10 nm in depth, indicating a

monolayer (hydrodynamic diameter of Tf = 4-5 nm).[131]
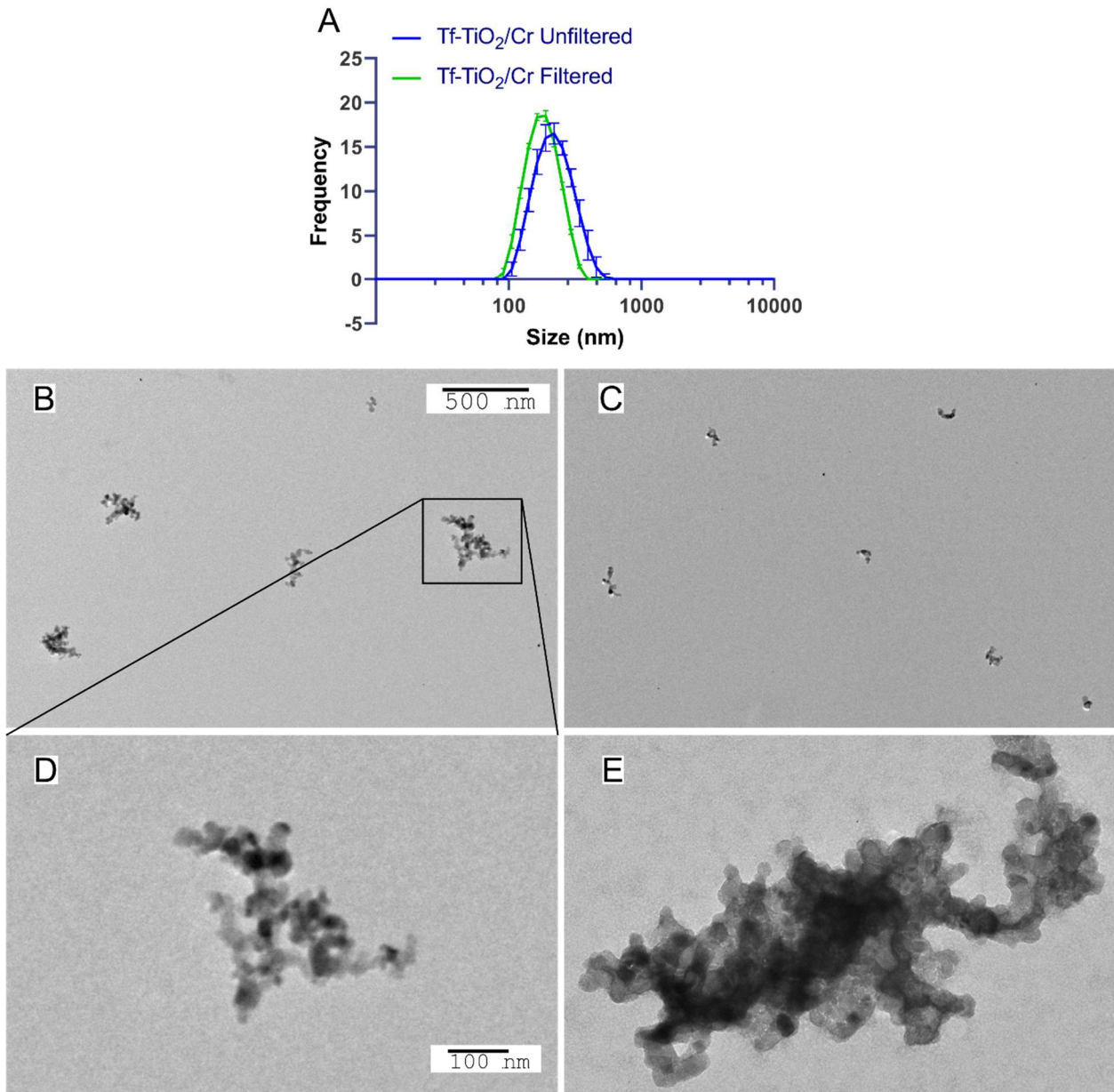
Figure 0-5: TiO$_2$/Cr particle structure.
A) DLS intensity distribution of Tf-TiO$_2$ /Cr filtered and unfiltered. B) Representative TEM images of Tf-TiO$_2$/Cr unfiltered. C) Representative TEM images of Tf-TiO$_2$/Cr filtered. D) Zoom in view of Tf-TiO$_2$/Cr unfiltered. E) Zoom in view of Tf-TiO$_2$/Cr unfiltered, stained with uranyl acetate for Tf visualization.

ROS Generation from TiO$_2$/Cr

With a standardized particle generation method, the effect on ROS generation was investigated under UV light exposure. Chromate itself showed low DCF conversion (Figure 3-6B) against UV light. Additionally, the standardized Tf-TiO$_2$/Cr showed a slight <u>decrease</u> in ROS generation rate (Figure 3-6A) in both hypoxic and normoxic conditions. This is likely due to dichromate reduction to lower ionic states, consuming photo-excited electrons in non-ROS generating reaction. As the Cr(VI)/(V) and O$^{II/I}$ photo-excitation is the primary charge separation mechanism, it appears the bridging oxygen in dichromate lowers the energy of the photo-generated hole. As mono-chromate had been proven an effective hole donor, the experiment was rerun from pH 3-10 without Tf and in excess Cr(VI). At pH 10 there was a clear increase in the ROS generation from TiO$_2$/Cr, whereas the other conditions showed no statistical difference with bare TiO$_2$ (Figure 3-6D). This suggested the ROS generation exists only from the mono-chromate state. As indicated above, however, adsorption is limited to lower pH, where dichromate or chromic acid dominates

To trap chromate to the surface of TiO$_2$, Tf was coated onto the surface after a single spin centrifugation of pH 10 TiO$_2$/Cr. Trapping showed increased ROS generation capacity of Tf-TiO$_2$/Cr relative to adding Tf before incubating against pH 10 chromate solution which would not sterically trap any chromate to the surface (Figure 3-6B).
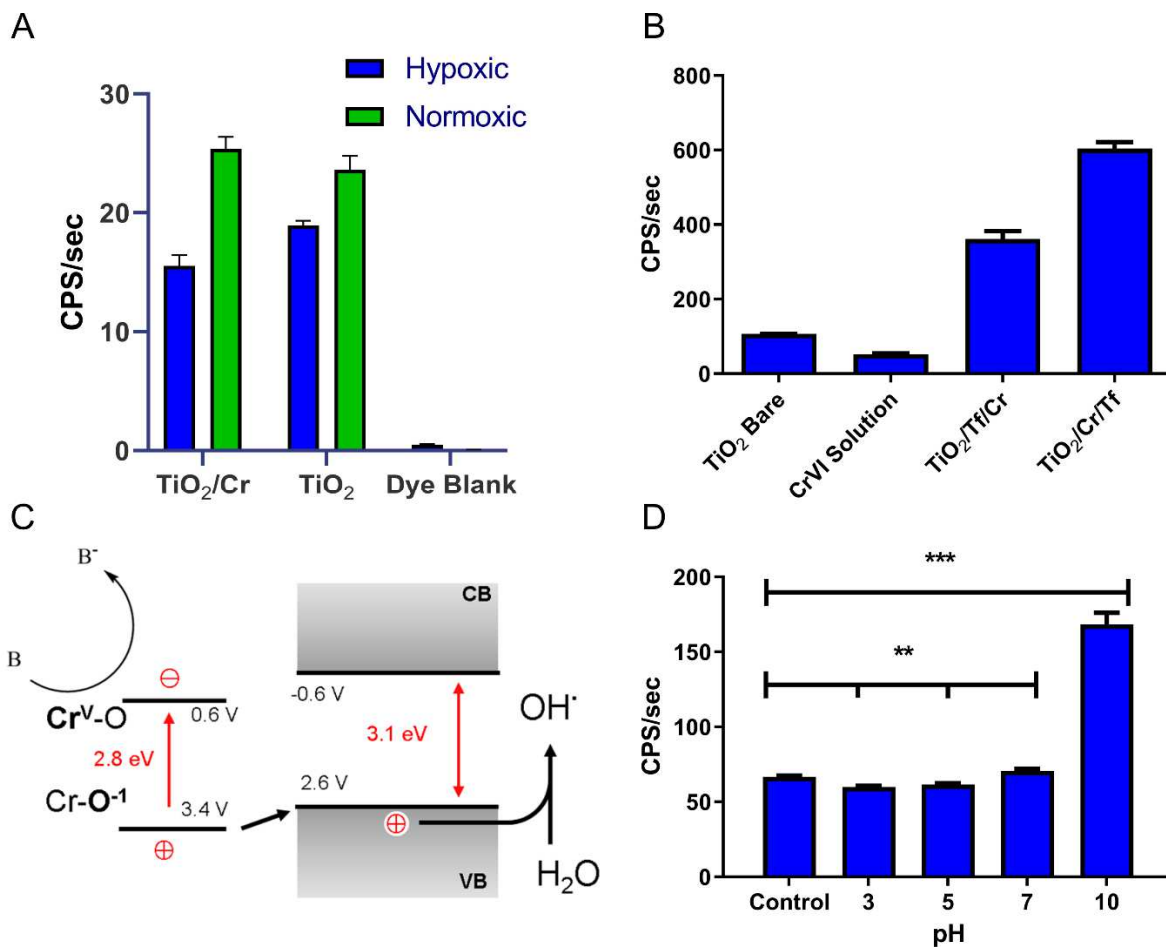
Figure 0-6: ROS generation from TiO_2/Cr.
A) ROS generation by pH 5 coated TiO_2/Cr in hypoxic and normoxic conditions. B) ROS generation rate of Tf-TiO_2/Cr to compare trapping to TiO_2 surface. C) Cartoon of hole donation energies from chromate into TiO_2's valence band. ROS generation by TiO_2/Cr coated in excess chromate conditions by pH. D) The order of coating by chromate at pH 10 either before or after Tf coating is indicated by the order of names.

While the coating of TiO_2/Cr at pH 10 with Tf did improve the ROS generation it was found that this increase was unstable over time (not shown) making this impractical as a mechanism for the current iteration of TiO_2/Cr. This made the generation of an alternative structure necessary to trap chromate.

TiO_2 Shell Synthesis

The size of silica NP generated by the Ströber process was determined via TEM analysis to be 203 ± 3.65 nm (Figure 3-7A). These were then coated with TiO_2 which increased the

particle size to 344.5 ± 6.8 nm (Figure 3-7C). When etched, the shells fused into mesoporous

amorphous TiO_2 with a shell thickness of 70 nm. The shells showed no apparent crystal structure

via HR-TEM or electron diffraction measurements.
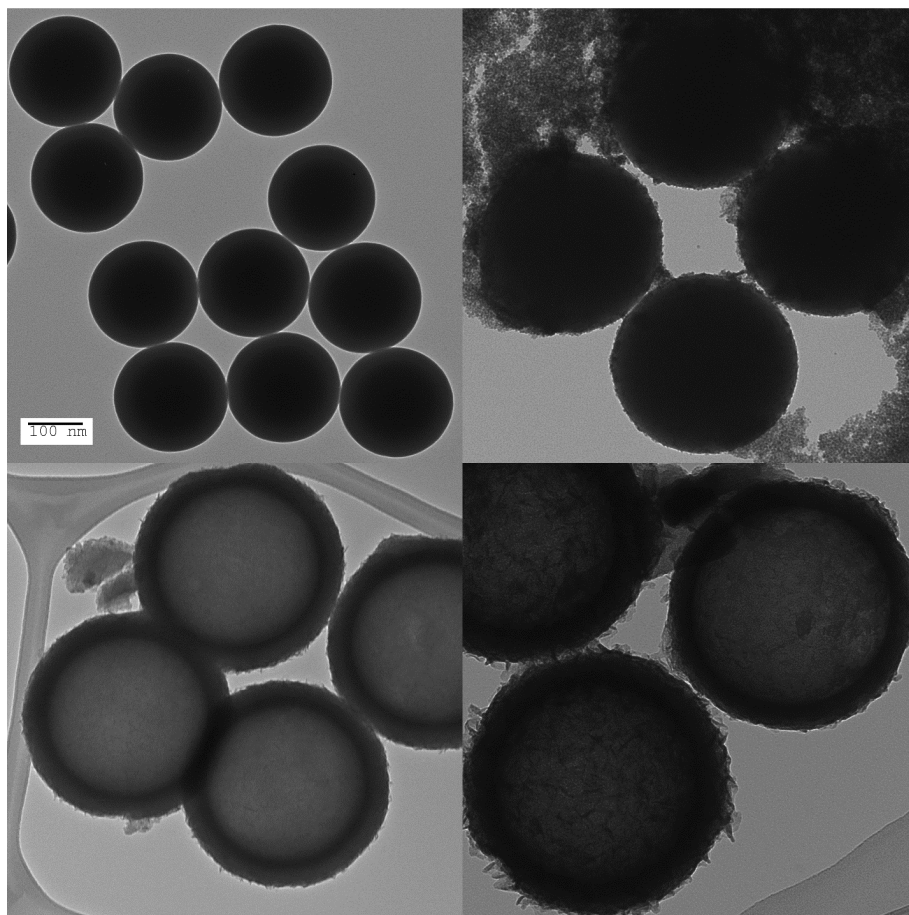
Figure 0-7: TiO_2 shell stepwise TEM.
TEM images of each step of shell creation, A) Bare silica particles, B) TiO_2 coated particles. C) TiO_2 shells post silica etch. D) Chromate coated shell. Patches of increased contrast indicate areas of Cr addition. All images set to 100 nm scale bar.

TiO_2 Shell/Cr ROS Properties

The adhesion of chromate was far lower for TiO_2 Shell/Cr which remained optically

white after full purification, as opposed to the yellowing of TiO_2/Cr. This was also seen in the

ROS generation which showed an initial ROS increase in excess chromate conditions, but this

was stripped after purification. Additionally, the shells showed almost no ROS generation

themselves. This is primarily caused by a lack of calcination and any cohesive crystal structure. Without calcining the shells exist as an agglomerate of 3 nm average TiO_2 cTds which suffer heavily from quantum confinement, limiting their activation.
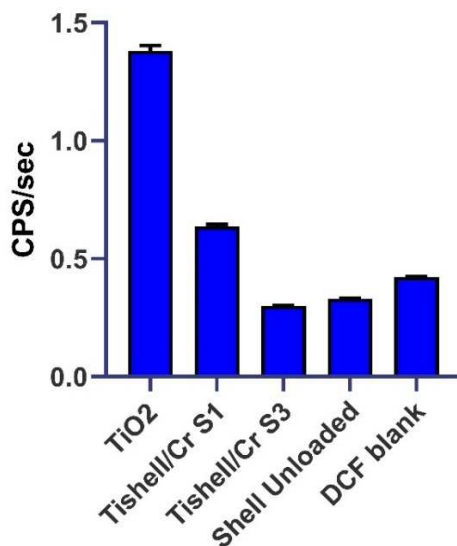
Figure 0-8: ROS generation from TiO_2 shell/Cr particles.
Cr coating was done at pH 10 followed by centrifugation purification. The number of spins is denoted by S#. 25nm TiO_2 controls included for reference.

3.5 Conclusion

The generation of Tf-TiO_2/Cr particles was successfully standardized, forming structurally similar NAGs to those generated for initial PRaST invesitgation. However, the ability of these particles to improve the oxygen dependence in biologically relevant pH appears limited. Adhesion of Cr(VI) to the surface of the particles is severely limited at circulation pH (7.4) and the stability of Tf trapped chromate at that pH. Generation of the shell structure shows promise but requires investigation of calcination effects on both chromate and shell structure. Should chromate trapping can be achieved, however, it will provide an effective sensitizer for TiO_2 phototherapy.

47

Chapter 4: TiO$_2$/Cr State Change Therapy

4.1 Chapter Summary

Metallo-therapies are an effective method for cancer treatment, utilizing compounds from cisplatin to arsenic trioxide.[132,133] The development and coating characteristics of TiO$_2$/Cr, though unable to directly enhance ROS at biological pH, does provide a major avenue for Cr(VI) delivery. As Cr(VI)'s cellular toxicity mechanism stems from ROS generation, its combination with PRaST can further imbalance cellular redox.[134] Here we show TiO$_2$/Cr has a release profile of 1 hrs in sink conditions and 4 hrs in cell culture. Experimental investigation of Tf-TiO$_2$/Cr against cell culture shows enhanced toxicity relative to free Cr(VI) (LC50 0.0173 µg/mL v 11 µg/mL[135]), suggesting improved cellular uptake of Cr(VI) as TiO$_2$ alone shows no toxicity within this range. Finally, mouse PRaST studies show a 60 % reduction in tumor size compared to no radiation controls.

4.2 Introduction

Cr(VI) Metabolism and Toxicity

Cr(VI) species is a well-known carcinogen within mammalian cells, with evidence of DNA chelation and ROS production.[136] Cr(VI)'s toxicity stems from its high solubility in water and cellular permeability, passing through the mixed anion transporter.[137] Once there it reacts quickly with cellular anti-oxidants, namely glutathione and ascorbate (vitamin C), on the order of 8 min to total reduction of Cr(VI).[138] The reduction generates Cr(V), a unstable state, detected through electron paramagnetic resonance and known for its Fenton-like reaction, catalytically

splitting peroxides to hydroxyl and peroxyl radicals.[139] This reaction generates a large amount of ROS in the vicinity of the mitochondria, activating ROS-initiated P53 signaling pathways.[140] In addition, this eventually produces Cr(III) which is known to chelate DNA.[138]

TiO$_2$ Photocatalytic Cr(VI) Conversion

The reduction of Cr(VI) by TiO$_2$ is a well-studied mechanism used to purify wastewater from industrial processing.[141–143] Under heavy irradiation this rapidly converts Cr(VI) to Cr(III) which then is precipitated from solution as Cr(III)(OH)$_x$ at pH 7. We seek to use this conversion to deliver and generate Cr(V) to cells to supplement existing PRaST.

4.3 Experimental Methods

Stock TiO$_2$/Cr Generation

TiO$_2$/Cr generation was standardized from results in chapter 3. Briefly, pH 4.5-5 aqueous solution with 10 mg/mL P25 TiO$_2$ and 2 mM potassium dichromate was probe sonicated for 10 min on ice at 4 watts before transferring to a rocking table for an additional hour. Excess dichromate was removed through centrifugation. The TiO$_2$/Cr was then lyophilized on a Savant SpeedVac overnight before weighing and storage. Samples were stored in the dark at r.t. and stocks were replenished every 2 weeks.

Cr(VI) to Cr(III) conversion

Direct confirmation of chromium conversion was evaluated through a closed reactor design. 1 mg/mL TiO$_2$/Cr in PBS (pH 7.1) was placed in a 100 mL beaker with a 9 W medium pressure UV lamp (Coospider Sun JUP-01), positioned centrally within the liquid. The solution pH was adjusted to 2 to prevent Cr(III) precipitation. The solution was then homogenized and

stirred for 24 hr. Reactor aliquots were taken, washed via centrifugation and UV-vis spectra were recorded. The solution pH was then increased to 10, precipitating Cr(III) to its hydroxide form, normally present at pH 7.4. The reactor was then UV stimulated for another 24 hrs and samples were tested the same way as above. The decrease of the chromate feature peak at 350 nm and the appearance of the Cr(III) feature peak at 580 nm from the sample solutions were quantified.

The pH conversion rate over Tf-TiO$_2$/Cr particles was confirmed using a 10 mg/mL solution of the standard TiO$_2$/Cr in MES or PBS buffer from 5-7.5 pH. These solutions were placed in 2 mL microcentrifuge tubes and exposed to a 365 nm UV light (1 mW/cm^2) for 30 min. Cr(VI) conversion was then verified through the Cr(VI) assay kit.

TiO$_2$/Cr Sink Release

Cr(VI)'s adsorption stability was quantified via dialysis against 1L PBS. 10 mg/mL TiO$_2$/Cr was placed in a 3,500 MW cutoff SnakeSkin Dialysis membrane (Thermo-Fischer Scientific, Waltham, MA, USA). The first 200 μL samples were taken after 10 min and then every hour for 8 hours. The Cr(VI) concentration was confirmed with Cr(VI) assay kit.

***In Vitro* TiO$_2$/Cr Toxicity and Stability**

In vitro cellular studies were performed on HT1080 fibrosarcoma cells. Cells were cultured at 5% CO$_2$ within a 37 °C humidified incubator. All studies were performed in 24 well clear corning plates, seeding 25,000 cells per well in 800 μL of DMEM supplemented with 10% fetal bovine serum, L-glutamine (2 mM), penicillin (100 units/ml) and streptomycin (100 μg/ml). Tf-TiO$_2$/Cr was generated as previously described and added to cell plates from PBS stocks at 1 mg/mL. Cells were given at least 12 hours to attach before a concentration dose response curve was generated from 0-100 μg/mL. Total incubation time of Tf-TiO$_2$/Cr in culture was 2.5 days

before survival was determined using Promega AQueous One Cell Proliferation Assay (MTS). To avoid scattering effects on the colorimetric assay, the plate was hand agitated and the particles removed from the well, followed by backfilling with 800 µL PBS and 60 µL MTS assay in each well. The assay was incubated for 30 min before 200 µL was transferred to a 96 well plate and measured on a Biotage Neo plate reader at 480 nm.

Cr(VI) release toxicity was quantified from a 100 µg/mL Tf-TiO$_2$/Cr sample, and cells were cultured in the same way as described above. After incubating for the desired time, the plates were shaken to re-suspend any settled particles and the media was removed. 800 µL of fresh media was added to replace removed volume in the well, and total incubation time was 2.5 days.

In Vivo Tumor Therapy

All studies were conducted in compliance with Washington University Animal Welfare Committee's requirements for the care and use of laboratory animals in research. Lewis Lung Carcinoma (LLC) cells were implanted subcutaneously into the flank of FOX Chase SCID Beige mice at a concentration of 1×10^6 cells per tumor. Once the tumors became palpable, the tumor size was measured before they were injected with 30 µL of Tf-TiO$_2$/Cr or Tf-TiO$_2$ at 1 mg/mL intratumorally. For radiation treatment, 24 hrs post particle injection a dose of 31 MBq of FDG in 85 µL was intraperitoneally injected after 6 hrs of fasting. Along with controls, 5 treatment groups were evaluated (n = 4/group): (1) untreated controls, (2) Tf-TiO$_2$/Cr alone, (3) Tf-TiO$_2$ alone, (4) Tf-TiO$_2$/Cr + FDG, and (5) Tf-TiO$_2$ + FDG. The mouse weight and any physical signs for distress were monitored closely, and mice were euthanized by cervical dislocation after anesthesia with 5% isoflurane when the tumor size reached 2 cm.

51

4.4 Results and Discussion

Cr(VI)->Cr(III) Conversion

Evidence of TiO_2/Cr reduction of Cr(VI) to Cr(III) was present in the diffuse reflectance spectra of long stored TiO_2/Cr stocks (Figure 3-4A). However, this represented passive conversion at a timescale beyond that of any therapy. To confirm active conversion a closed batch reactor with excess Cr(VI) was tested against TiO_2. The pH was lowered to pH 2, facilitating strong TiO_2/Cr binding as well as limiting Cr(III) precipitation. 24 hrs exposure showed a 90 % reduction in Cr(VI) signal and the emergence of a Cr(III) peak at 550 nm (Figure 4-1A). To test for the regeneration of $Cr(III)(OH)_3$ to chromate the reactor pH was adjusted to 10 before again treating the reactor for 24 hrs. This returned the level of Cr(VI) to 25% initial values and indicated reactions in both directions take place on TiO_2. To confirm Cr(VI) can be reduced from the TiO_2/Cr NAGs at biological pH, the Cr(VI) conversion was tested at 5.5-7.5 with MES and PBS buffer (Figure 4-1B). This showed conversion was independent of pH but did appear to change with buffer. Spectral analysis of the supernatant showed no visible Cr(III) signal, however, meaning most of the chromium was likely in Cr(V) or Cr(IV) state which are Fenton-like reagents. The independence of conversion rate on pH is likely due to pre-adsorption of Cr(VI), removing binding affinity as a factor in solution for Cr(VI) conversion. The choice of buffer did affect the conversion rate, however, due to a combination of the increased UV absorption by MES and possible ROS quenching by MES's tertiary amine.
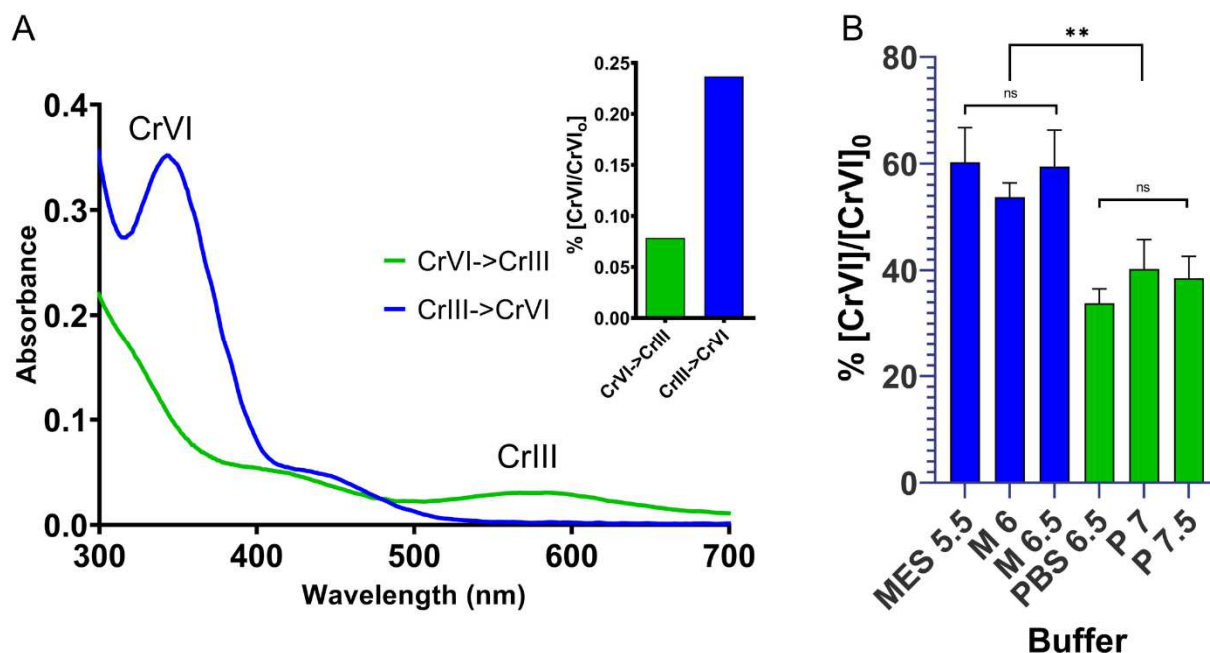
Figure 0-1: Chromium conversion from Cr(VI) to Cr(III).
A) Spectra of batch reactor conversion of Cr(VI) to Cr(III) (green) at pH 2 followed by recovery of Cr(VI) at pH 10 (blue). Insert is the remaining Cr(VI) concentration after each reaction. B) Cr(VI) conversion from TiO2/Cr in 2 different buffers, MES and PBS, at various pH Reported as % initial values. **$P < 0.01$.

Chromate Shedding and Cellular toxicity

With effective UV conversion of Cr(VI) to reactive lower states, TiO$_2$/Cr particles unstimulated release rate and toxicity was investigated. Using dialysis against PBS of the standardized TiO$_2$/Cr coating, the release half-life was 1.04 ± 0.06 hrs vs. 0.19 ± 0.01 hrs for Cr(VI) alone. As this is in sink conditions, we postulated this rate would be slowed in cell culture when in the full Tf-TiO$_2$/Cr formulation, both due to steric trapping as indicated in the ROS experiments and the lower volume of culture.

As Cr(VI) is a known toxin, the cellular response had to be verified before any *in vivo* toxicity/PRaST experimentation. HT1080-RFP cells were stressed against Tf-TiO$_2$/Cr at 100 µg/mL, the concentration often used for cellular PRaST, with significant killing observed. As a result, a dosing ladder was used to find the ideal range for Tf-TiO$_2$/Cr in cell culture. The EC50

value for Tf-TiO$_2$/Cr was 17.3 ± 0.62 µg/mL (Figure 4-2C), while Tf-TiO$_2$ showed no toxicity

up to 1000 µg/mL, as previously reported.[51] Interestingly, potassium dichromate solution at 34

µM was required to reach the same toxicity as 0.34 µM on Tf-TiO$_2$/Cr. This suggests Tf-TiO$_2$/Cr

conjugated drastically increase the toxicity of the released chromate. This is possibly driven by

intracellular trafficking of the Cr(VI) through the transferrin receptor or dark catalytic conversion

to unstable Fenton-like reagents Cr(V) and Cr(IV) by TiO$_2$.
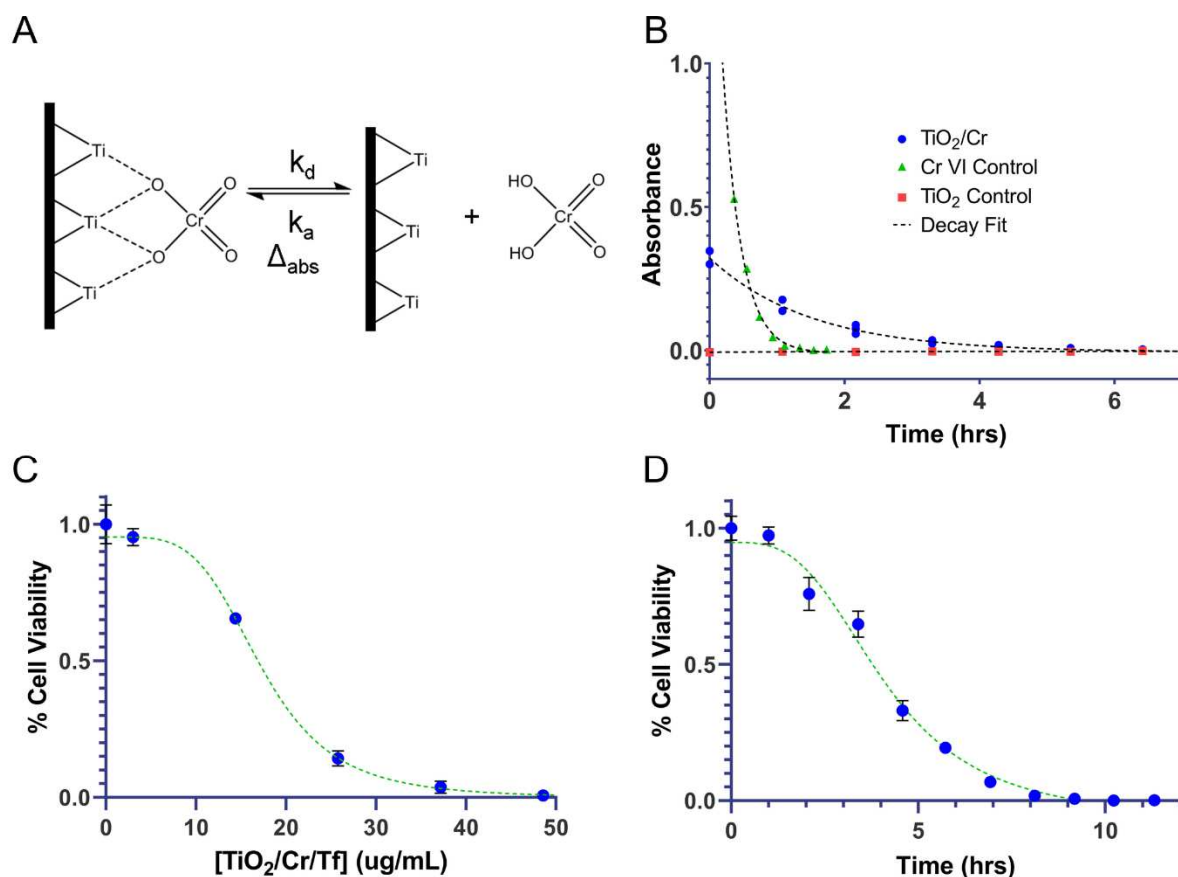
Figure 0-2: Cr(VI) release rate and toxicity for TiO$_2$/Cr.
A) Diagram for equilibrium stability of chromate on TiO$_2$. B) Release rate of Cr(VI) from TiO$_2$/Cr against sink dialysis conditions. Included for comparison are free Cr(VI) and bare TiO$_2$. Decay fits are indicated by dotted lines and are source of half-life parameter. C) Dose response curves for TiO$_2$/Cr against HT1080 cells. D) Incubation time response curve for TiO$_2$/Cr. Response determined through sigmoidal fit (green dashed line).

To test if this enhanced toxicity was related to the release of the chromate, an incubation time series was run using 100 µg/mL Tf-TiO$_2$/Cr. This showed that an incubation time of 4.094 ± 0.22 hrs led to 50% cell death (Figure 4-2D). Previous investigations against chromate in cell culture have shown the reduction time for chromate intracellularly to be ~8.5 min.[132,138] Additionally, these studies showed full reduction effects in viability before 3 hr. There reports indicate the lag in toxicity is driven by the Tf-TiO$_2$/Cr NAGs themselves.

In Vivo **Tf-TiO$_2$/Cr PRaST**

Further investigation of the effect of Cr(VI) toxicity on PRaST was carried out *in vivo* in an aggressive LLC subcutaneous mouse model. TiO$_2$ samples were administered via intratumoral injection to limit the effect of non-specific liver uptake and potential chromate toxicity for the initial study. FDG (31 MBq) was systemically administered 24 hrs after particle injection and the tumor size tracked via caliper (Fig 6). Tf-TiO$_2$/Cr showed substantial tumor growth inhibition both with (10% control, p=0.0005) and without (24% control, p=0.046) FDG treatment two days after injection. This is relative to Tf-TiO$_2$ with a single dose of FDG producing no significant difference relative to control. This tumor suppression persisted beyond the 24 hrs, after FDG decay. While the increased tumor suppression of Tf-TiO$_2$/Cr with or without FDG was not statistically significant, optimization of the dosage regimen or use of a longer-lived beta emitter could improve the efficacy of treatment response by PRaST. Systemic toxicity outside of the tumor region was negligible with no statistical decrease in tracked weight showed over the time of study (Figure 4-3B). This was expected as the dose of Cr(VI) is well below toxicity limit in mice and rats.[144] Further investigation of toxicity will be required, focusing on alterations in TiO$_2$/Cr trafficking relative to free Cr(VI), especially in the liver. While the increased tumor

55

suppression of Tf-TiO$_2$/Cr with or without FDG was not statistically significant, the combination of Tf-TiO$_2$/Cr and FDG did provide the largest suppression of any treatment, and future higher-powered studies with an optimized dosage regimen using a longer-lived beta emitter could improve the efficacy of treatment response by PRaST.
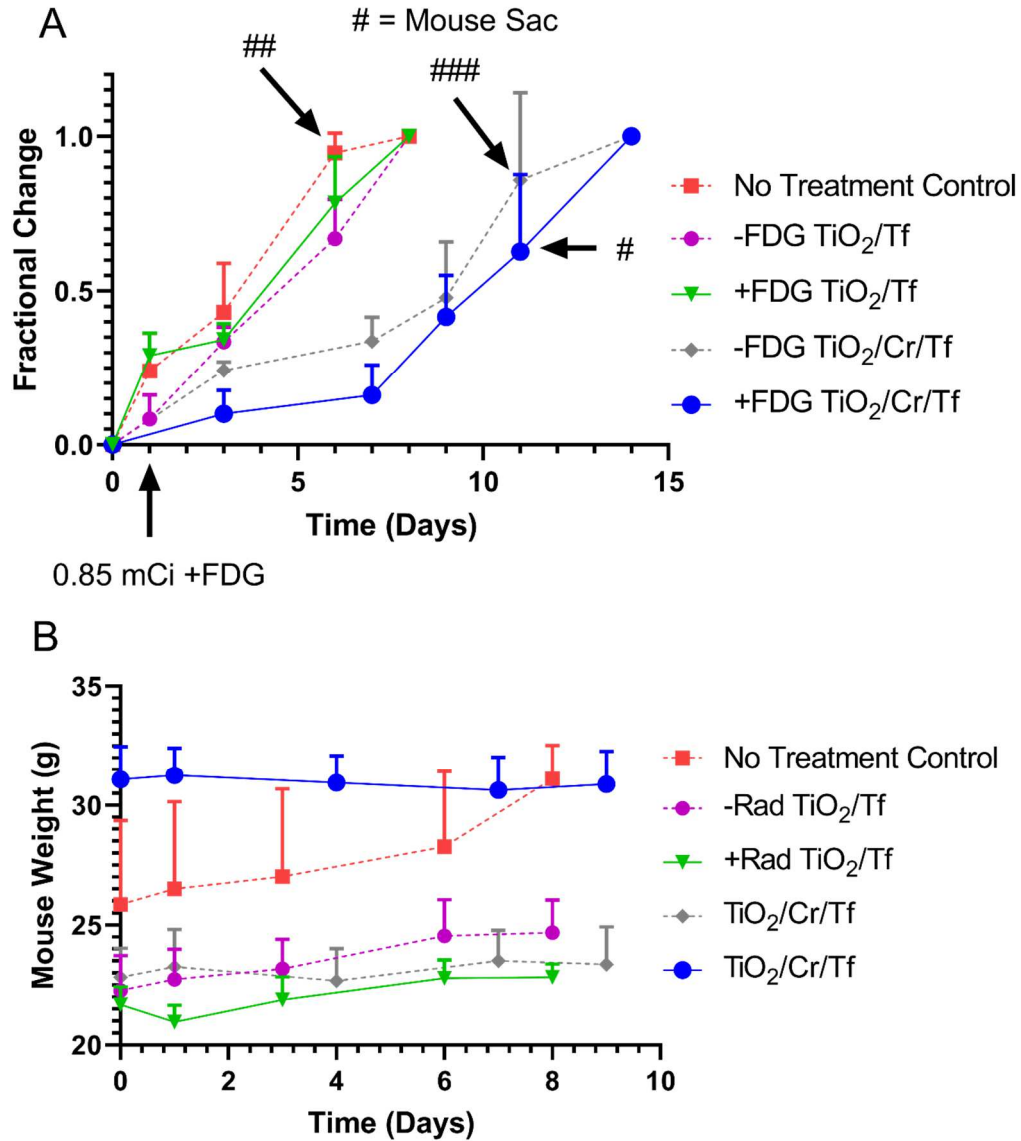
Figure 0-3: Tf-TiO$_2$/Cr PRaST of LLC flank tumors.
A) *In vivo* PRaST through one-time intratumoral injection of NAG and FDG in LLC-tumor-bearing FOX Chase mice. Values are mean ± SEM. (n=4 mice per group). # = Sacrificed mice due to tumor burden. B) Mouse body weight.

4.5 Conclusion

Overall, Tf-TiO$_2$/Cr shows increased toxicity against cells relative to an equivalent concentration of free Cr(VI) indicating a targeting effect which increases the therapeutic window. This increased toxicity is supplemented by timed release within the uptake time of Tf-TiO$_2$ in tumor tissue. Combined this indicates possible compatibility with systemic therapy with a mechanism that mimics current NP formulations of cisplatin. Finally, initial mouse data indicates an enhanced tumor suppression both from Tf-TiO$_2$/Cr alone and with ^{18}FDG. Combined these factors make TiO$_2$/Cr a prime candidate for enhanced PRaST therapy.

Chapter 5: Perfluorinated Polymer for Oxygen Delivery and Photosensitization

5.1 Chapter Summary

Existing TiO_2 PDT loses ~ 30 % of ROS generation ability when at 3 % atmospheric oxygen, this level of hypoxia being common in solid tumors.[4] Existing PDT has partially overcome this by directly delivering oxygen to tumors through hyperoxia gas therapy, ultrasound stimulated microbubbles, or through perfluorinated nanosystems. We sought to combine direct oxygen delivery with TiO_2 PRaST through a polymeric perfluorocarbon system. Utilizing a radical addition fragmentation chain transfer (RAFT) polymer we stabilized a perfluorooctyl bromide (PFOB) nanoemulsion. This structure allows for facile modification through hydroxyethyl methacrylate groups by click or carbodiimide chemistry conjugation, radionuclide chelation and fluorescent imaging. Investigation of the ideal perfluorocarbon modification ratio on 9000 MW mPEGMA-HEMA backbone showed 40 % weight (wt) modification generated stable particles with a 20 nm diameter and 0.3 PDI. With this as a guide, two formulations of 2:1 ratio PerfMA:mPEGMA polymers were generated, the first a single pot statistical copolymer $PerfMA_{54}$-co-$PEGMA_{45}$ and a two-step blocking of $mPEGMA_{31}$-b-$PerfMA_{69}$. The blocking produced a more stable PFC nanoemulsion with a final extruded size of 155.9 nm (PDI 0.253) construct with 20% by wt PFOB filler. Additionally, the particle was able to incorporate cypate at 26 μM for *in vivo* tracking. A 5 mg/mL solution of the emulsion delivered an additional 3%

oxygen per mL, relative to water. *In vivo* MSOT imaging showed a 20 % increase in hemoglobin O_2 saturation 4 hrs post-injection. No change was seen in cypate regions of a PFOB free sham.

5.2 Introduction

Polymer Nanoparticles

Polymeric NP's flexibility has made them a staple across several scientific fields.[145,146] The most notable advantage being the ability to generate biodegradable structures that increase biocompatibility relative to "hard" systems like gold or semiconducting NPs. Additionally, facile modification through carbodiimide and click reactions allow multi-targeting and drug carrying capacity.[147] From drug delivery to imaging to extra-cellular media mimicry, organic polymers can play a variety of roles and have a significant story in the 3rd generation of photosensitizers.[148] For our work, we focus on PFC modification.

Perfluorocarbon Oxygen Carrying

As stated previously, PDT efficiency drops in low cellular oxygen environments, most notably that of hypoxic tumor cores. To overcome this deficiency many different systems have been applied, from hyperoxia gas therapy to sequestered oxygen particles, each showing their own disadvantages.[149–151] PFCs are one such system found to dissolve large amounts of oxygen due to their self-avidity and high electro-negativity.[152] Due to these factors they have been heavily investigated as a blood substitute, eventually generating FDA approved Fluosol and Oxygent as synthetic emergency blood fillers.[153] PFC particles have shown the ability to improve tumor oxygenation due to their increased oxygen solubility.[154] Additionally, oxygen

normalization decreases metastasis rate from tumor tissues.[155–157] These properties make PFC

ideal for increasing PS efficiency in depleted oxygen environments.[158]
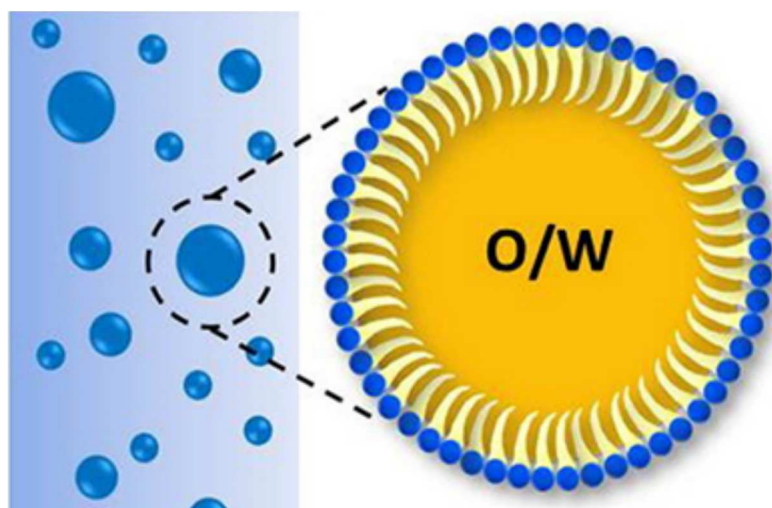
Figure 0-1: Depiction of an oil-in-water nanoemulsion.

RAFT Chemistry

To generate stable nanoscale formulations, the components themselves must be well

controlled and characterized. RAFT polymerization offers fine control of chain length and

composition through living radical polymerization.[159–161] The chemistry is based on a radical

stabilizing, chain transfer agent (CTA) that kinetically controls growing polymer backbones,

providing even chain growth and leaving a reactivatable end group for additional

polymerization.[145] In the case of PFCs, RAFT is one of the most economical methods for

generating well-defined polymers.[162]

5.3 Experimental Methods

Materials

Our lab synthesized (E)-3-perfluoroalkoxy acrylic acid (XPAA). All Materials were purchased from Sigma-Aldrich unless otherwise stated. Abbreviations: Perfluorooctyl methacrylate (PerfMA). Methyl-(polyethylene glycol) Methacrylate (MW 950) (mPEGMA). Hydroxyethyl Metacrylate (HEMA). Diisopropyl carbodiimide (DIC), 4-Dimethylaminopyridine (DMAP). 4,4'-azobis(4-cyanovaleric acid) (ABCVA). 4-cyano-4-(phenylcarbonothioylthio) pentanoic acid (CTP). Perfluoroocytl bromide (PFOB). Perfluoro-15-crown-5 ether (CE).
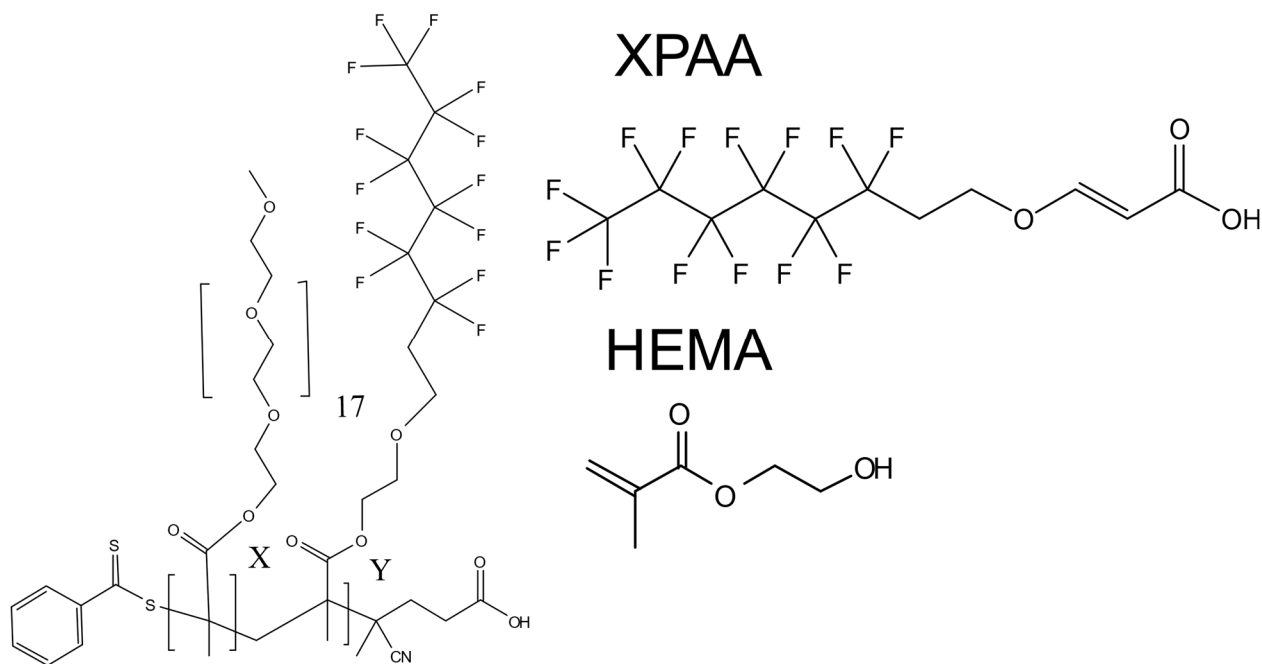
Figure 0-2: Molecular components of polymer structures.
Left) The final polymer structure for mPEGMA-b-PerfMA. Right) HEMA monomer for DIC chemistry linkages and XPAA, the linked PFC for initial wt % testing.

RAFT Synthesis of mPEGMA₅-co-HEMA₂₈

Initial backbone synthesis targeted a 30% mPEGMA, 70% HEMA. Synthesis was carried out in a 20 mL round bottom flask following work done by Lane et al.[160] Briefly, polymerization was carried out assuming 80% monomer conversion with a 4:1 CTA/initiator ratio targeting a total degree of polymerization (DP) of 20. 1.8 g mPEGMA, 0.059 g CTP and 1.1 g HEMA were dissolved in a 15 mL flask in 11 mL 1,4-dioxane (Fischer Scientific). Then 0.019 g ABCVA was added and dissolved. Oxygen was removed through freeze-vacuum-thaw cycling 3x followed by 10 min of argon purge. Polymerization was carried out on a temperature-controlled oil bath at 85 □C for 24 hrs. The reaction was then placed on ice and oxygen quenched before being purified against chilled DEE via precipitation/centrifugation. The minimum volume of acetone was used to resuspend the polymer between each wash (~1 mL).

The final composition of the polymer was confirmed in d-DMSO by proton NMR. Monomer conversion was determined by vinyl signal (2H – 6-5.8 ppm, 2H – 5.5-5.3 ppm, depending upon monomer). HEMA vs. mPEGMA composition was examined through ratio of PEG chain (86H – 3.45 ppm) and backbone peaks (5H – 0.85-1.4 ppm). Living chain end preservation and total monomer ratio was defined from the CTP phenolic protons (1H - 7.65 ppm, 2H - 7.485, 7.9 ppm). CTA preservation was confirmed via UV-vis at 520 nm.

Grafting XPAA to mPEGMA-co-HEMA via DIC Chemistry

The mPEGMA₅-co-HEMA₂₈ was modified by DIC chemistry to XPAA. XPAA was weighed and dissolved in DCM assuming 100% reaction conversion. ~1 mg DMAP as a catalyst before a stock solution of 60 mg/mL mPEGMA₅-co-HEMA₂₈ was added and vortexed to

homogeneity. The solutions were then well mixed for 5 min before the addition of DIC at a 1:1 molar ratio to XPAA. This was then placed on a shaker and incubated overnight.

Purification was done with ice cold DEE as above. ^{1}H NMR of purified stocks confirmed XPAA modification fraction through the alkane protons (2H - 7.54, 2H - 5.25) against the CTP chain ends (1H - 7.79, 1H - 8.28) (Figure 5-4).

DLS was run in PBS from ethanol stocks targeting 1 mg/mL polymer in solution and <5 % ethanol. Critical micellular concentration (CMC) was confirmed with rhodamine 6G sequestration in PBS, comparing both absorbance and fluorescence fits.

PERFMA-co/b-mPEGMA Polymerization

2:1 PerfMA/mPEGMA ratio chains were generated in two separate structures. PerfMA-co-mPEGMA was performed in single pot, targeting a DP of 100, 80 % monomer conversion, CTA/I ratio of 4, and 20 wt % monomer in dioxane. PerfMA-b-mPEGMA was generated through a 2-step process, first synthesizing a mPEGMA macro-CTA with the same solution parameters above but targeting DP of 30. NMR was used to verify chain length and then PerfMA was used to extend the chain, targeting a DP of 60. Final polymer chain lengths and monomer ratios were verified by NMR. Structural imaging was done via TEM using 3% uranyl acetate to stain the polymer.

Nanoemulsion Stability

PFOB was encapsulated by the polymer through mixing with ethanol mPEGMA-b-PerfMA stock at 50 mg/mL. The solution was well mixed before being injected into an aqueous solution and probe sonicated at 4 W for 5 min on ice. The resulting particles were sized by DLS.

Further narrowing of particle distribution was done via different sizes of NanoSizer MINI extruder (T&T Scientific). Sonicated particles were placed in a 2 mL syringe and passed 5x through the extrusion membrane at r.t. via hand pressure.

Cypate, a NIR fluorescent dye (760 ex/830 em), was loaded into the emulsion for fluorescent tracking at 50 µg/mL and run through the emulsion stabilization process above. Incorporation was determined via UV-vis. Stability of the cypate incorporation was determined by dialysis against PBS using a 3,500 MW cutoff SnakeSkin Membrane (Fischer Scientific).

Oxygen Delivery

All oxygen delivery tests were run against 20 wt % PFOB mPEGMA-b-PerfMA nanoemulsions. Oxygen concentration was determined with an Ocean Optics (now Ocean Insight) Neofox oxygen sensor fitted with a FOSPOR probe. Calibration was run against pure argon, pure oxygen, and atmospheric oxygen. Oxygen delivery into solution was tracked in a sealed 10 mL round bottom flask that had been purged with argon via bubbling for 10 min pre-injection of either the nanoemulsion or water. The nanoemulsion or water had oxygen loaded by bubbling for >1 hrs with pure oxygen. Injections were of 1 mL added rapidly and the oxygen tension within the round bottom tracked. After equilibration of oxygen in solution, the nanoemulsion was further destabilized via bath sonication and the O_2 level tracked.

MSOT Oxygenation Imaging

HT1080 xenograft subcutaneous tumors were implanted into the flank of Athymic NCr nude mice. Tumors were implanted with 10k cells per injection and were grown to 2 cm before the start of experimentation. Imaging was done via iTheraMedical inVision MSOT imager over a full spectral sweep from 680-980 nm. Imaging was done pre-injection, and 2, 4, 24 hrs post-

injection. Injections were 200 μL i.v. of either PerfMA-b-mPEGMA cypate with or without 20 % PFOB.

Analysis was done on inVision's proprietary software when images were extracted from slices within known tumor boundaries. Oxy/Deoxy-Hemoglobin ratios were determined against known cypate signal areas within MATLAB on a pixel by pixel basis and converted into oxygen saturation values. Selections also excluded any regions that had no signal on any of the channels. All analyses were then plotted by histogram for timepoint comparison.

5.4 Results

mPEGMA-co-HEMA Characterization and Functionalization

Post purification the polymer composition was confirmed via NMR (Figure 5-4). The resulting monomer per chain of 5 units mPEGMA and 28 units HEMA provided a large range of possible modification with XPAA. Modification was carried out from 0-60 wt%, confirmed via NMR. DLS measurements of the different XPAA modifications showed the highest stability at a 2:1 PFC to PEG mass ratio with a micellular size of 22.9 nm and PDI of 0.2 by DLS. As this size of mPEGMA(950)$_5$-co-HEMA$_{19}$-g-XPAA$_9$ was ideal for future study, its micellular structure was confirmed via CMC using rhodamine 6G. Both absorbance (CMC$_A$ = 0.017 ± 0.004 mg/mL) and fluorescence (CMC$_F$ = 0.012 ± 0.003 mg/mL) averaged to a CMC of 0.0144 mg/mL.
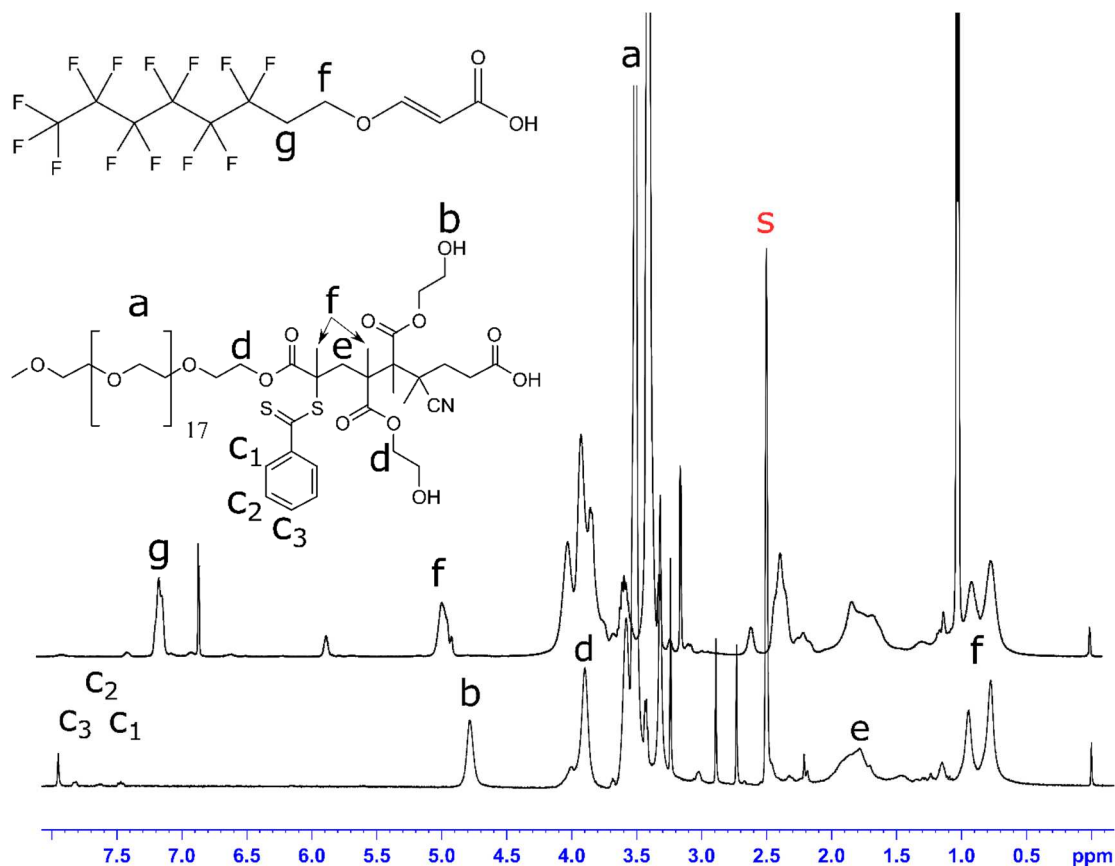
Figure 0-3: Characterization of mPEGMA-HEMA and mPEGMA-co-HEMA-g-XPAA.
Bottom) mPEGMA$_5$-co-HEMA$_{28}$ NMR spectra shows the characteristic peaks from CTP's aromatic ring c$_{1-3}$ and main PEG peak, a, for quantification. The top) spectra is mPEGMA$_5$-co-HEMA$_{19}$-g-XPAA$_9$, quantified against the high resonance alkane protons g and f.
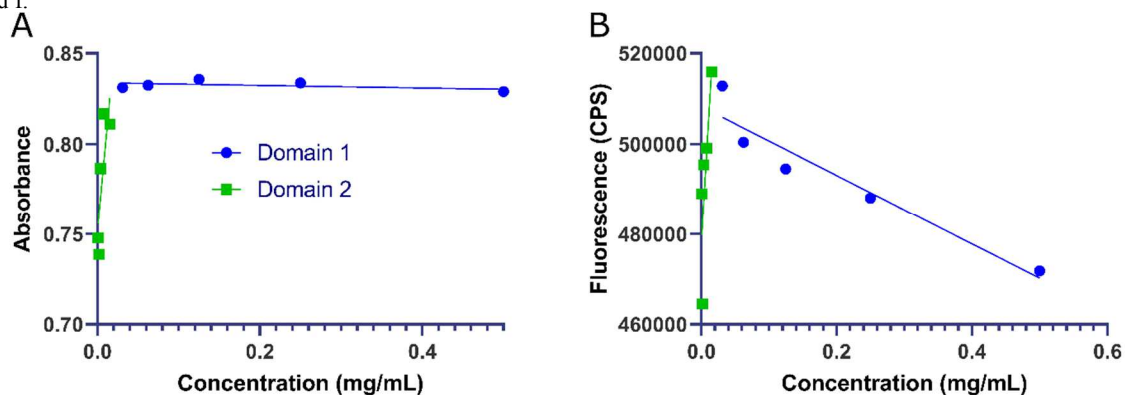
Figure 0-4: Rhodamine 6G CMC determination of mPEGMA$_5$-co-HEMA$_{19}$-g-XPAA$_9$.
Determination done against both A) absorbance and B) fluorescence. Linear fits imaged as straight lines and intersection taken as CMC concentration.

66

PerfMA-mPEGMA Synthesis and Characterization

With a ratio of 2:1 PFC to PEG for micelle generation selected, synthesis switched to a PerfMA monomer, reducing reaction complexity. First, a statistical copolymer was investigated as it provided a single pot reaction. Additionally, the rate of homo-addition for PerfMA should be far higher the hetero-addition to mPEGMA, generating a gradient copolymer with distinct domains. To increase the domain separation, a DP of 100 was chosen and NMR analysis confirmed a final polymer composition of $mPEGMA_{46}$-co-$PerfMA_{54}$. However, PFOB encapsulation studies showed unstable emulsion, requiring investigation of the nanostructure by TEM. Uranyl acetate staining reveled phase separated aggregates without a clear PFC domain (Figure 5-6A). To increase the domain separation, a second polymer was generated in a block structure, which, after two pot synthesis, yielded $mPEGMA_{31}$-b-$PerfMA_{69}$ by NMR. This was investigated by TEM which showed well defined micellular structures (Figure 5-6B) and gave stable PFOB emulsions.
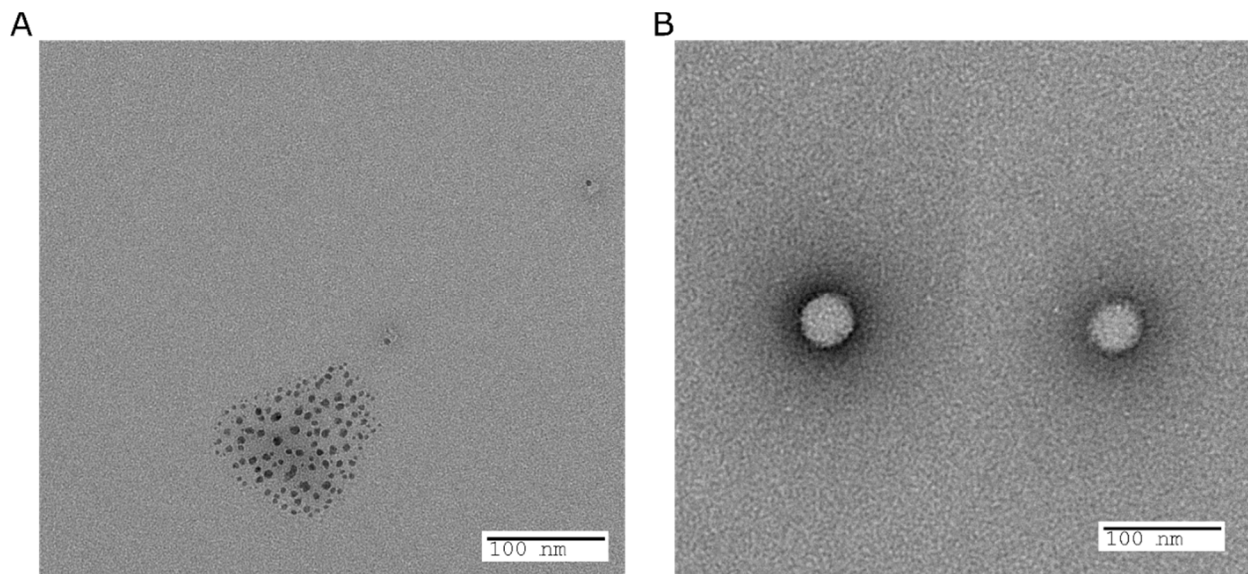
Figure 0-5: Uranyl acetate stained A) mPEGMA-co-PerfMA and B) mPEGMA-b-PerfMA.

As several fillers can be used for perfluorinated emulsions, two of the current gold standards were selected for testing, CE and PFOB. CE can be easily imaged by ^{19}F MRI but has a slightly lower oxygen carrying capacity relative to PFOB origin. Both were incorporated into the mPEGMA$_{31}$-b-PerfMA$_{69}$ at 20% by volume and analyzed by DLS. The CE showed limited stability with a 10% upward trend in particle size over 30 min, averaging 120.6 ± 32.90 nm and a PDI of 0.435 ± 0.07 (Figure 5-7B). The PFOB showed stability at 68.12 ± 0.35 nm and a PDI of 0.142 ± 0.01, with a slight decrease in size of 5% over 30 min.
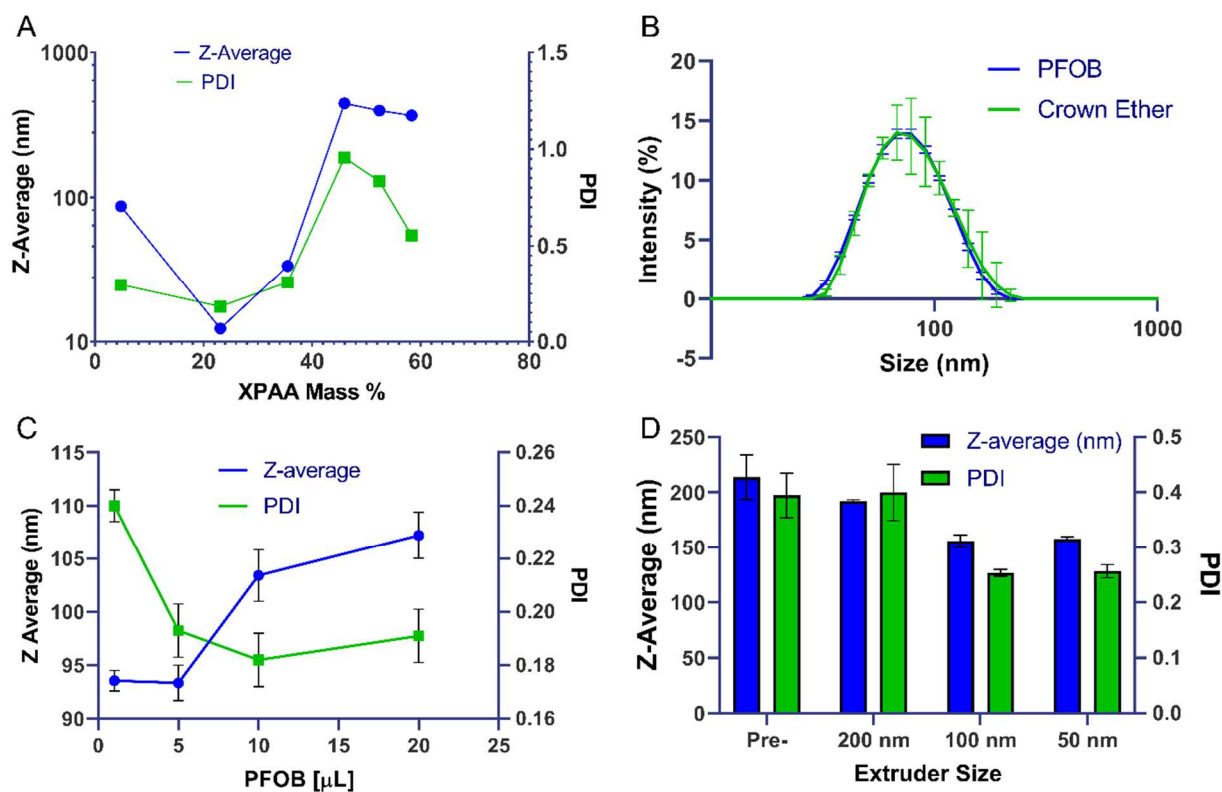
Figure 0-6: Perfluorocarbon nanoemulsion size optimization.
A) mPEGMA$_5$-co-HEMA$_{28}$-g-XPAA$_x$ DLS measurements against the mass fraction of PFC. B) Histogram fit of intensity vs size by DLS for mPEGMA$_{31}$-b-PerfMA$_{69}$ emulsions of either PFOB or CE. C) mPEGMA$_{31}$-b-PerfMA$_{69}$ emulsions of different quantities of PFOB. D) Extruded sizes of mPEGMA$_{31}$-b-PerfMA$_{69}$ 20 % PFOB emulsions using different extruder filters.

With evidence of stable emulsions, the final size was refined via extrusion. Three separate filter sizes were tested, 200, 100 and 50 nm (Figure 5-7D). 50 nm extruder showed low particle yield, slow purification, and final particle sizes near 100 nm. The 200 nm extruder

showed no benefits to PDI. 100 nm showed improvement of PDI for 0.4 to 0.2 while reducing the average particle size to 155.9 nm.

Cypate Incorporation for *in vivo* Tracking

To track the nanoemulsions *in vivo* the NIR dye cypate was added at 50 µg/mL. UV-vis post purification revealed a final cypate concentration of 5.5 µg/mL in the emulsion and 4.79 µg/mL in the polymer micelle alone at 1 mg/mL mPEGMA-b-PerfMA. The emulsions encapsulation was then tested for stability against PBS dialysis. The initial results show a burst release of cypate which stabilized at 76 % initial value, representing a final stable formulation of 4.18 µg/mL cypate in a 5 mg/mL polymer weight emulsion.

MSOT Oxygen and Particle Tracking

Oxygen delivery was confirmed in deoxygenated water using a ruthenium, lifetime-based oxygen probe. Comparing the O_2 change of a 1 mL injection of oxygenated 5 mg/mL polymer 20 wt % PFOB emulsion vs oxygenated water the emulsion was able to increase O_2 levels by an additional 3%, representing a 1.21 g oxygen/mol solubility increase over water (Figure 5-8A).
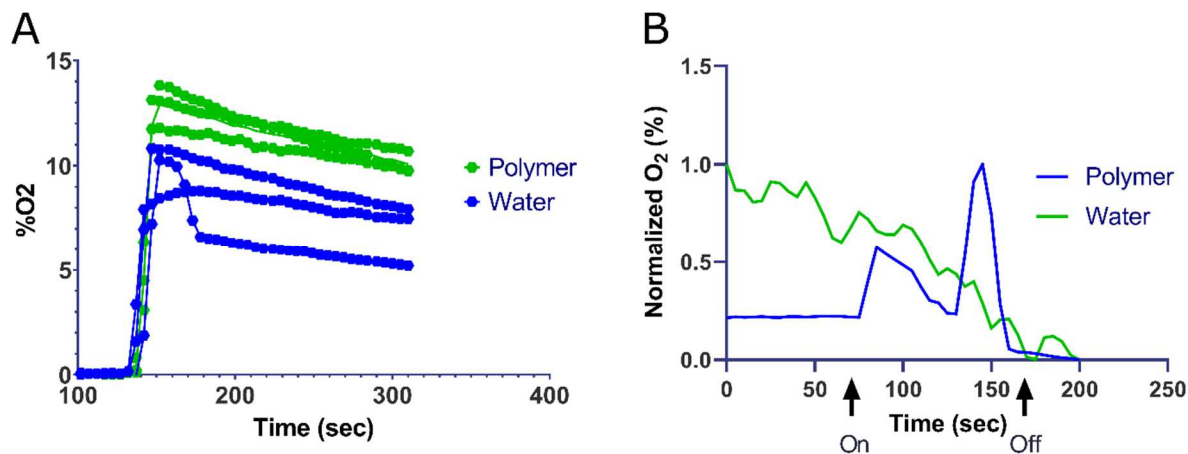
Figure 0-7: Dissolved oxygen delivery by PFOB nanoemulsion.
 A) Oxygen saturation change by injecting oxygenated water or 20 wt% PFOB nanoemulsion at 5 mg/mL polymer. B) Sonication of water alone or nanoemulsion. Destabilization by sonication of the emulsion shows release of sequestered oxygen.

With oxygen carrying capacity confirmed, the nanoemulsion was run in a pilot study against HT-1080 xenograft tumors. These were grown to 2 cm to generate hypoxic regions and provide sufficient volume for MSOT imaging. Oxygenated mPEGMA-b-PerfMA/cypate with and without PFOB filler were injected. Image slices within the tumor boundaries were selected and the areas of hemoglobin signal were colocalized with cypate. Figure 5-9A shows the delineation of particle containing regions. The oxy/deoxy hemoglobin signal was extracted, and oxygen saturation calculated pixel-by-pixel. The oxygen saturation increased from 40 to 57 % in the first hour (Figure 5-9B). This increased further at 4 hrs to 62 % before returning to 43% at 24 hr. This is compared to no change seen over the 24-hour period (Figure 5-9D) using only oxygenated polymer micelles as control.
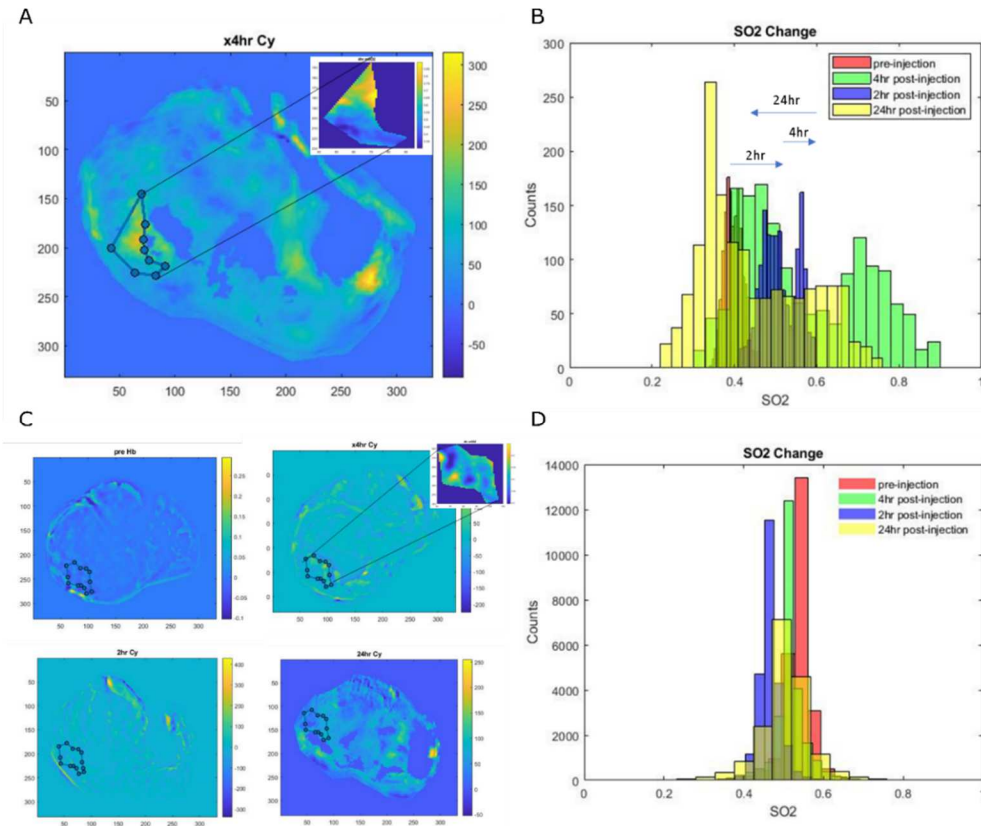
Figure 0-8: MSOT imaging of cypate and hemoglobin.
Mice injected with oxygenated A) nanoemulsion at 4 hour and C) unloaded polymer micelle at each time point loaded with cypate. The selected area was aligned across each time point (pre, 2, 4, 24 hr) and analyzed for oxygen saturation. The histograms for the B) nanoemulsion and D) micelle were shown with the saturation mean shifts indicated with arrows.

5.5 Conclusion

Here we investigated the ideal parameters for generating stable PFC emulsions for oxygen delivery *in vivo*. Grafting studies showed a 2:1 ratio of PFC to PEG generates a stable nanoemulsion with a PFOB filler. While the PFC polymer micelle did not increase oxygen delivery, forming a PFOB emulsion increased the oxygen solubility 30 % over water. The nanoemulsion's ability to deliver dissolved oxygen to tumor tissue was then confirmed by MSOT imaging. Combining this system with TiO_2 via co-delivery and/or direct linking of the nanoemulsion via chelating groups should provide direct enhancement for PRaST.

Chapter 6: Conclusions on Nanoscale PRaST Enhancement

PRaST has proven effective in reducing tumor burden and stimulating immune response. Our work within this dissertation expands the future impact of PRaST within the clinical domain. Refinement of TiO_2 physical parameters and their effects on ROS generation and biodistribution show an interplay at sub-25 nm cTd. Additionally, the apparent increase in hydroxyl yield within quantum confined TiO_2 may be a method for further reducing oxygen dependence of PRaST.

Investigation of TiO_2/Cr resulted in effective metallo-therapy, both alone and when combined with PRaST, able to increase ROS generation through chromate and provide *in vivo* tumor suppression. The restriction of hole injection to chromate alone does present future challenges, requiring an increase in chromate's retention at biological pH or another high energy donor. Initial investigation of a shell trap system shows promise and with calcination to reduce porosity and increase crystallinity can achieve permanent ROS enhancement. TiO_2/Cr(VI)'s ability to increase toxicity of Cr in culture and *in vivo* shows promise as a standalone metallo-therapeutic. The surface retention of Cr(VI) provides targeted delivery and clearance of Cr(III) will be investigated to confirm limited off target effects.

Finally, the polymer-stabilized nanoemulsion provided effective oxygen delivery into tumors. Refinement of ideal mass ratios of PFC generated stable emulsions near the Tf-TiO_2 NAG size, ideal for co-localization. This system also showed encapsulate and *in vivo* tracking with cypate using novel MSOT imaging, while also increasing O_2 saturation within the tumor

region. Direct combination with PRaST remains to be investigated but will indicate reduced tumor burden for the combination therapy.

In conclusion, this dissertation focuses on maximizing the therapeutic benefit of PRaST through the generation of nanoscale systems able to overcome inherent tumor resistance mechanisms. The combination and enhancements these approaches provide have shown decreased tumor burden through ROS and metallo-therapy, benefiting both from controlled dosage and immune recruitment. Future investigations will focus on direct investigation of *in vivo* efficacy of each approach and combinations thereof. Overall, the systems represented here enhance existing TiO_2 PRaST and advance the search for total cancer remission.

References:

1.   World Health Organization. WHO methods and data sources for glogal burden of disease estimates 2000-2016. 1–46 (2018).

2.   Analytics, C. Web of Science [v5.35].

3.   Brown, J. A. & Schober, M. Cellular quiescence: How TGFβ protects cancer cells from chemotherapy. *Mol. Cell. Oncol.* **5**, (2018).

4.   Vaupel, P. Tumor microenvironmental physiology and its implications for radiation oncology. *Semin. Radiat. Oncol.* **14**, 198–206 (2004).

5.   Agostinis, P. *et al.* Photodynamic Therapy of Cancer: An Update. *Ca A Cancer J. Clin.* **61**, 250–281 (2011).

6.   Bertrand, N., Wu, J., Xu, X., Kamaly, N. & Farokhzad, O. C. Cancer nanotechnology: The impact of passive and active targeting in the era of modern cancer biology. *Advanced Drug Delivery Reviews* **66**, 2–25 (2014).

7.   Valko, M., Izakovic, M., Mazur, M., Rhodes, C. J. C. J. & Telser, J. Role of oxygen radicals in DNA damage and cancer incidence. *Mol. Cell. Biochem.* **266**, 37–56 (2004).

8.   Sarsour, E. H., Kumar, M. G., Chaudhuri, L., Kalen, A. L. & Goswami, P. C. Redox control of the cell cycle in health and disease. *Antioxidants Redox Signal.* **11**, 2985–3011 (2009).

9.   Filomeni, G. & Ciriolo, M. R. Redox Control of Apoptosis: An Update. *Antioxidants Redox Signal.* **8**, (2006).

10.   Montero, A. J. & Jassem, J. Cellular redox pathways as a therapeutic target in the treatment of cancer. *Drugs* **71**, 1385–1396 (2011).

11.   Simon, H.-U., Haj-Yehia, A. & Levi-Schaffer, F. Role of reactive oxygen species (ROS) in apoptosis induction. *Apoptosis* **5**, 415–418 (2000).

12.   Li, Y., Zhu, H. & Trush, M. A. Detection of mitochondria-derived reactive oxygen species production by the chemilumigenic probes lucigenin and luminol. *Biochim. Biophys. Acta - Gen. Subj.* **1428**, 1–12 (1999).

13.   Foyer, C. H. & Noctor, G. Ascorbate and glutathione: The heart of the redox hub. *Plant*

Physiol. **155**, 2–18 (2011).

14.   Moran, L., Gutteridge, J. & Quinlan, G. Thiols in Cellular Redox Signalling and Control. *Curr. Med. Chem.* **8**, 763–772 (2012).

15.   Schaap, A. P., Thayer, A. L., Faler, G. R., Goda, K. & Kimura, T. Singlet Molecular Oxygen and Superoxide Dismutase. *J. Am. Chem. Soc.* **96**, 4025–4026 (1974).

16.   Weser, U., Paschen, W. & Younes, M. Singlet oxygen and superoxide dismutase (cuprein). *Biochem. Biophys. Res. Commun.* **66**, 769–777 (1975).

17.   Bhagat, J., Ingole, B. S. & Singh, N. Glutathione s-transferase, catalase, superoxide dismutase, glutathione peroxidase, and lipid peroxidation as biomarkers of oxidative stress in snails: A review. *Invertebr. Surviv. J.* **13**, 336–349 (2016).

18.   Chen, Y., Liu, K., Shi, Y. & Shao, C. The tango of ROS and p53 in tissue stem cells. *Cell Death Differ.* **25**, 637–639 (2018).

19.   Survila, M. *et al.* Peroxidase-generated apoplastic ROS impair cuticle integrity and contribute to DAMP-elicited defenses. *Front. Plant Sci.* **7**, 1–16 (2016).

20.   Land, W. G., Agostinis, P., Gasser, S., Garg, A. D. & Linkermann, A. Transplantation and Damage-Associated Molecular Patterns (DAMPs). *Am. J. Transplant.* **16**, 3338–3361 (2016).

21.   Frazier, V. N., Holl, E., Boczkowski, D., Sullenger, B. & Nair, S. K. Targeting DAMP-induced inflammation to prevent breast cancer metastasis and improve anti-tumor immunity. *J Immunol* **202**, (2019).

22.   Pandolfi, F., Altamura, S., Frosali, S. & Conti, P. Key Role of DAMP in Inflammation, Cancer, and Tissue Repair. *Clin. Ther.* **38**, 1017–1028 (2016).

23.   Hönigsmann, H. History of phototherapy in dermatology. *Photochem. Photobiol. Sci.* **12**, 16–21 (2013).

24.   Allison, R. R., Mota, H. C. & Sibata, C. H. Clinical PD/PDT in North America: An historical review. *Photodiagnosis and Photodynamic Therapy* **1**, 263–277 (2004).

25.   Rabb, O. On the effect of fluorescent substances on infusoria. *Z Biol.* **39**, 524–526 (1900).

26.   Tappeiner, H. Von & Jesionek, A. Therapeutic trials with fluorescent substances. *Munch Med Wochenschr* (1903).

27.   Jesionek, A. & Von Tappeiner, H. On the treatment of skin cancers with fluorescent

substances. *Arch Klin Med* **82**, 223–7 (1905).

28.   Dougherty, T. J. Hematoporphyrin as a Photosensitizer of Tumors. *Photochem. Photobiol.* **38**, 377–379 (1983).

29.   Dougherty, T. J., Gomer, C. & Henderson, B. . Photodynamic Therapy. *J. Natl. Cancer Inst.* **91**, 889–905 (1998).

30.   Dougherty, T. J. & Marcus, S. L. Photodynamic therapy. *Eur. J. Cancer* **28**, 1734–1742 (1992).

31.   Photofrin (Porfimer Sodium). *Drug Approval Package* Available at: https://www.accessdata.fda.gov/drugsatfda_docs/nda/2003/020415s012_021525_Photofri nTOC.cfm. (Accessed: 4th September 2020)

32.   Verma, S. & Dwivedbi, U. Heterogeneous Fenton behavior of nano nickel zinc ferrite catalysts in the degradation of 4-chlorophenol from water under neutral conditions. *J. Water Process Eng.* **91**, 107–125 (2014).

33.   Chen, H. *et al.* Combined chemo- and photo-thermal therapy delivered by multifunctional theranostic gold nanorod-loaded microcapsules. *Nanoscale* **7**, 8884–8897 (2015).

34.   Troutman, T. S., Leung, S. J. & Romanowski, M. Light-induced content release from plasmon-resonant liposomes. *Adv. Mater.* **21**, 2334–2338 (2009).

35.   Ohulchanskyy, T. Y. *et al.* Organically modified silica nanoparticles with covalently incorporated photosensitizer for photodynamic therapy of cancer. *Nano Lett.* **7**, 2835–2842 (2007).

36.   Georgakoudi, I., Nichols, M. G. & Foster, T. H. The mechanism of Photofrin photobleaching and its consequences for photodynamic dosimetry. *Photochem. Photobiol.* **65**, 135–144 (1997).

37.   Dellinger, M. Apoptosis or necrosis following photofrin® photosensitization: Influence of the incubation protocol. *Photochem. Photobiol.* **64**, 182–187 (1996).

38.   Dougherty, T. J., Cooper, M. T. & Mang, T. S. Cutaneous phototoxic occurrences in patients receiving Photofrin®. *Lasers Surg. Med.* **10**, 485–488 (1990).

39.   Diamond, I. *et al.* Photodynamic Therapy of Malignant Tumours. *Lancet* **300**, 1175–1177 (1972).

40.   Bellnier, D., Ho, Y.-K., Pandey, R., Missert, J. & Dougherty, T. Distribuion and

Elimination of Photofrin II in Mice. *Photochem. Photobiol.* **50**, 221–228 (1989).

41.   Casas, A., Fukuda, H., Di Venosa, G. & Batlle, A. Photosensitization and mechanism of cytotoxicity induced by the use of ALA derivatives in photodynamic therapy. *Br. J. Cancer* **85**, 279–284 (2001).

42.   Kennedy, J. C., Marcus, S. L. & Pottier, R. H. Photodynamic therapy (PDT) and photodiagnosis (PD) using endogenous photosensitization induced by 5-aminolevulinic acid (ALA): Mechanisms and clinical results. *J. Clin. Laser Med. Surg.* **14**, 289–304 (1996).

43.   Kennedy, J. C. & Pottier, R. H. New trends in photobiology. Endogenous protoporphyrin IX, a clinically useful photosensitizer for photodynamic therapy. *J. Photochem. Photobiol. B Biol.* **14**, 275–292 (1992).

44.   Henderson, T. A. & Morries, L. D. Near-infrared photonic energy penetration: Can infrared phototherapy effectively reach the human brain? *Neuropsychiatr. Dis. Treat.* **11**, 2191–2208 (2015).

45.   He, X. *et al.* Stereotactic Photodynamic Therapy Using a Two-Photon AIE Photosensitizer. *Small* **15**, 1–8 (2019).

46.   Idris, N. M. *et al.* In vivo photodynamic therapy using upconversion nanoparticles as remote-controlled nanotransducers. *Nat. Med.* **18**, 1580–1585 (2012).

47.   Heer, S., Kömpe, K., Güdel, H. U. & Haase, M. Highly efficient multicolour upconversion emission in transparent colloids of lanthanide-doped NaYF4 nanocrystals. *Adv. Mater.* **16**, 2102–2105 (2004).

48.   Maleki Dizaj, S. *et al.* An update on calcium carbonate nanoparticles as cancer drug/gene delivery system. *Expert Opin. Drug Deliv.* **16**, 331–345 (2019).

49.   Beguin, E. *et al.* Direct Evidence of Multibubble Sonoluminescence Using Therapeutic Ultrasound and Microbubbles. *ACS Appl. Mater. Interfaces* **11**, 19913–19919 (2019).

50.   Castano, A. P., Mroz, P. & Hamblin, M. R. Photodynamic therapy and anti-tumour immunity. *Nat. Rev. Cancer* **6**, 535–545 (2006).

51.   Kotagiri, N., Sudlow, G. P., Akers, W. J. & Achilefu, S. Breaking the depth dependency of phototherapy with Cerenkov radiation and low-radiance-responsive nanophotosensitizers. *Nat Nanotechnol* **10**, 370–379 (2015).

52. Kotagiri, N. *et al.* Radionuclides transform chemotherapeutics into phototherapeutics for precise treatment of disseminated cancer. *Nat. Commun.* **9**, 1–12 (2018).

53. Hoefnagel, C. A. Radionuclide cancer therapy. *Ann. Nucl. Med.* **12**, 61–70 (1998).

54. Wild, D. *et al.* Alpha- versus beta-particle radiopeptide therapy in a human prostate cancer model (213Bi-DOTA-PESIN and 213Bi-AMBA versus 177Lu-DOTA-PESIN). *Cancer Res.* **71**, 1009–1018 (2011).

55. Isaac, A. *et al.* In situ 3D quantification of the evolution of creep cavity size, shape, and spatial orientation using synchrotron X-ray tomography. *Mater. Sci. Eng. A* **478**, 108–118 (2008).

56. Jelley, J. V. Cerenkov radiation and its applications. *Br. J. Appl. Phys.* **6**, 227 (1955).

57. Shaffer, T. M., Pratt, E. C. & Grimm, J. Utilizing the power of Cerenkov light with nanotechnology. *Nat. Nanotechnol.* **12**, 106–117 (2017).

58. Kamkaew, A. *et al.* Cerenkov Radiation Induced Photodynamic Therapy Using Chlorin e6-Loaded Hollow Mesoporous Silica Nanoparticles. *ACS Appl. Mater. Interfaces* **8**, 26630–26637 (2016).

59. Royal, T. & Hospital, C. The luminescence of irradiated transparent media and the Čerenkov effect - I. The luminescence of aqueous solutions of radioactive isotopes. *Proc. R. Soc. London. Ser. A. Math. Phys. Sci.* **216**, 90–102 (1953).

60. Duck, F. A. *Physical Properties of Tissue: A Comprehensive Reference Book.* (1990).

61. Weber, M. J. Inorganic scintillators: Today and tomorrow. *J. Lumin.* **100**, 35–45 (2002).

62. Ding, Y., Caucci, L. & Barrett, H. H. Charged-particle emission tomography. *Med. Phys.* **44**, 2478–2489 (2017).

63. Haider, A. J., Jameel, Z. N. & Al-Hussaini, I. H. M. Review on: Titanium dioxide applications. *Energy Procedia* **157**, 17–29 (2019).

64. Fujishima, A., Zhang, X. & Tryk, D. A. TiO2 photocatalysis and related surface phenomena. *Surf. Sci. Rep.* **63**, 515–582 (2008).

65. Fujishima, A. & Honda, K. Electrochemical photolysis of water at a semiconductor electrode. *Nature* **238**, 37–38 (1972).

66. Carp, O., Huisman, C. L. & Reller, A. Photoinduced reactivity of titanium dioxide. *Prog. Solid State Chem.* **32**, 33–177 (2004).

67. Barrera-Díaz, C. E., Lugo-Lugo, V. & Bilyeu, B. A review of chemical, electrochemical and biological methods for aqueous Cr(VI) reduction. *J. Hazard. Mater.* **223–224**, 1–12 (2012).

68. Fujishima, A., Ootsuki, J., Yamashita, T. & Hayakawa, S. Behavior of Tumor Cells on Photoexcited Semiconductor Surface. *Photomed. Photobiol.* **8**, 45–46 (1986).

69. Cai, R. *et al.* Induction of Cytotoxicity by Photoexcited TiO2 Particles. *Cancer Res.* **52**, 2346–2348 (1992).

70. Fujishima, A., Rao, T. N. & Tryk, D. A. Titanium dioxide photocatalysis. *J. Photochem. Photobiol. C Photochem. Rev.* **1**, 1–21 (2000).

71. Xu, K., Xie, Y., Cui, X., Zhao, J. & Glusac, K. D. Diiodo bodipy-rhodamine dyads: Preparation and study of the acid-activatable competing intersystem crossing and energy transfer processes. *J. Phys. Chem. B* **119**, 4175–4187 (2015).

72. Mabjeesh, N. J. & Amir, S. Hypoxia-inducible factor (HIF) in human tumorigenesis. *Histol. Histopathol.* **22**, 559–572 (2007).

73. Wendt, S. *et al.* Oxygen vacancies on TiO_2(1 1 0) and their interaction with H_2O and O_2: A combined high-resolution STM and DFT study. *Surf. Sci.* **598**, 226–245 (2005).

74. Turchi, C. & Ollis, D. Photocatalytic degradation of organic water contaminants: Mechanisms involving hydroxyl radical attack. *J. Catal.* **122**, 178–192 (1990).

75. Zhang, Q., Chen, R., San, H., Liu, G. & Wang, K. Betavoltaic effect in titanium dioxide nanotube arrays under build-in potential difference. *J. Power Sources* **282**, 529–533 (2015).

76. Axelsson, J., Davis, S. C., Gladstone, D. J. & Pogue, B. W. Cerenkov emission induced by external beam radiation stimulates molecular fluorescence. *Med. Phys.* **38**, 4127–4132 (2011).

77. Ouyang, Z., Liu, B., Yasmin-Karim, S., Sajo, E. & Ngwa, W. Nanoparticle-aided external beam radiotherapy leveraging the Cerenkov effect. *Phys. Med.* **32**, 944–947 (2016).

78. Gill, R. K., Mitchell, G. S. & Cherry, S. R. Computed Cerenkov luminescence yields for radionuclides used in biology and medicine. *Phys. Med. Biol.* **60**, 4263–4280 (2015).

79. Baldini, E. *et al.* Strongly bound excitons in anatase TiO2 single crystals and nanoparticles. *Nat. Commun.* **8**, (2017).

80. Diebold, U. The surface science of titanium dioxide. *Surf. Sci. Rep.* **48**, 53–229 (2003).

81. Shultz, A. N. *et al.* Comparative second harmonic generation and X-ray photoelectron spectroscopy studies of the UV creation and O_2 healing of Ti^{3+} defects on (110) rutile TiO_2 surfaces. *Surf. Sci.* **339**, 114–124 (1995).

82. Yamamoto, T. & Ohno, T. A hybrid density functional study on the electron and hole trap states in anatase titanium dioxide. *Phys. Chem. Chem. Phys.* **14**, 589–598 (2012).

83. Sclafani, A. & Herrmann, J. M. Comparison of the photoelectronic and photocatalytic activities of various anatase and rutile forms of titania in pure liquid organic phases and in aqueous solutions. *J. Phys. Chem.* **100**, 13655–13661 (1996).

84. Shen, M. *et al.* Nanoscale colocalization of fluorogenic probes reveals the role of oxygen vacancies in the photocatalytic activity of tungsten oxide nanowires. *ACS Catal.* **10**, 2088–2099 (2020).

85. Liu, Z., Hu, B. H. & Messersmith, P. B. Acetonide protection of dopamine for the synthesis of highly pure N-docosahexaenoyldopamine. *Tetrahedron Lett.* **51**, 2403–2405 (2010).

86. Linsebigler, A. L. *et al.* Photocatalysis on TiO_2 Surfaces: Principles, Mechanisms, and Selected Results. *Chem. Rev.* **95**, 735–758 (1995).

87. Luttrell, T. *et al.* Why is anatase a better photocatalyst than rutile?--Model studies on epitaxial TiO_2 films. *Sci. Rep.* **4**, 4043 (2014).

88. Jin, C. *et al.* Cellular Toxicity of TiO_2 Nanoparticles in Anatase and Rutile Crystal Phase. *Biol. Trace Elem. Res.* **141**, 3–15 (2011).

89. Jiang, J. *et al.* Does Nanoparticle Activity Depend upon Size and Crystal Phase? *Nanotoxicology* **2**, 33–42 (2008).

90. Bickley, R. I., Gonzalez-Carreno, T., Lees, J. S., Palmisano, L. & Tilley, R. J. D. A structural investigation of titanium dioxide photocatalysts. *J. Solid State Chem.* **92**, 178–190 (1991).

91. Prasai, B., Cai, B., Underwood, M. K., Lewis, J. P. & Drabold, D. A. Properties of amorphous and crystalline titanium dioxide from first principles. *J. Mater. Sci.* **47**, 7515–7521 (2012).

92. Calza, P., Pelizzetti, E., Mogyorósi, K., Kun, R. & Dékány, I. Size dependent

photocatalytic activity of hydrothermally crystallized titania nanoparticles on poorly adsorbing phenol in absence and presence of fluoride ion. *Appl. Catal. B Environ.* **72**, 314–321 (2007).

93.   Jiang, J., Oberdörster, G. & Biswas, P. Characterization of size, surface charge, and agglomeration state of nanoparticle dispersions for toxicological studies. *J. Nanoparticle Res.* **11**, 77–89 (2009).

94.   Sun, H., Li, H., Weir, R. A. & Sadler, P. J. The first specific Ti(IV)-protein complex: Potential relevance to anticancer activity of titanocenes. *Angew. Chemie - Int. Ed.* **37**, 1577–1579 (1998).

95.   Nuevo-Ordoñez, Y., Montes-Bayón, M., Blanco González, E. & Sanz-Medel, A. Titanium preferential binding sites in human serum transferrin at physiological concentrations. *Metallomics* **3**, 1297–1303 (2011).

96.   Tinoco, A. D. & Valentine, A. M. Ti(IV) binds to human serum transferrin more tightly than does Fe(III). *J. Am. Chem. Soc.* **127**, 11218–11219 (2005).

97.   Kratz, F. *et al.* Transferrin conjugates of doxorubicin: Synthesis, characterization, cellular uptake, and in vitro efficacy. *J. Pharm. Sci.* **87**, 338–346 (1998).

98.   McDonagh, B. H. *et al.* Self-assembly and characterization of transferrin-gold nanoconstructs and their interaction with bio-interfaces. *Nanoscale* **7**, 8062–70 (2015).

99.   Danhier, F., Feron, O. & Preat, V. To exploit the tumor microenvironment: Passive and active tumor targeting of nanocarriers for anti-cancer drug delivery. *J. Control. Release* **148**, 135–146 (2010).

100.   Tybor, P. T., Dill, C. W., Bryant, J. N. & Landmann, W. A. Heat Denaturation of Blood Serum Proteins Measured in Saturated Sodium Chloride. *J. Agric. Food Chem.* **18**, 629–631 (1970).

101.   Daniels, T. R., Delgado, T., Helguera, G. & Penichet, M. L. The transferrin receptor part II: Targeted delivery of therapeutic agents into cancer cells. *Clin. Immunol.* **121**, 159–176 (2006).

102.   Jefferies, W. A. *et al.* Transferrin receptor on endothelium of brain capillaries. *Nature* **312**, 162–163 (1984).

103.   Tulpule, K., Robinson, S. R., Bishop, G. M. & Dringen, R. Uptake of ferrous iron by

cultured rat astrocytes. *J. Neurosci. Res.* **88**, 563–571 (2010).

104. Qian, Z. M. & Ke, Y. Brain iron transport. *Biol. Rev.* **94**, 1672–1684 (2019).

105. Brigger, I., Dubernet, C. & Couvreur, P. Nanoparticles in cancer therapy and diagnosis. *Adv. Drug Deliv. Rev.* **54**, 631–651 (2002).

106. Carmeliet, P. & Jain, R. K. Angiogenesis in cancer and other diseases. *Nature* **407**, 249–257 (2000).

107. Kulkarni, S. A. & Feng, S. S. Effects of particle size and surface modification on cellular uptake and biodistribution of polymeric nanoparticles for drug delivery. *Pharm. Res.* **30**, 2512–2522 (2013).

108. Thanh, N. T. K. & Green, L. a W. Functionalisation of nanoparticles for biomedical applications. *Nano Today* **5**, 213–230 (2010).

109. Zhang, Y. & Clapp, A. Overview of stabilizing ligands for biocompatible quantum dot nanocrystals. *Sensors* **11**, 11036–11055 (2011).

110. Choi, H. S. *et al.* Renal clearance of quantum dots. *Nat. Biotechnol.* **25**, 1165–1170 (2007).

111. Chae, S. Y. *et al.* Preparation of size-controlled TiO_2 nanoparticles and derivation of optically transparent photocatalytic films. *Chem. Mater.* **15**, 3326–3331 (2003).

112. Xu, B. *et al.* Electrospray Functionalization of Titanium Dioxide Nanoparticles with Transferrin for Cerenkov Radiation Induced Cancer Therapy. *ACS Appl. Bio Mater.* **2**, 1141–1147 (2019).

113. Carpenter, P. Procedures for Using the Bruker d8 Advance X-ray Diffractometer. *WUSTL* (2017). Available at: http://xraysrv.wustl.edu/web/xrd/brukerd8.html.

114. Setsukinai, K. ichi, Urano, Y., Kakinuma, K., Majima, H. J. & Nagano, T. Development of novel fluorescence probes that can reliably detect reactive oxygen species and distinguish specific species. *J. Biol. Chem.* **278**, 3170–3175 (2003).

115. Anthony, J., Bideaux, R., Bladh, K. & Nochols, M. *Handbook of Mineralogy*. (1990).

116. Ramsden, J. J. Effect of Ionic Strength on Protein Adsorption Kinetics. *J. Phys. Chem.* **98**, 5376–5381 (1994).

117. Hu, H. H. *et al.* Synthesis and stabilization of metal nanocatalysts for reduction reactions - A review. *J. Mater. Chem. A* **3**, 11157–11182 (2015).

118. Nakataa, K. & Fujishima, A. TiO$_2$ photocatalysis: Design and applications. *J. Photochem. Photobiol. C Photochem. Rev.* **13**, 169–189 (2012).

119. Reeves, J. F., Davies, S. J., Dodd, N. J. F. & Jha, A. N. Hydroxyl radicals (OH) are associated with titanium dioxide (TiO$_2$) nanoparticle-induced cytotoxicity and oxidative DNA damage in fish cells. *Mutat. Res.* **640**, 113–122 (2008).

120. Ohno, T., Sarukawa, K. & Matsumura, M. Crystal faces of rutile and anatase TiO$_2$ particles and their roles in photocatalytic reactions. *New J. Chem.* **26**, 1167–1170 (2002).

121. Orians, K. J. & Boyle, E. A. Determination of picomolar concentrations of titanium, gallium and indium in sea water by inductively coupled plasma mass spectrometry following an 8-hydroxyquinoline chelating resin preconcentration. *Anal. Chim. Acta* **282**, 63–74 (1993).

122. Gilson, R. C., Black, K. C. L., Lane, D. D. & Achilefu, S. Hybrid TiO$_2$–Ruthenium Nano-photosensitizer Synergistically Produces Reactive Oxygen Species in both Hypoxic and Normoxic Conditions. *Angew. Chemie - Int. Ed.* **56**, 10717–10720 (2017).

123. Sauvé, G. *et al.* Dye sensitization of nanocrystalline titanium dioxide with osmium and ruthenium polypyridyl complexes. *J. Phys. Chem. B* **104**, 6821–6836 (2000).

124. Furtado, L. F. O., Alexiou, A. D. P., Gonçalves, L., Toma, H. E. & Araki, K. TiO$_2$-Based Light-Driven XOR/INH Logic Gates. *Angew. Chemie* **118**, 3215–3218 (2006).

125. Buchalska, M. *et al.* Photoinduced hole injection in semiconductor-coordination compound systems. *Coord. Chem. Rev.* **257**, 767–775 (2013).

126. Kuncewicz, J., Ząbek, P., Kruczała, K., Szaciłowski, K. & MacYk, W. Photocatalysis involving a visible light-induced hole injection in a chromate(VI)-TiO$_2$ system. *J. Phys. Chem. C* **116**, 21762–21770 (2012).

127. Tel, H., Altaş, Y. & Taner, M. S. Adsorption characteristics and separation of Cr(III) and Cr(VI) on hydrous titanium(IV) oxide. *J. Hazard. Mater.* **112**, 225–231 (2004).

128. Liang, P., Shi, T., Lu, H., Jiang, Z. & Hu, B. Speciation of Cr(III) and Cr(VI) by nanometer titanium dioxide micro-column and inductively coupled plasma atomic emission spectrometry. *Spectrochim. Acta - Part B At. Spectrosc.* **58**, 1709–1714 (2003).

129. Brito, F. *et al.* Equilibria of chromate(VI) species in acid medium and ab initio studies of these species. *Polyhedron* **16**, 3835–3846 (1997).

130. Valari, M., Antoniadis, A., Mantzavinos, D. & Poulios, I. Photocatalytic reduction of Cr(VI) over titania suspensions. *Catal. Today* **252**, 190–194 (2015).

131. Bakowsky, U. *et al.* Characterization of the interactions between various hexadecylmannoside-phospholipid model membranes with the lectin Concanavalin A. *Phys. Chem. Chem. Phys.* **2**, 4609–4614 (2000).

132. Flores, A. & Pérez, J. M. Cytotoxicity, apoptosis, and in vitro DNA damage induced by potassium chromate. *Toxicol. Appl. Pharmacol.* **161**, 75–81 (1999).

133. Emadi, A. & Gore, S. D. Arsenic trioxide - An old drug rediscovered. *Blood Rev.* **24**, 191–199 (2010).

134. Newbold, R. F., Amos, J. & Connell, J. R. The cytotoxic, mutagenic and clastogenic effects of chromium-containing compounds on mammalian cells in culture. *Mutat. Res. Toxicol.* **67**, 55–63 (1979).

135. Pedraza-Chaverri, J. *et al.* Protective effects of garlic powder against potassium dichromate-induced oxidative stress and nephrotoxicity. *Food Chem. Toxicol.* **46**, 619–627 (2008).

136. Budhwar, R. & Kumar, S. Prevention of chromate induced oxidative stress by alpha-lipoic acid. *Indian J. Exp. Biol.* **43**, 531–535 (2005).

137. Buttner, B. & Beyersmann, D. Modification of the erythrocyte anion carrier by chromate. *Xenobiotica* **15**, 735–741 (1985).

138. Morse, J. L., Luczak, M. W. & Zhitkovich, A. Chromium(VI) causes interstrand DNA cross-linking in vitro but shows no hypersensitivity in cross-link repair-deficient human cells. *Chem. Res. Toxicol.* **26**, 1591–1598 (2013).

139. Shi, X. & Dalal, N. S. Generation of hydroxyl radical by chromate in biologically relevant systems: Role of Cr(V) complexes versus tetraperoxochromate(V). *Environ. Health Perspect.* **102**, 231–236 (1994).

140. Son, Y. O. *et al.* Cr(VI) induces mitochondrial-mediated and caspase-dependent apoptosis through reactive oxygen species-mediated p53 activation in JB6 Cl41 cells. *Toxicol. Appl. Pharmacol.* **245**, 226–235 (2010).

141. Yao, Z. *et al.* Photocatalytic reduction of potassium chromate by Zn-doped TiO2/Ti film catalyst. *Appl. Surf. Sci.* **256**, 1793–1797 (2010).

142. Ku, Y. & Jung, I. L. Photocatalytic reduction of Cr(VI) in aqueous solutions by UV irradiation with the presence of titanium dioxide. *Water Res.* **35**, 135–142 (2001).

143. Zhang, Y., Xu, M., Li, H., Ge, H. & Bian, Z. The enhanced photoreduction of Cr(VI) to Cr(III) using carbon dots coupled TiO_2 mesocrystals. *Appl. Catal. B Environ.* **226**, 213–219 (2018).

144. Guertin, J. Toxicity and Health Effects of Chromium (All Oxidation States). *Chromium Handb.* 215–234 (2005).

145. Perrier, S. 50th Anniversary Perspective: RAFT Polymerization - A User Guide. *Macromolecules* **50**, 7433–7447 (2017).

146. Kreuter, J. Nanoparticles and microparticles for drug and vaccine delivery. *J. Anat.* **189 (Pt 3**, 503–505 (1996).

147. Li, J., Wang, L. & Benicewicz, B. C. Synthesis of Janus nanoparticles via a combination of the reversible click reaction and 'grafting to' strategies. *Langmuir* **29**, 11547–11553 (2013).

148. Li, B. *et al.* Diblock copolymer micelles deliver hydrophobic protoporphyrin IX for photodynamic therapy. *Photochem. Photobiol.* **83**, 1505–1512 (2007).

149. Song, X., Feng, L., Liang, C., Yang, K. & Liu, Z. Ultrasound Triggered Tumor Oxygenation with Oxygen-Shuttle Nanoperfluorocarbon to Overcome Hypoxia-Associated Resistance in Cancer Therapies. *Nano Lett.* **16**, 6145–6153 (2016).

150. Lee, H. Y., Kim, H. W., Lee, J. H. & Oh, S. H. Controlling oxygen release from hollow microparticles for prolonged cell survival under hypoxic environment. *Biomaterials* **53**, 583–591 (2015).

151. Song, G. *et al.* Perfluorocarbon-Loaded Hollow Bi_2Se_3 Nanoparticles for Timely Supply of Oxygen under Near-Infrared Light to Enhance the Radiotherapy of Cancer. *Adv. Mater.* **28**, 2716–2723 (2016).

152. Riess, J. G. Perfluorocarbon-based oxygen delivery. *Artif. Cells, Blood Substitutes, Biotechnol.* **34**, 567–580 (2006).

153. Riess, J. G. & Riess, J. G. Oxygen carriers ('blood substitutes') - Raison d'etre, chemistry, and some physiology. *Chem. Rev.* **101**, 2797–2919 (2001).

154. Xiang, Y., Bernards, N., Hoang, B., Zheng, J. & Matsuura, N. Perfluorocarbon

nanodroplets can reoxygenate hypoxic tumors in vivo without carbogen breathing. *Nanotheranostics* **3**, 135–144 (2019).

155. Carmeliet, P. & Jain, R. K. Principles and mechanisms of vessel normalization for cancer and other angiogenic diseases. *Nat. Rev. Drug Discov.* **10**, 417–427 (2011).

156. Delaney, L. J. *et al.* Breast Cancer Brain Metastasis Response to Radiation After Microbubble Oxygen Delivery in a Murine Model. *J. Ultrasound Med.* **38**, 3221–3228 (2019).

157. Jiang, M. S. *et al.* Inhibiting Hypoxia and Chemotherapy-Induced Cancer Cell Metastasis under a Valid Therapeutic Effect by an Assistance of Biomimetic Oxygen Delivery. *Mol. Pharm.* **16**, 4530–4541 (2019).

158. Wang, Q. *et al.* Fluorinated polymeric micelles to overcome hypoxia and enhance photodynamic cancer therapy. *Biomater. Sci.* **6**, 3096–3107 (2018).

159. Lane, D. D. *et al.* Well-defined single polymer nanoparticles for the antibody-targeted delivery of chemotherapeutic agents. *Polym. Chem.* **6**, 1286–1299 (2015).

160. Lane, D. D. *et al.* Dynamic intracellular delivery of antibiotics via pH-responsive polymersomes. *Polym. Chem.* **6**, 1255–1266 (2015).

161. Keddie, D. J. A guide to the synthesis of block copolymers using reversible-addition fragmentation chain transfer (RAFT) polymerization. *Chem. Soc. Rev.* **43**, 496–505 (2013).

162. Yao, W., Li, Y. & Huang, X. Fluorinated poly(meth)acrylate: Synthesis and properties. *Polymer (Guildf).* **55**, 6197–6211 (2014).